DENDRIMERS ON SUBSTRATES: INTERFACIAL INTERACTIONS, DOMAIN FORMATION AND PHYSICAL INTERMIXING

by

Fengting Xu

BS, Tsinghua University, 1997

MS, Institute of Metal Research, Chinese Academy of Sciences, 2000

Submitted to the Graduate Faculty of

The School of Engineering in partial fulfillment

of the requirements for the degree of

Doctor of Philosophy

University of Pittsburgh

2005

UNIVERSITY OF PITTSBURGH

SCHOOL OF ENGINEERING

This dissertation was presented

by

Fengting Xu

It was defended on

July 7, 2005

and approved by

Dr. Andrew J. Gellman, Professor, Department of Chemical Engineering

Dr. John P. Leonard, Assistant Professor, Department of Materials Science and Engineering

Dr. Ian Nettleship, Associate Professor, Department of Materials Science and Engineering

Dr. Judith C. Yang, Associate Professor, Department of Materials Science and Engineering

Dr. John A. Barnard, Professor, Department of Materials Science and Engineering
Dissertation Director

DENDRIMERS ON SUBSTRATES: INTERFACIAL INTERACTIONS, DOMAIN FORMATION AND PHYSICAL INTERMIXING

Fengting Xu, PhD

University of Pittsburgh, 2005

Dendrimers are three-dimensional, globular, highly-branched macromolecules made up of a focal point surrounded by repetitive units all enclosed by a terminal group 'shell'. Both their chemistry and size (in the range about ~1 - ~10 nm) are precisely tailorable and some dendrimers are known to readily form monolayers on technologically useful substrates. For these reasons they are of interest both scientifically and practically in the context of nanostructure and ultra-thin film studies. This dissertation focuses on three interrelated issues: 1) interfacial interactions (the role of dendrimer monolayers in mediating the properties of subsequently deposit thin films), 2) submonolayer dendrimer domain formation, and, 3) physical intermixing between dendrimer domains and metal overlayers.

In the dendrimer mediation section, the effects of dendrimer monolayers on thin metal overlayers, subsequently deposited by physical vapor deposition, are studied focusing on tribomechanical behavior and molecule-metal reactions. Dendrimer monolayer mediation of Cu and Cr overlayer films is found to dramatically influence nanoscratch mechanisms in these systems. Physical intermixing of metal atoms with dendrimer molecules to form a nanocomposite with distinct properties (rather than chemical interaction, grain size effects, etc.) is proposed as the probable explanation for these observations. In the domain formation section, a simple aerosol spray process is developed and used to prepare thin dendrimer-containing liquid layers from which submonolayer dendrimer domains form during the evaporation of solvent. An understanding of the relevant physical interactions (e.g., dewetting, boundary energy, long-range

repulsion, dendrimer-substrate and dendrimer-dendrimer bonding, domain thermal stability, etc.) which control the form and coverage-dependent evolution of experimentally observed domains is developed. The importance of electrostatic interaction revealed in this section motivated a study of charge patterning by scanning probe microscopy methods in granular materials (Appendix A). Finally, submonolayer dendrimer domain patterns with uniform monolayer thickness are used as heterogeneous substrates for the deposition of Au overlayers. Direct evidence is found for the extent and type of physical intermixing of non-reaction Au with dendrimer monolayer domains by atomic force microscopy based step-height and force measurements as a function of Au thicknesses.

TABLE OF CONTENTS

LIST OF TABLES

LIST OF FIGURES

ACKNOWLEDGEMENTS

My first and foremost acknowledgement must go to my advisor, Prof. John A. Barnard. Less than five years ago, his accepting me to be a PhD student in the group gave me the chance to work under his superb supervision. I appreciate his advice, patience, and guidance both in my everyday life and academic education as well as the financial support.

I would also like to thank all of our collaborators on the various projects, including Prof. Shane C. Street and his students Dr. Michael L. Curry and David L. Arrington from University of Alabama. I also owe special thanks to Prof. Judith C. Yang and her research associate Mr. Long Li with the TEM. In addition, my sincere appreciation goes out to all of the faculty, students, and postdoctoral students in the Materials Science and Engineering department at the University of Pittsburgh and the IRG2 group in the MINT Center of University of Alabama.

I owe many thanks to my committee members: Prof. Andrew J. Gellman, Prof. John P. Leonard, Prof. Ian Nettleship, Prof. Judith C. Yang, and Prof. John A. Barnard. I want to thank them for serving on my committee and helping to make the dissertation better. I also want to thank Prof. William A. Soffa for the help of my dissertation.

I would like to extend my appreciation to my formal group members and friends for the initial training on the instruments and useful discussion of the projects, including Dr. Feng Huang, Dr. James L. Weston, Dr. Guohua Wei, Dr. Andrei Rar, Dr. Shi-Shen Yan from University of Alabama, Dr. Guangwen Zhou, Mr. Long Li, Mr. Liang Wang, Mr. Sean M. Thaler, and Ms. Fang-I Li from the University of Pittsburgh. I am also forever indebted to the department secretaries for their endless help in my documentation.

I want to thank my parents Fulan Xia and Fugan Xu, and my two sisters for their constant support and encouragement throughout the past years. I also want to thank my wife, Pingping Ye, and our daughter Jennifer (Yunwen) Xu for their love and companionship. As I get older and wiser, I become more aware of just how important it is to have the support of such loving and devoted family members.

1.0 INTRODUCTION

Dendrimers are three-dimensional, globular, highly-branched macromolecules made up of a focal point surrounded by repetitive units all enclosed by a terminal group 'shell'. Both their chemistry and size can be precisely tailored by controlling the core type, the extent of branching, and the nature of the end groups. Dendrimers are true nanomaterials as their diameters are restricted to the range from ~1 - ~10 nm. Some classes of dendrimers are known to readily form compact monolayers on technologically useful substrates. Dendrimer layers are beginning to receive attention with regard to their adhesive and frictional behavior and related potential applications. Dendrimers are also a convenient, commercially available organic constituent which can be used in the development of hybrid organic-inorganic nanocomposites with new function and properties. For these reasons dendrimers are of interest both scientifically and practically in the context of nanostructure and thin film studies.

This dissertation considers three interrelated issues: 1) interfacial interactions in continuous dendrimer layers (specifically, the role of dendrimer *monolayers* in mediating the properties of subsequently deposited thin metal films), 2) *submonolayer* dendrimer domain formation, and, 3) physical intermixing between dendrimer domains and subsequently deposited metal overlayers. The areas of interest explored in this dissertation are summarized schematically in Figure 1.1. The development of new insights and a better understanding of dendrimer-dendrimer, dendrimer-substrate, and dendrimer-overlayer interactions is a key objective of this work.

In the dendrimer mediation section (Results – Part 1), the effects of dendrimer monolayers on thin metal overlayers, subsequently deposited by physical vapor deposition, are studied with special attention on tribo-mechanical behavior and molecule-metal reactions. This work was undertaken to determine whether a single monolayer of dendrimer molecules only a few nm thick could substantially influence the properties of subsequently deposited thin metal layers. Results from these studies clearly demonstrate the potential for mediating metal overlayer properties and performance with dendrimer monolayers. In the domain formation section (Results – Part 2), a simple aerosol spray process is developed and used to prepare thin dendrimer-containing liquid layers from which organized submonolayer dendrimer domains form during the evaporation of solvent. An understanding of the relevant physical interactions (e.g., dewetting, boundary energy, long-range repulsion, dendrimer-substrate, dendrimer-dendrimer bonding, etc.) which control the form and coverage-dependent evolution of experimentally observed domains is developed. The importance of electrostatic interactions in domain formation revealed in part 2 motivated an ancillary study of charge patterning contained in Appendix A. Finally, the submonolayer dendrimer domain patterns with uniform monolayer thickness (developed in Part 2) are used as 'heterogeneous' substrates for the deposition of metal overlayers (Results – Part 3). The extent of physical intermixing and the nature of the free surface following deposition are investigated for variable metal overlayer thicknesses. Such films, in which dendrimer-covered and dendrimer-free regions coexist on the same substrate, allow for a direct comparison of metal overlayer interpenetration and dendrimer-metal nanocomposite behavior.

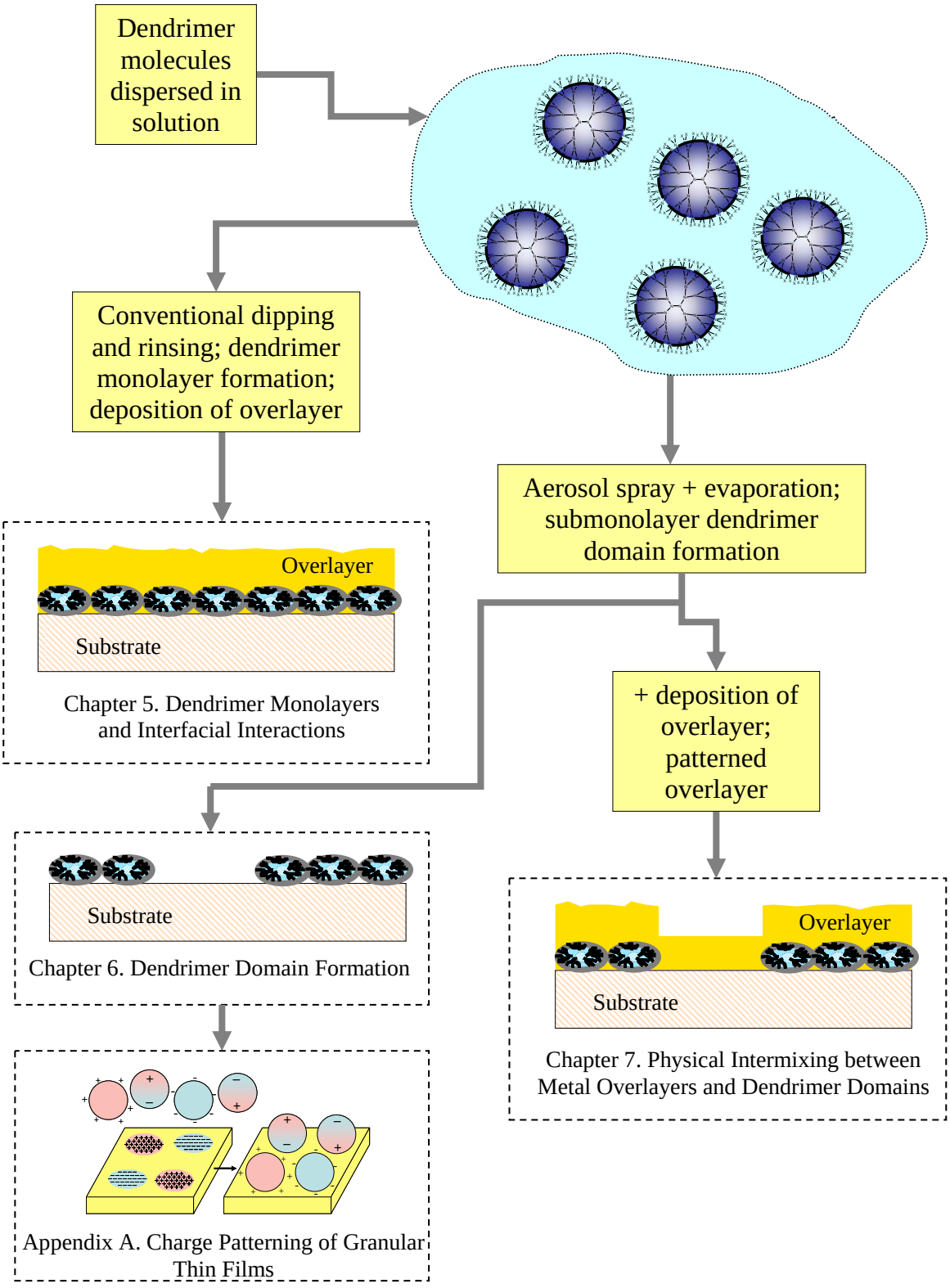

Figure 1.1 Schematic representation of the relationship of the key elements considered in this dissertation.

The dissertation is organized by chapter as follows. Background material on the history of dendrimer synthesis, self assembly processes, and early dendrimer mediation studies is found in Chapter 2. Chapter 3 introduces the instruments and experimental techniques used in sample preparation and characterization. A more detailed overview of the proposed work of the dissertation is found in Chapter 4. Interfacial interactions (the role of dendrimer monolayers in mediating the properties of subsequently deposit thin films) are explored in Chapter 5. Submonolayer dendrimer domain formation using the aerosol spray technique is reviewed in Chapter 6. The nature of the physical intermixing between submonolayer dendrimer domains and metal overlayers is discussed in Chapter 7. Finally, the principle conclusions and impact of this work, as well as the most promising avenues for future research are summarized in Chapter 8.

2.0 BACKGROUND

2.1 DENDRIMER MOLECULES

Dendrimers are three-dimensional, globular, highly-branched macromolecules made up of a focal point surrounded by repetitive units all enclosed by a terminal group 'shell'. They can be synthesized with highly controllable sizes (they are essentially monodisperse) determined by the core type, extent of branching, and nature of the end groups, in the range from ~1 - ~10 nm in diameter[1-4]. They differ from classical monomers, oligomers and hyperbranched polymers because of their extraordinary symmetry, high degree of branching, and maximized terminal functionality density. These macromolecules bridge the gap between traditional natural organic molecules (MW < 2000) and traditional polymers generated from linear monomers. They have received intensive interest associated with their variable size, the controllable chemistry of their surfaces, and their potential for serving as the host for metal (and other) nanoparticles[5-7].

In 1978, Vögtle successfully developed a repetitive synthesis strategy for creation of well-defined branching structures[8, 9]. These new molecular architectures were originally called ‘cascade molecules’ (Figure 2.1). The term ‘dendrimer’ (greek: *dendron* = tree, *meros* = part) has come to be used to describe the architecture of this new class of molecules.

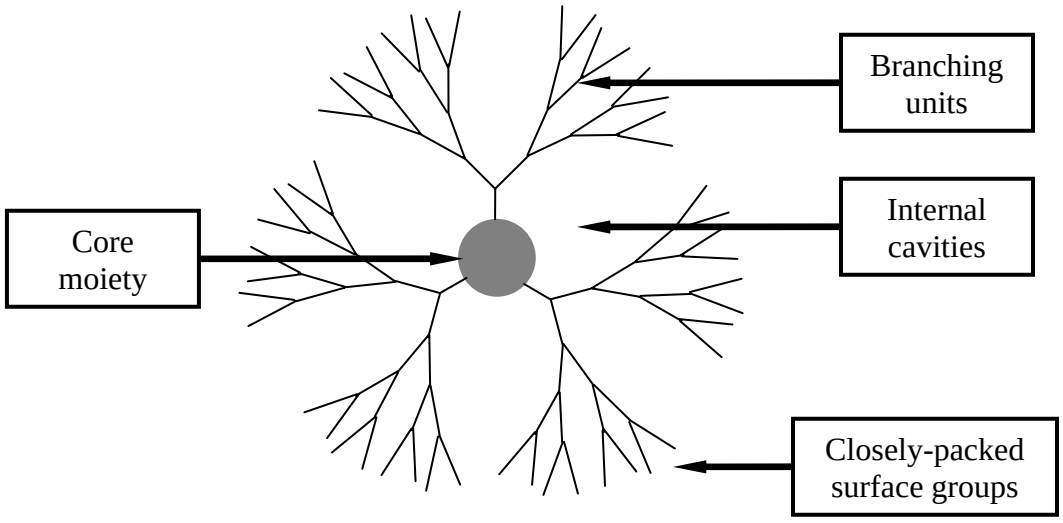

Figure 2.1 Schematic of the structure of the highly branched, globular structure of a dendritic molecule.

Progress in this area proceeded comparatively slowly at first (primarily due to challenges in synthesis) and then more rapidly from the early 1990s on[9]. The first fully investigated and also the best known dendritic structures are Tomalia's Poly(amidoamine) (PAMAM) dendrimers, first synthesized during the mid-1980s.

A dendrimer consists of three distinguishing architectural components[10].

(i) a focal point, (or central core, initiator core, core moiety);

(ii) an interior layer of branches (generations), composed of repeating units, linked radially to the central core;

(iii) terminal functional groups (or end or surface groups), i.e., the exterior attached to the outmost interior generation.

Commercially available poly(amidoamine) (PAMAM) dendrimers are used for all of the experiments in this dissertation. Their schematic physical structure and the chemical structure expected in solution are shown in Figure 2.2.

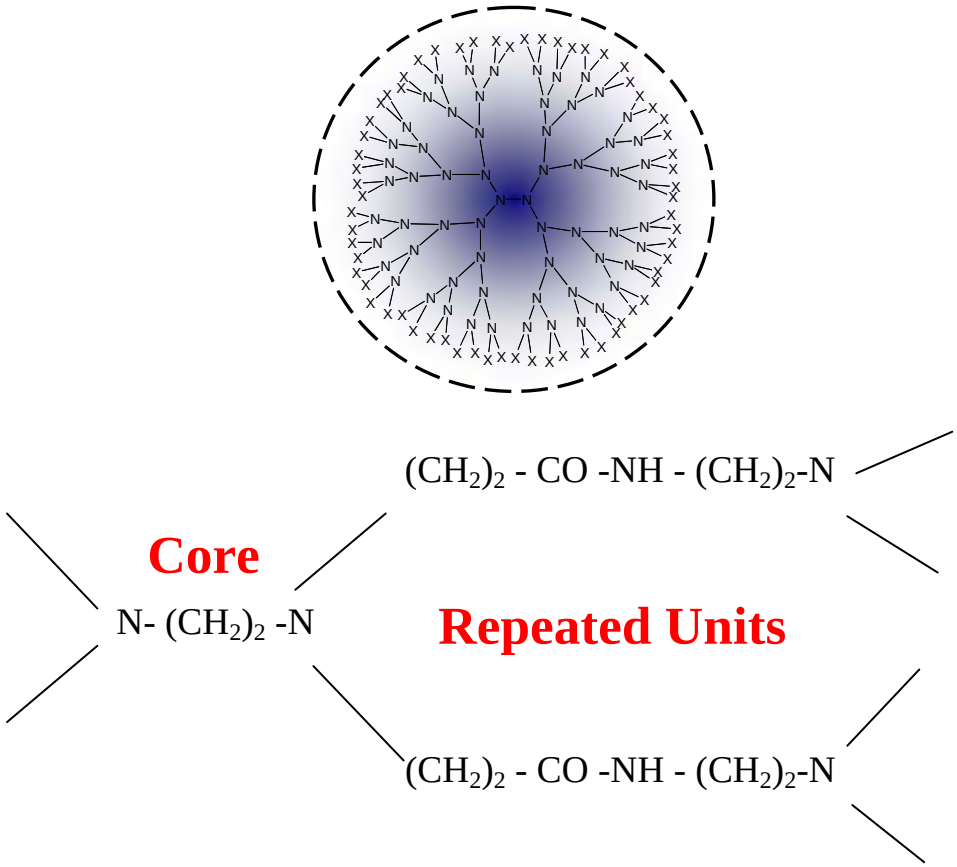

Figure 2.2 Schematic of the physical structure and chemical structure expected for PAMAM dendrimers in solution.

2.2 DENDRIMER SYNTHESIS

There are two fundamentally different approaches to dendrimer synthesis: (1) the divergent method[3, 10] begins with a multifunctional core molecule and one branching unit after another is successively attached to the core molecule; and (2) the convergent method[11, 12] takes

the opposite course, building dendritic architectures from the periphery and proceeding inward. In the divergent method, the integrity and purity of high generation dendrimers remain problematic since numerous reactions have to be conducted on a single molecule. Dendrimers produced from the convergent method are usually purer, but can not reach as many generations as divergently made dendrimers, primarily due to steric problems that arise from the reaction of the segments and the core molecule. The 'generation' indicates the number of branching steps (or shells) used in creating the final dendrimer molecule.

2.3 MOLECULAR MONOLAYERS

Although molecular adsorption on solid substrate surfaces has been the subject of rapidly increasing scientific interest in the last two decades, monolayers of organic materials have, in fact, been studied for many years. In 1774, Benjamin Franklin deposited a thin film of oil on the surface of a pond and observed the effects of surface tension. These observations were published and may be thought of as the first 'monolayer' study. In the early 1900s, Irving Langmuir conducted systematic research on organic monolayers and hence organic monolayers deposited on water are named after him. In 1935, Katherine Blodgett drew a solid substrate through a Langmuir film. The films created in this manner became known as Langmuir-Blodgett (LB) films. LB films have since been the subject of intensive scientific interest and have found use in many technological applications.

Self-assembled molecular monolayers can be formed spontaneously by contacting an appropriate substrate with an active surfactant. The first study of monolayer self-assembly can be attributed to Zisman in 1946. In a typical procedure, an appropriate substrate, e.g., gold, mica, silicon, etc., is introduced into an organic solvent containing the surface-active species, as shown

in Figure 2.3. Relatively few systems have been found in which complete monolayers are formed through chemisorption onto the solid substrate. Examples include organosilanes on hydroxylated surfaces, (e.g., the native oxide of silicon)[13-17], and alkanethiols on Au, Cu or Ag[18-20]. The energies associated with chemisorption are typically hundreds of kJ/mol. Some monolayers (Ar, Xe/Si[21], thiol on Au at low temperature) can be formed via physisorption. However, the energies involved in physisorption are substantially lower than for chemisorption, generally less than 50 kJ/mol. In certain systems physisorbed monolayers can be transformed to chemisorbed monolayers. For example, flat-lying physisorbed alkanethiols will transform to the upright-tilted alkyl chain of the saturated thiolate phase on Au by heating the Au substrate to remove H atoms in the SH group, enabling the formation of the S-Au bond[22]. The deposition of metals onto, for example, modified-end group alkylthiol self-assembled monolayers, is an active area of research[23-26]. Such systems may serve as models for studies of polymer-metal interactions.

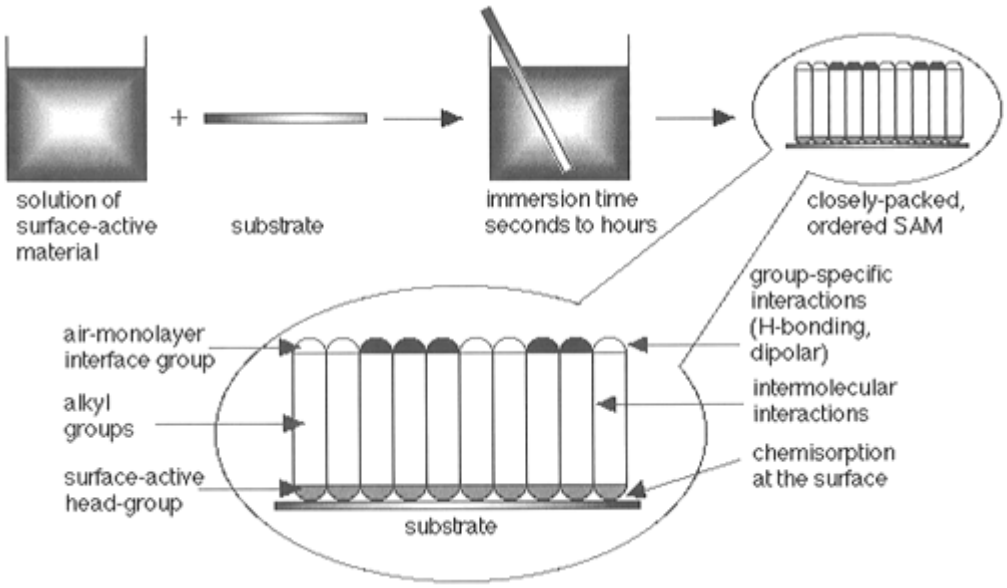

Figure 2.3 Self-assembled monolayers are formed by simply dipping a substrate into a solution of the surface-active material. The driving force for the spontaneous formation of the 2D assembly includes chemical bond formation between the molecules and the surface along with intermolecular interactions[27].

2.4 SELF-ASSEMBLED DENDRIMER MONOLAYERS

Dendrimer monolayers are an excellent candidate for the study of self assembly of organic molecules[28-30], as well as metal–organic interfacial reactions, and nanocomposite formation[31-35]. Certain types of dendrimers have been shown to readily form flat, complete monolayers on appropriate substrates[32]. It has been speculated that the main driving force for dendrimer monolayer formation on the native oxide of Si is electrostatic[36]. Tsukruk has proposed that the electrostatic interactions are complemented by the high interaction strength between "sticky" surface groups combined with short range van der Waals forces and long range capillary forces, i.e., a combination of forces are responsible for the formation of compact monolayer structures[36]. In related phenomena, dramatic conformational changes, from a more compact coiled to a stretched state, have been observed during adsorption of non-branched

polyionomers[28]. It is known that capillary forces between soft spherical latex nanoparticles may lead to severe deformation of particles and surface spreading during the drying process[37]. One might speculate that soft dendrimer 'nanoparticles' may behave similarly. Subsequent vapor or sputter deposition of metal onto dendrimer monolayers has been shown to result in hybrid dendrimer/metal nanocomposite thin films with surprising physico-mechanical behavior[31, 33-35, 38-40].

Dendrimers can readily form flat, complete monolayers[41, 42] using standard cleaning, dipping, and rinsing procedures, as shown in Figure 2.4. This procedure is analogous to that found in Figure 2.3 for L-B films. The average thickness of dendrimer films is invariably significantly smaller than the diameter of ideal spherical dendritic macromolecules in solution. It is well-established that poly(amidoamine) (PAMAM) dendrimers, which are roughly spherical in solution, "collapse" when adsorbed onto substrate surfaces (Figure 2.4). Heights (thicknesses) of both isolated molecules and monolayers [measured by scanning probe microscopy (SPM) and X-ray reflectivity (XRR)] are typically something less than half the diameter in solution, independent of generation. This is true not only of dried structures but also of adsorbed isolated dendrimers measured *in situ* at the liquid/substrate interface[28]. Generation 4 (G4) PAMAM dendrimers, which have a solution diameter of 4.5 nm, have displayed monolayer thicknesses on silicon ranging from 1.1 to 1.7 nm (SPM)[28] and from 1.4 to 2.2 nm (XRR)[31]. Isolated G4 PAMAM dendrimer molecules on Au have SPM-measured heights of 0.5-0.8 nm[43].

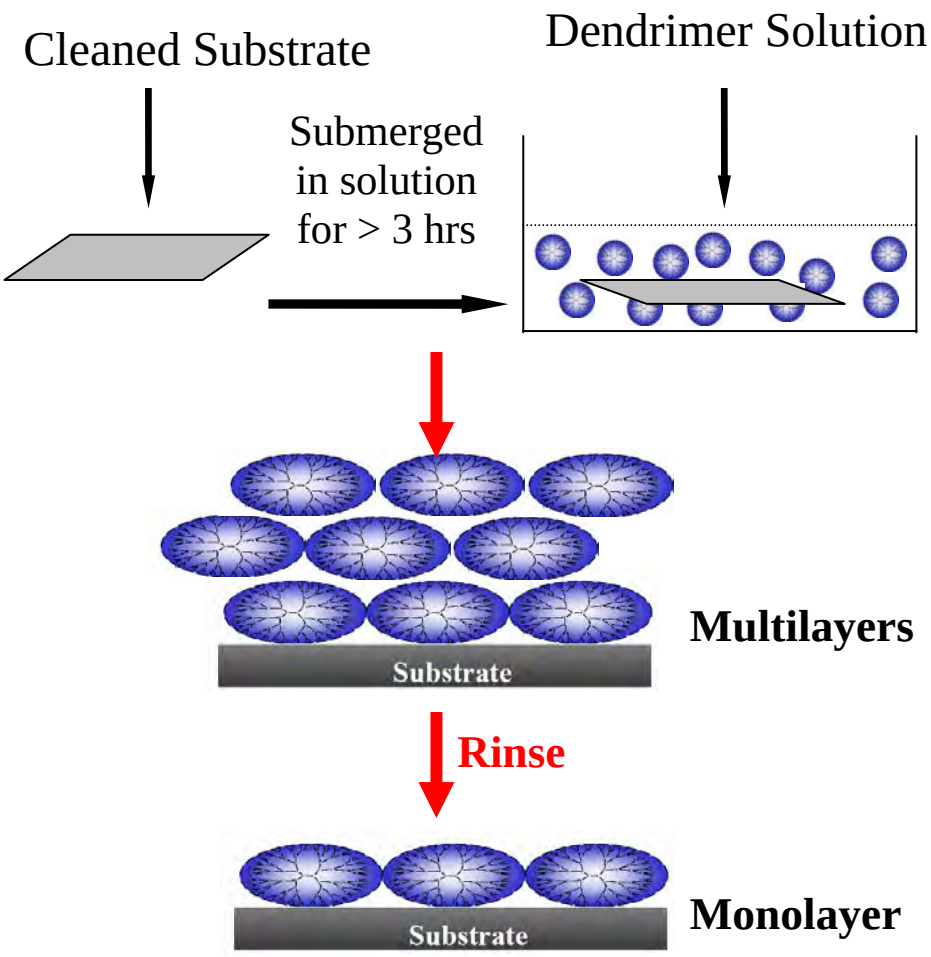

Figure 2.4 Schematics of the clean – dip - rinse procedure of making self-assembled dendrimer monolayers. The cleaned substrate is dipped into the dilute dendrimer solution for a controlled amount of time, removed and rinsed with ethanol alcohol and then water to remove the loosely bonded dendrimer molecules.

Table 2.1 shows representative physical constants of PAMAM dendrimers as a function of generation number in solution and as a condensed layer on a substrate. Note that due to the crowding effect of the end groups doubling with each increasing generation, dendrimers are difficult to synthesize above generation 12 (G12).

Table 2.1 Dendrimer Physical Constants. Molecular diameter in solution (D), thickness of dendrimer monolayer, molecular density of the unadsorbed molecule (ρ) and adsorbed as a monolayer (ρ_{ML}), number of terminal amine groups (N), theoretical molecular weight (MW), and calculated areal density (Γ) of NH_2 groups at the dendrimer surface as a function of dendrimer generation number. Values calculated from technical information available from Dendritech, Inc. (25% C_{12} PAMAM G4 is similar to G4 dendrimer except that 25% percent of the NH_2 end groups are replaced by C_{12} chains which will be explained more in later section)

G	D (nm)	Thickness (nm/ML)	ρ (g/cm^3)	ρ_{ML} (g/cm^3)	N (# end groups)	MW (a.u. x 10^3)	Γ (nm^{-2})
4	4.5	1.8	0.49	N/A	64	14.2	1.0
25%C_{12} G4	10.7	4.7	0.80	N/A	64	201.1	0.75 NH_2 0.25 C_{12}
5	5.4	N/A	0.58	N/A	128	28.8	1.4
6	6.7	2.8	0.61	N/A	256	58.0	1.8
7	8.1	3.7	N/A	N/A	512	116.5	2.5
8	9.7	4.6	0.81	1.1	1024	233.4	3.5
9	11.4	N/A	1.00	N/A	2048	467.2	5.0
10	13.5	5.6	1.21	N/A	4096	934.7	7.2

Although flat, complete monolayers of dendrimers formed on technologically interesting substrates have been realized by using standard cleaning, dipping, and rinsing procedures, the self-organized growth of complex submonolayer dendrimer patterns observed when finite volumes of dendrimer solution are cast on a substrate in a thin layer and allowed to evaporate has received comparatively little attention[44-47].

2.5 DENDRIMERS AS 'MEDIATING' LAYERS

Interest in thin organic films has intensified recently because of their importance for applications in micro- and nanoscale technology. Metal–organic interactions, including the

metallization of polymers, are an important part of this technology. One of the technical objectives in this area is to provide a durable, homogeneous, continuous, well-adhered surface with minimal (or controllable) roughness. Dendrimer monolayers have been used as the organic substrate in the study of metal–organic interfacial reactions and nanocomposite formation. It has been shown that the presence of a dendrimer monolayer can considerably improve the adhesion of an overlayer[32]. The enhanced adhesion has been associated with the aggregate strength of multidentate interactions - the dendrimer has many terminal functional end groups able to interact with both the surface of the substrate and the overlayer. The presence of a dendrimer monolayer can also strongly alter the topography, nanomechanical response, and chemistry of thin metal overlayers. Recent findings in dendrimer mediated metal films also include: significant reductions in the roughness of deposited metal films mediated by dendrimer monolayers, (Figure 2.5)[35]; a substantial increase in the nanomechanical hardness of ultrathin Au when deposited on a dendrimer adlayer by thermal evaporation (Figure 2.6)[31]; and the occurrence of interfacial reactions, including the formation of metal nitrides, following deposition of reactive metals such as Co and Cr onto amine-terminated dendrimer monolayers (Figure 2.7)[33, 34]. The surface roughness of evaporated Au deposited on a Si substrate decreases from 1.2 nm to 0.4 nm when a dendrimer monolayer is present. The apparent hardness of dendrimer-mediated Au films is as high as 3.2 GPa, almost twice the value for dendrimer-free Au films. In XPS N1s spectrum studies of dendrimer-mediated Co and Cr films, the occurrence of additional peak corresponding to the bonding energy of N1s in metal nitride form reveals that metal nitrides are formed . These effects have obvious implications for the metallization of substrates used in future nanoscale technological devices, in particular the possibility of

preventing diffusion of deposited metals into adjacent dielectric materials which can compromise electrical, photonic, and chemical properties.

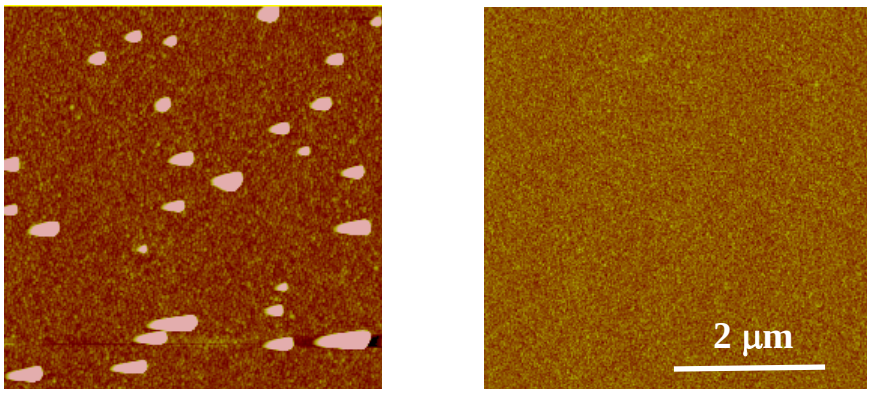

Figure 2.5 Surface roughness is much larger in dendrimer-free Au films (L) than dendrimer-mediated Au films (R). Au films deposited by evaporation on a Si wafer (image is 5μm x 5μm). Distortion in left image is due to the very large defect feature heights.

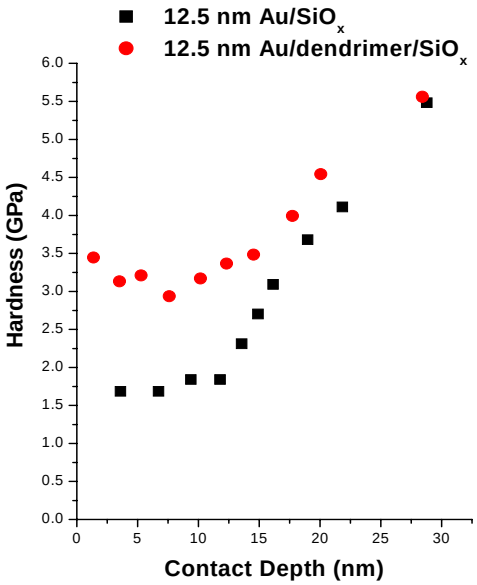

Figure 2.6 Nanoindentation hardness profiles of dendrimer-mediated and dendrimer-free Au films deposited by evaporation onto a Si wafer with native oxide.

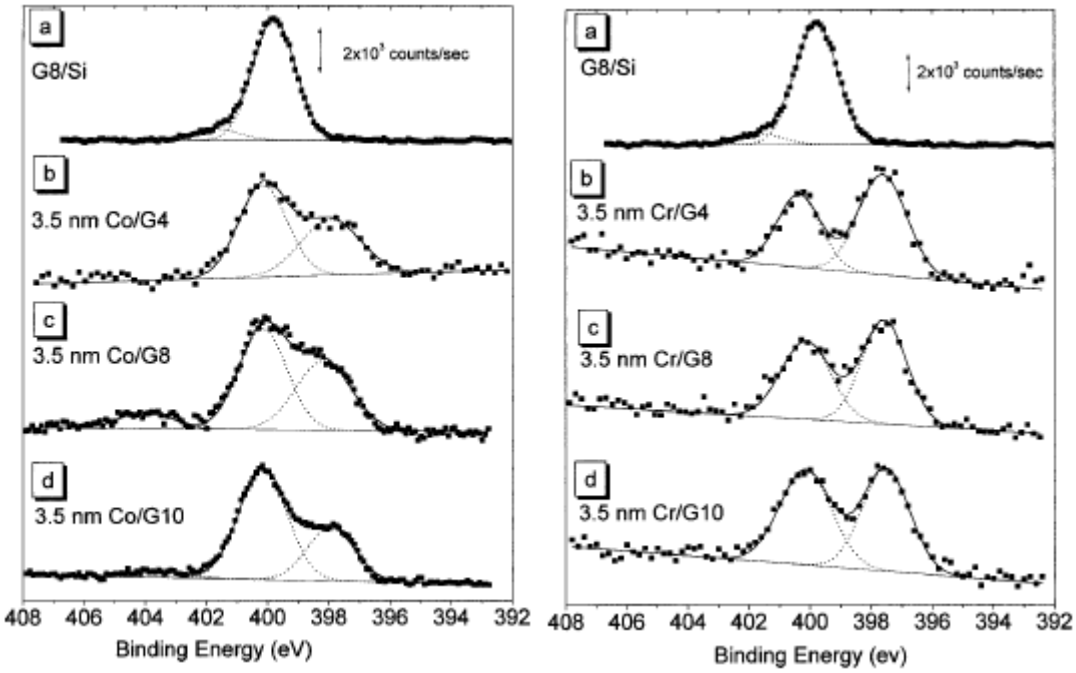

Figure 2.7 XPS spectra for N 1s region. Left: (a) G8 monolayer/Si, and 3.5 nm Cr on (b) G4 monolayer/Si, (c) G8 monolayer/Si, and (d) G10 monolayer/Si. Right: (a) G8 monolayer/Si, and 3.5 nm Co on (b) G4 monolayer/Si, (c) G8 monolayer/Si, and (d) G10 monolayer/Si.

3.0 EXPERIMENTAL TECHNIQUES

3.1 SUBSTRATE PREPARATION

Substrate preparation and cleanliness are critical in obtaining reproducible results in experiments of the type carried out in this dissertation. All glassware was cleaned in normal detergents, followed by generous rinsing with distilled water. The glassware was then cleaned with Nochromix (oxidizer)/H_2SO_4 solution to remove both organic and inorganic matter and thoroughly rinsed again in deionized water.

3.1.1 Si Substrates

In general, the method detailed by Crooks and co-workers[32] in preparing dendrimers adsorbed on Si wafers was followed. The substrates were immersed in freshly prepared piranha solution (3:1 H_2SO_4/30% H_2O_2) for 1 hour to remove organic impurities. (Caution: piranha solution reacts violently with organic matter. Care should be taken in the use and proper disposal of this oxidizer). The substrates were then rinsed with plenty of water, and ethanol alcohol before using dry nitrogen to blow them dry. Ellipsometric measurements indicate that the piranha etch treatment leaves a 2.5 nm-thick SiO_x film on the freshly prepared surface[35].

3.1.2 Mica Substrates

Muscovite mica was also used as a substrate for our experiments. Mica is a potassium aluminum silicate mineral, which has the form of $KAl_2(AlSi_3O_{10})(OH)_2$. Muscovite is the most common form of mica, ranging from colorless or pale yellow to gray and brown. It has a pearly luster, and is used as an insulator. The mica sheets were purchased from Structure Probe, Inc®. All the mica sheets were graded V1 or V4. The difference between V1 and V4 is that V4 has 25% air (which is “ancient” air) content – it does not exist as actual "pores" or "voids" but in layers parallel to the micaceous cleavage planes. V1 has essentially zero % air. For some research this is an important difference, but for our experiments, no differences were observed between the two grades of mica.

Each mica sheet was cleaned thoroughly by ethanol alcohol before use. Fresh mica surfaces were prepared by cleaving with a thoroughly cleaned razor. Since the mica has a layered structure, once separation is achieved at a corner, it is fairly easy to cleave with the razor and achieve an atomically flat fresh surface (with roughness ~ 0.082 nm).

3.1.3 HOPG Substrate

Highly ordered pyrolytic graphite (HOPG) was also an excellent choice as the substrate used in this dissertation. HOPG is a relatively new form of high purity carbon with ABABAB hexagonal layer structure. The A-A layer distance is 6.7 Å. Like mica, HOPG has an atomically flat surface – making it an excellent substrate for scanning probe microscopy measurements. The fresh smooth surface can be cleaved like mica.

3.2 DENDRIMER SELF ASSEMBLY

3.2.1 Self assembly of dendrimer monolayers

Dendrimer solutions were prepared by simple volumetric dilution using pipettes with disposable tips from fresh commercial methanol-based solutions obtained as 10 weight percent methanolic solutions from Aldrich (Milwaukee, WI). Following the method proposed by Crooks, et. al.[32], the clean Si wafers and mica were placed in ground-glass-sealed weigh bottles along with 1μM ethanolic solutions of the PAMAM dendrimers and allowed to remain at least 3 h (usually overnight) before removal. Upon removal the substrates were copiously rinsed with pure ethanol and dried in a stream of dry N_2. This procedure is known to produce dendrimer monolayers from this class of dendrimer molecules.

3.2.2 Self assembly of submonolayer dendrimer domains

Submonolayer dendrimer film structures were prepared by aerosol spray deposition using an EFFA Spray Mounter MK II (Ernest F. Fullam, Inc.). Aerosol deposition was used as a convenient way to rapidly and relatively uniformly transport a finite volume of fluid to a substrate to form a thin fluid layer. In our experiments the volume of fluid used yielded a fluid film thickness of ~ 15 μm, see Figure 3.1. The EFFA Spray Mounter MK II system, using the Bernoulli principle[48], can be used to disperse fluids onto a substrate in a fine uniform layer. Reproducible amounts of fluids are drawn into special capillary tubes, inserted into the plastic pipette, and dispersed without danger of coagulation or large droplet formation. The direction of the spray was ~ normal to the substrate surface. The distance from spray source to substrate

surface was kept at ~15 cm. In the case of mica substrates the dendrimer solution was sprayed onto the fresh side of the mica immediately after cleaving.

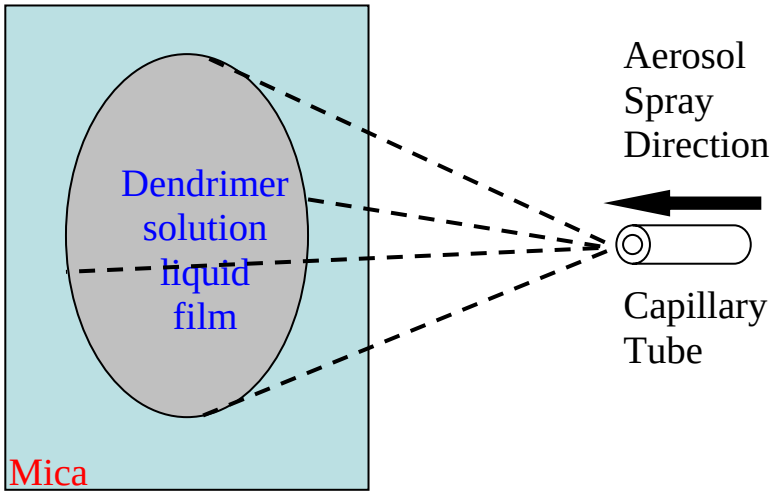

Figure 3.1 Schematic of the aerosol spray technique.

The average droplet diameter in the aerosol was ~10 µm. This was determined by using stained aerosol solution sprayed at an angle and distance from the substrate so as to produce some isolated droplets. The dried stained droplets were observed with an optical microscope. Under normal deposition conditions the droplets coalesced upon arrival at the substrate. Preliminary aerosol depositions were carried out using various dendrimer concentrations and total fluid volumes to determine conditions that produced dried dendrimer film structures with total volumes per substrate area corresponding to thicknesses ("equivalent thicknesses") ranging from ~ 0.3 to ~ 2 nm. In the experiments described here, two different dendrimers and solvents are used for the aerosol spray. One is produced by aerosol deposition and subsequent evaporation of 0.04 wt % ethanolic solutions of generation 4 (G4) PAMAM dendrimer. The second utilized 0.05 wt % pentanol solutions of 25%C_{12} PAMAM G4 dendrimer which has 25% C_{12} terminations besides the normal amine end groups (48 primary amino surface groups and 16

[N-(2-hydroxydodecyl)] surface groups, theoretical molecular weight 20,113 amu). A comparison of the structure of a standard G4 molecule with a 25% C_{12} PAMAM G4 molecule is found in Figure 3.2. The solutions were prepared by simple volumetric dilution using pipettes with disposable tips from fresh commercial methanol-based solutions.

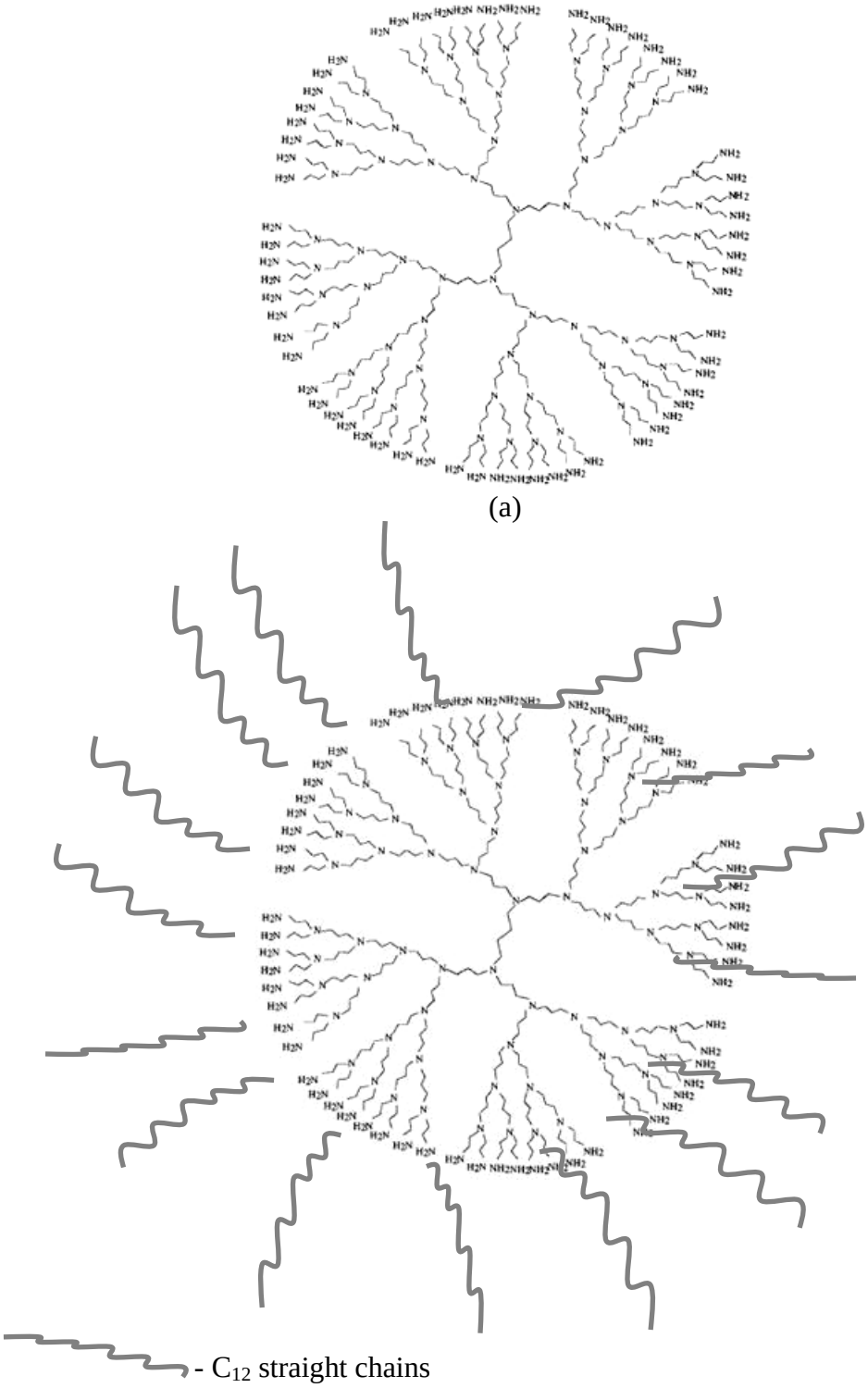

Figure 3.2 Comparison between normal G4 (a) and 25% C_{12} PAMAM G4 (b) dendrimer. There are 25% C_{12} [N-(2-hydroxydodecyl)] terminal groups replacing the normal NH_2 groups in (b).

3.3 METAL OVERLAYER DEPOSITION

Conventional DC magnetron sputtering was used for the overlayer film deposition. Figure 3.3 shows the schematic layout and process of a typical sputtering system. The process is designed to transfer atoms of the material of interest from the 'target' to the substrate. The target (cathode) is connected to the negative terminal of a DC power supply. The substrate (anode) may be grounded, positive/negatively biased, and heated/cooled or some combination of these. The chamber is pumped to 10^{-7}~10^{-8} Torr level before introducing the working gas, typically argon. The working gas is the medium used to initiate and sustain the electrical discharge. To deposit thin films, atoms are controllably transferred from the source (target) to the substrate where film formation and growth proceed atom by atom. In sputtering, the atoms are dislodged from the surface of the solid target through impact of gaseous ions. Sputtering processes are conventionally divided into four categories: (1) DC, (2) RF, (3) magnetron, (4) reactive. However, there are hybrids between categories such as DC magnetron sputtering and DC magnetron reactive sputtering which were used in this investigation. During sputtering[49, 50], the positive ions in the plasma strike the cathode and eject neutral target atoms through momentum transfer. These atoms enter and pass through the plasma region to eventually deposit on the substrate and create growing film. At the same time, secondary electrons and negative ions are accelerated toward the anode (substrate) bombarding the growing film, which may be undesirable.

Two commercial sputtering systems - Key® and Innovative Systems® - were used for the film deposition. In both systems, in order to increase the sputtering efficiency, a permanent magnet is embedded within the cathode target such that the resultant magnetic field is several

hundred gauss. This process is the called DC magnetron sputtering and it was used for the film deposition in this dissertation.

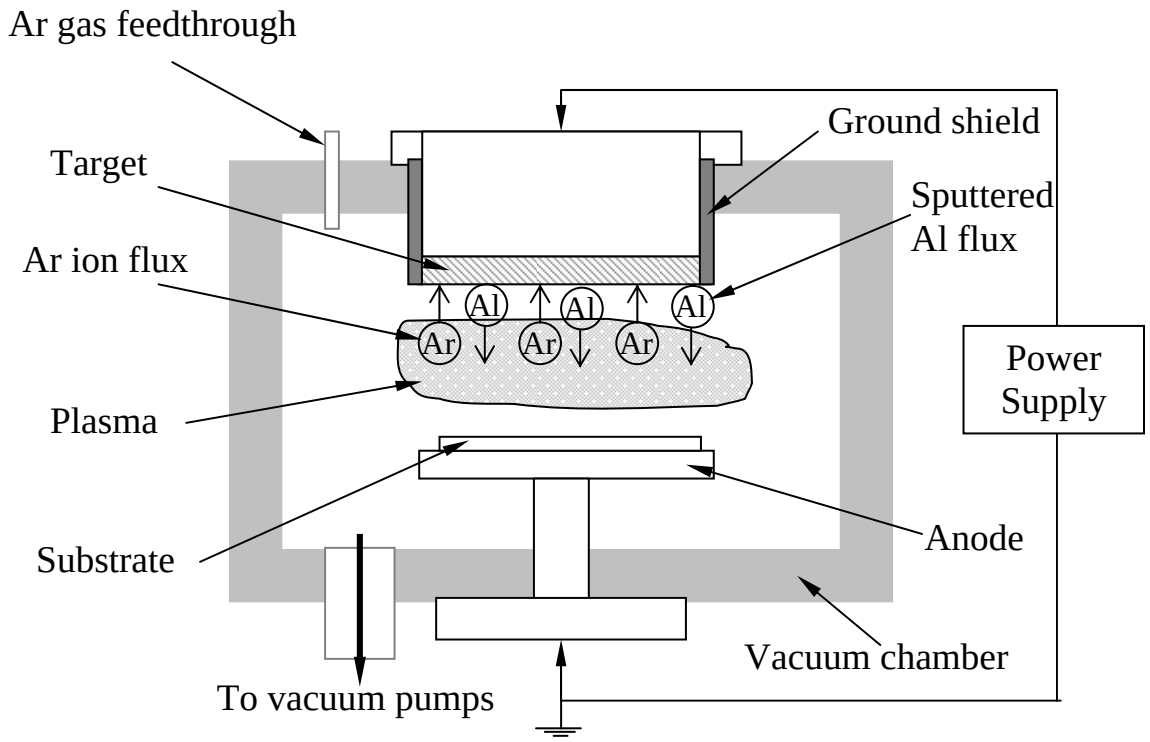

Figure 3.3 Schematic of the sputtering process.

3.4 ATOMIC FORCE MICROSCOPY

The first scanning probe technique, scanning tunneling microscope (STM) was developed in 1981 by Gerd Binning and Heinrich Rohrer at IBM Zurich[51]. The scanning probe microscope is a scanning image tool with a large dynamic range, spanning the realms of optical and electron microscopes. It has unprecedented resolution when used as a surface profiler. Atomic force microscopy (AFM) or scanning force microscopy (SFM) was invented in 1986 by Binning,

Quate, and Gerber[52]. It combines the principles of operation of the STM and the Stylus Profilometer.

Figure 3.4 schematically illustrates the principles of operation of an STM as well as an AFM. The tip follows contour B, in one case to keep the tunneling current constant (STM) and in the other to maintain constant force between tip and sample (AFM, sample and tip either insulating or conducting). Like other scanning probe microscopies (SPM), the AFM utilizes a sharp probe moving over the surface of a sample in a raster scan. In the case of the AFM, the probe is a tip on the end of a cantilever, which bends in response to the force between the tip and the sample. The first AFM used a scanning tunneling microscope at the end of the cantilever to detect the bending of the lever, but now most AFMs employ an optical lever technique. The diagram in Figure 3.5 illustrates how this works; as the cantilever flexes, the light from the laser is reflected onto the photosensitive detector (PSD). By measuring the differences in signal at the PSD, changes in the bending of the cantilever can be measured. Since the cantilever obeys Hooke's Law for small displacements, the interaction force between the tip and the sample can be found. The movement of the tip or sample is controlled by an extremely precise positioning device made from piezo-electric ceramics, most often in the form of a tube scanner. The scanner is capable of sub-angstrom resolution in the x-, y- and z-directions. The z-axis is conventionally perpendicular to the sample. Besides high resolution topography scanning, AFM can also measure physical properties such as localized friction, stray fields from magnetic domains, surface conductivity, surface potential, adhesion, and nanomechanical behavior. Recently it has also been used to generate patterns on surfaces, for example by Dip-Pen Nanolithography (DPN)[53] and charge writing techniques[54-59].

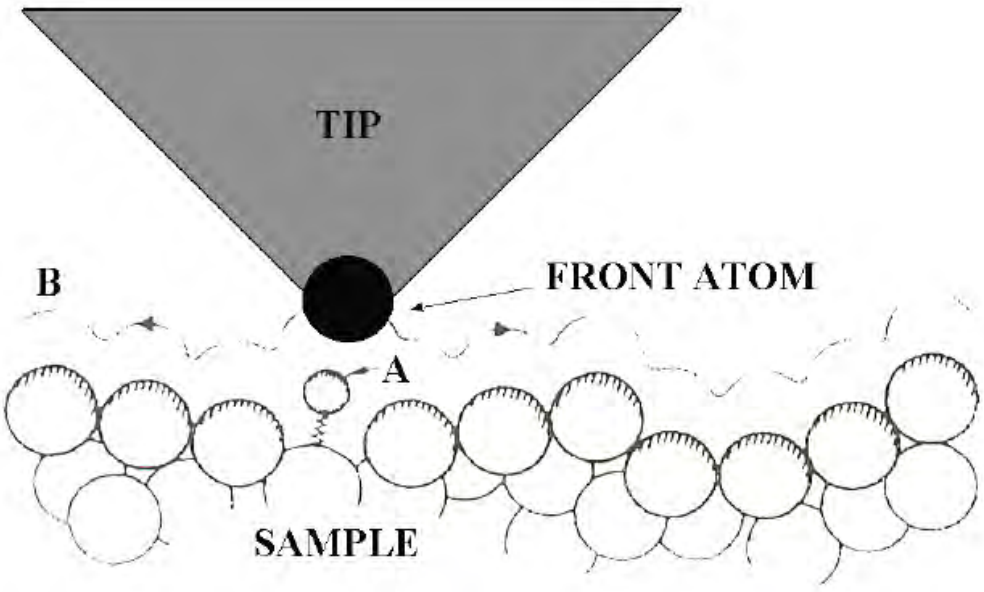

Figure 3.4 Principles operation of STM and AFM. The tip follows contour B, in one case to keep the tunneling current constant (STM) and in the other to maintain constant force between tip and sample (AFM).

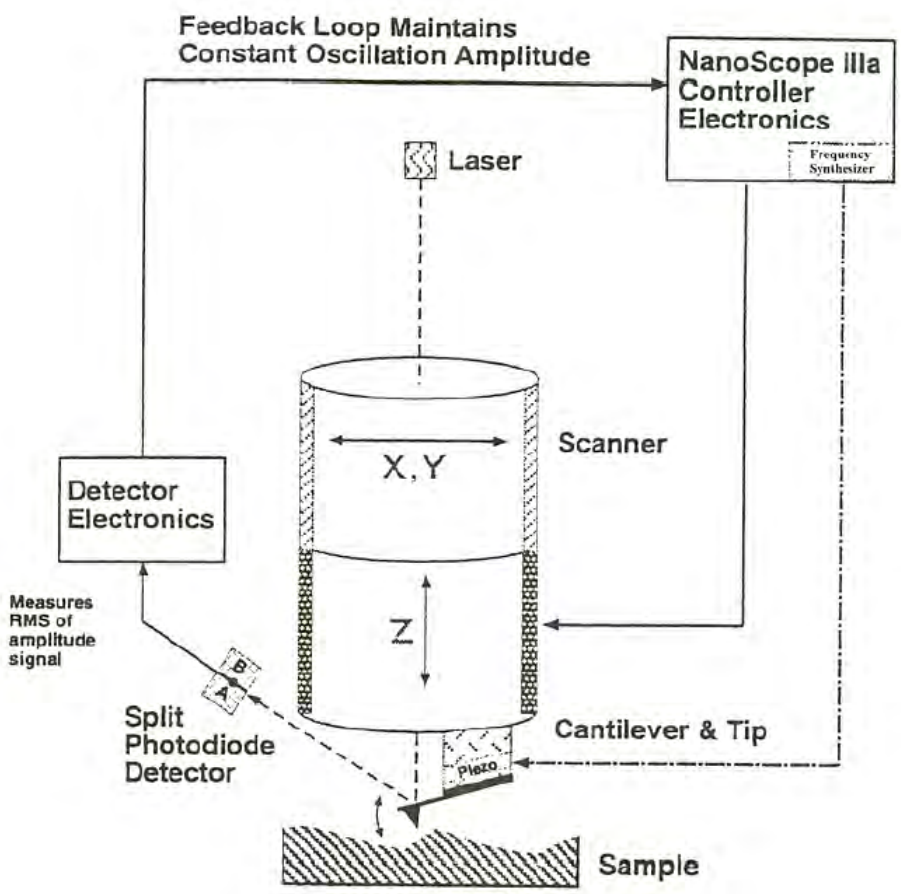

Figure 3.5 AFM working principles.

3.4.1 Feedback operation

The AFM can be operated in two principal ways: with feedback control and without feedback control. If the electronic feedback is switched on, then the positioning piezo, which moves the tip (or sample) up and down, can respond to any changes in force that are detected corresponding to the deflection position of the reflected laser, and alter the tip-sample distance to restore the force to a setpoint value. This mode of operation is known as constant force, and usually enables a fairly faithful topographical image to be obtained (hence the alternative name, height mode). If the feedback system is switched off, then the microscope is said to be operating

in constant height or deflection mode. This is particularly useful for imaging very flat samples at high resolution. Usually it is best to have a small amount of feedback-loop gain, to avoid problems of thermal drift or the possibility of a rough sample damaging the tip and/or cantilever. Strictly, this should then be called error signal mode. The error signal mode may also be displayed while feedback is switched on; this image will remove slow variations in topography but highlight the edges of features.

3.4.2 Operating options

AFM image contrast can be obtained in many ways. The three main classes of operation options are contact mode, tapping mode and non-contact mode. The force distance regime of these three options is shown in Figure 3.6.

Contact mode is the most common operation method of the AFM. As the name suggests, the tip and sample surface remain in contact during the scanning. By "contact" we mean in the repulsive regime of the inter-molecular force curve (see Figure 3.6). The repulsive region of the curve lies above the x-axis. One of the drawbacks of remaining in contact with the sample is that there exist large lateral forces on the sample as the tip is "dragged" over the specimen.

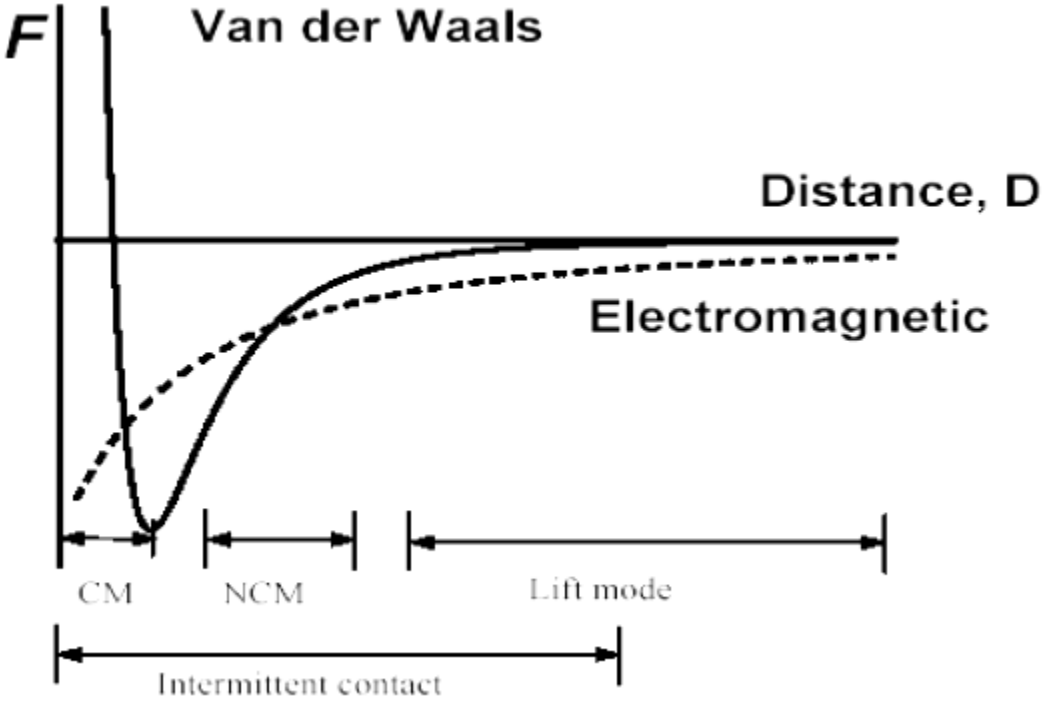

Figure 3.6 Distance dependence of Van der Waals and electrostatic forces compared to the typical tip-surface separations in the contact mode (CM), non-contact mode (NCM), intermittent contact (or tapping) mode, and lift mode. In the last case, the tip cannot acquire topographic information and an additional scan is necessary to position the tip at the required separation from the surface.

Tapping mode (or intermittent contact) is the next most common mode used in AFM. When operated in air or other gases, the cantilever is oscillated at its resonant frequency (several tens to hundreds of kilohertz) and positioned above the surface so that it only taps the surface for a very small fraction of its oscillation period. This is still viewed as 'contact' with the sample in the sense defined earlier, but the very short time over which this contact occurs means that lateral forces are dramatically reduced as the tip scans over the surface. When imaging poorly immobilized or soft samples, tapping mode may be a far better choice than contact mode for imaging. Other methods of obtaining image contrast are also possible with tapping mode. In constant force mode, the feedback loop adjusts so that the amplitude of the cantilever oscillation

remains (nearly) constant. An image can be formed from this amplitude signal, as there will be small variations in this oscillation amplitude due to the control electronics not responding instantaneously to changes on the specimen surface.

Non-contact operation is another possible method which may be employed when imaging by AFM. The cantilever must be oscillated above the surface of the sample at such a distance that we are no longer in the repulsive regime of the inter-molecular force curve. This is a very difficult mode to operate in ambient conditions with the AFM. The thin layer of water contamination, which exists on the surface on the sample under ambient conditions, will invariably form a small capillary bridge between the tip and the sample and cause the tip to "jump-to-contact". Even under liquids and in vacuum, jump-to-contact is extremely likely, and imaging is most probably occurring using tapping mode. All other advanced scanning techniques are based on these three basic methods.

3.4.3 Extended techniques in AFM

The main advanced option based on the contact mode is lateral force microscopy (or friction force microscopy). The earlier discussion of the way in which the bending of the cantilever is detected considered the use of a laser and a split photo-diode. Lateral force microscopy (LFM) uses a 4-segment (or quadrant) photo-diode to enable measurement of the torsion of the cantilever as well. As the cantilever is scanned over the specimen surface (with the cantilever now scanning with its long axis perpendicular to the fast scan direction), variations in friction between the tip and sample will cause the tip to stick / slip during the scan, resulting in twisting of the cantilever.

There are a number of advanced options based on tapping mode, such as magnetic force microscope (MFM) and electrostatic force microscope (EFM). In these two methods one must remove topographical information from magnetic and electrostatic signal. MFM and EFM work by first determining the topography along a scan line, and then lifting a pre-determined distance above the surface to re-trace the line following the contour of the surface. In this way, the tip-sample distance should be unaffected by topography, and an image can be built up by recording changes which occur due to longer range force interactions, such as magnetic forces.

3.4.4 Tip effects

One of the most important factors influencing the resolution which may be achieved with an AFM is the sharpness of the scanning tip. The first tips used by the inventors of the AFM were made by gluing diamond onto pieces of aluminum foil. Commercially fabricated probes are now universally used. The best tips may have a radius of curvature of only around 2nm (carbon nanotubes used as the AFM tip may have an even finer radius). The need for sharp tips is normally explained in terms of tip convolution. This term is often used (slightly incorrectly) to group together any influence that the tip has on the image. The main influences are:

Broadening:

Tip broadening arises when the radius of curvature of the tip is comparable with, or greater than, the size of the feature imaged. Figure 3.7 illustrates this problem. As the tip scans over the feature, the sides of the tip make contact before the apex, and the microscope begins to respond to the feature. This is what we may call tip convolution.

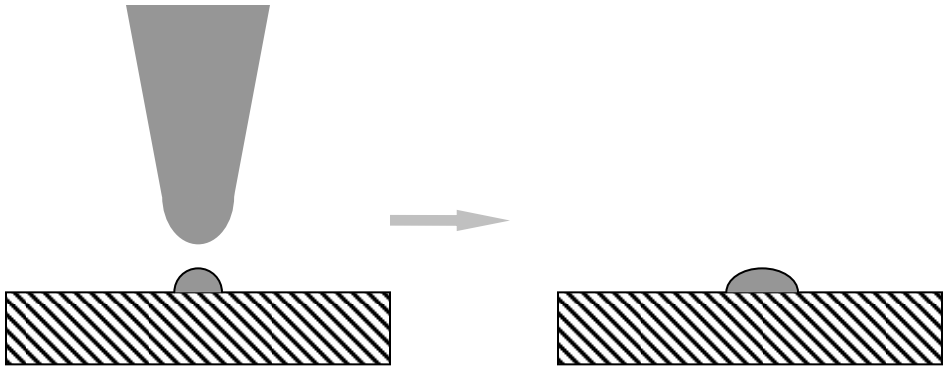

Real physical situation Image

Figure 3.7 Tip broadening effect.

Compression:

Compression occurs when the tip is over the feature being imaged. It is difficult to determine in many cases how important this effect is, but studies on some soft biological molecules (such as DNA) have shown the apparent DNA width to be a function of imaging force. Note that although the force between the tip and sample may only range from nN to μN, the resulting pressure might be MPa to GPa due to the small tip radius.

Interaction forces:

Interaction forces between the tip and sample surface are the source of image contrast with the AFM. However, some changes that may be interpreted as corresponding to the topography may be due to a change in force interaction. Forces due to the chemical nature of the tip are probably most important here, and selection of a particular tip for its material can be important. Chemical mapping using specially treated or modified tips is another important aspect of current research in AFM.

Aspect ratio:

The aspect ratio (or cone angle) of a particular tip is crucial when imaging steep sloped features (Figure 3.8). Electron beam deposited tips have been used to image steep-walled features far more faithfully than can be achieved with the common pyramid tips.

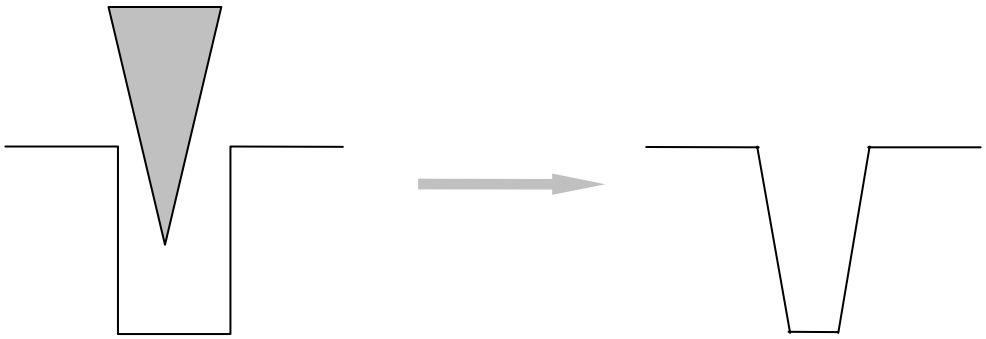

Real physical situation Image

Figure 3.8 Tip aspect ratio effect.

3.5 NANOMECHANICAL MEASUREMENTS

3.5.1 Nanoindenter II system ®

A Nano Indenter® II mechanical properties microprobe (MTS, Oak Ridge TN) equipped with a nanoscratch attachment was used to perform the nanoscratch experiments. Figure 3.9 illustrates the scratch attachment for the Nano Indenter® II. This tangential force option monitors the lateral deflection of the indenter shaft away from its centered position using two proximity probes in the x and y directions, by which the friction coefficient between the scratching tip and the sample surface can be obtained during the scratching process. A Berkovich-shaped diamond indenter with radius about 150 nm was utilized to make the scratches.

As shown in Figure 3.10, the tip can be aligned such that the scan can be performed either along the face-forward or the edge-forward direction. Usually the face-forward orientation was used for the scratching. The indenter tip velocity for the scratch was 1 μm/s. To insure reliability, five scratches were performed on each film.

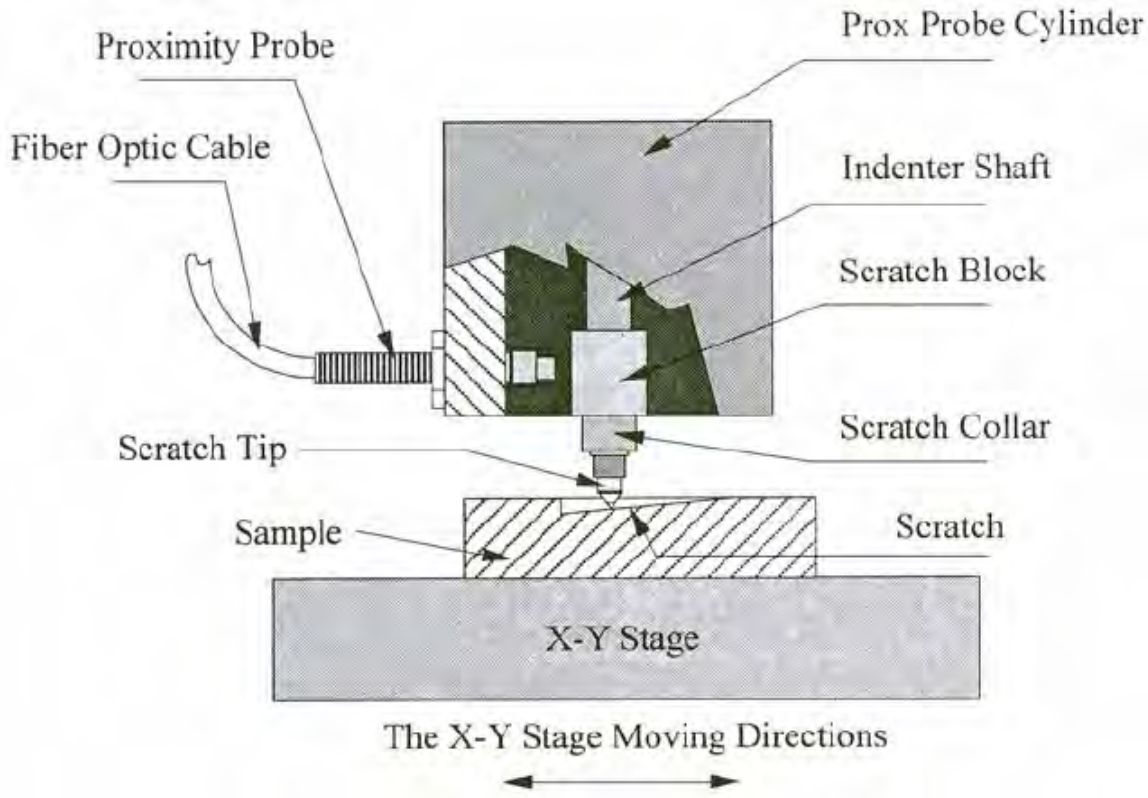

Figure 3.9 Schematic of the scratch attachment of the Nano Intenter® II system.

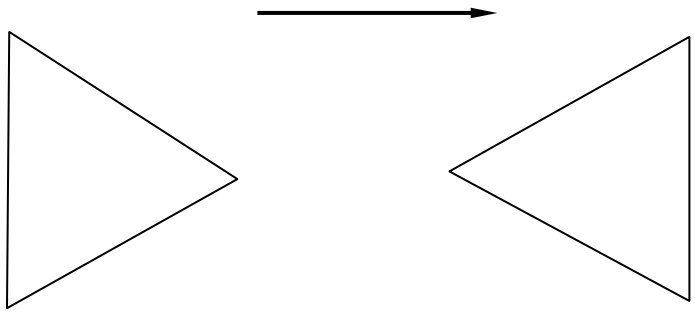

Figure 3.10 Schematic of edge forward (L) and face forward (R) scratches. (arrow indicates scratch direction, triangle indicates tip with alignment orientation).

3.5.2 Hysitron triboscope ®

In the Hysitron TriboScope ® Nanomechanical Testing System, the SPM controller, monitor and the 3-D piezo actuators of an existing commercial Scanning Probe Microscope are used. The heart of the instrument is a specially designed load-displacement transducer developed by Hysitron, Inc. The transducer assembly, which replaces the optical head of the AFM, and its associated hardware, comprise the Hysitron system. The transducer consists of a three plate capacitive structure with electrostatic actuation hardware used for direct application of normal load, and a capacitive sensor for vertical displacement measurements. The operation mechanism of the transducer can be found elsewhere[60] and will not be described here. During a nanoindentation measurement, the tip is lowered towards the sample so that it is positioned close to the sample (ideally less than 100 μm). After waiting for at least 15 minutes to minimize the thermal drift, the tip is engaged to the sample by the stepper motor with a predetermined set point. The surface is imaged using AFM prior to indentation to locate the region of interest. During indentation, the feedback signal is disabled by setting the gains to zero and indentation is

performed using the Hysitron transducer. At the same time, an in situ load-displacement curve is measured and displayed on the video display monitor.

3.6 X-RAY PHOTOELECTRON SPECTROSCOPY (XPS)

XPS is a surface analytical technique commonly used to determine elemental composition and chemistry of the near surface regions of materials. A schematic of the XPS process is shown in Figure 3.11. Essentially, XPS is based on the photoelectric effect described by Einstein in 1905. When the material of interest is subjected to X-rays of sufficient energy (hν) to overcome the work function (φ) of that material, a core (inner shell) level electron will be ejected[61]. Consequently, there will be some atoms lacking electrons in the inner shell from which photoelectrons have been released, causing the material to be partially ionized. To compensate for this ionized state, the atom will undergo one of two processes: relaxation of a higher energy inner shell electron to fill the vacant hole emitting its energy as another photon (florescence) or transfer of that energy to a third electron (Auger electron) causing it to be ejected. Since samples in this research were characterized by photoelectron analysis, the Auger process will not be discussed. The key to chemical identification largely depends on the relative insensitivity of the core electrons deep inside the inner shell to their surroundings and on their retaining the binding energies (EB) that are signatures of that atom type, i.e., number of protons in the nucleus. Using Einstein's photoelectric equation, one may estimate the kinetic energy of emitted photoelectrons (EK):

$$E_K = h\nu - E_B - \phi \qquad (3.1),$$

where hν is the energy of the x-ray photon and ϕ is the work function.

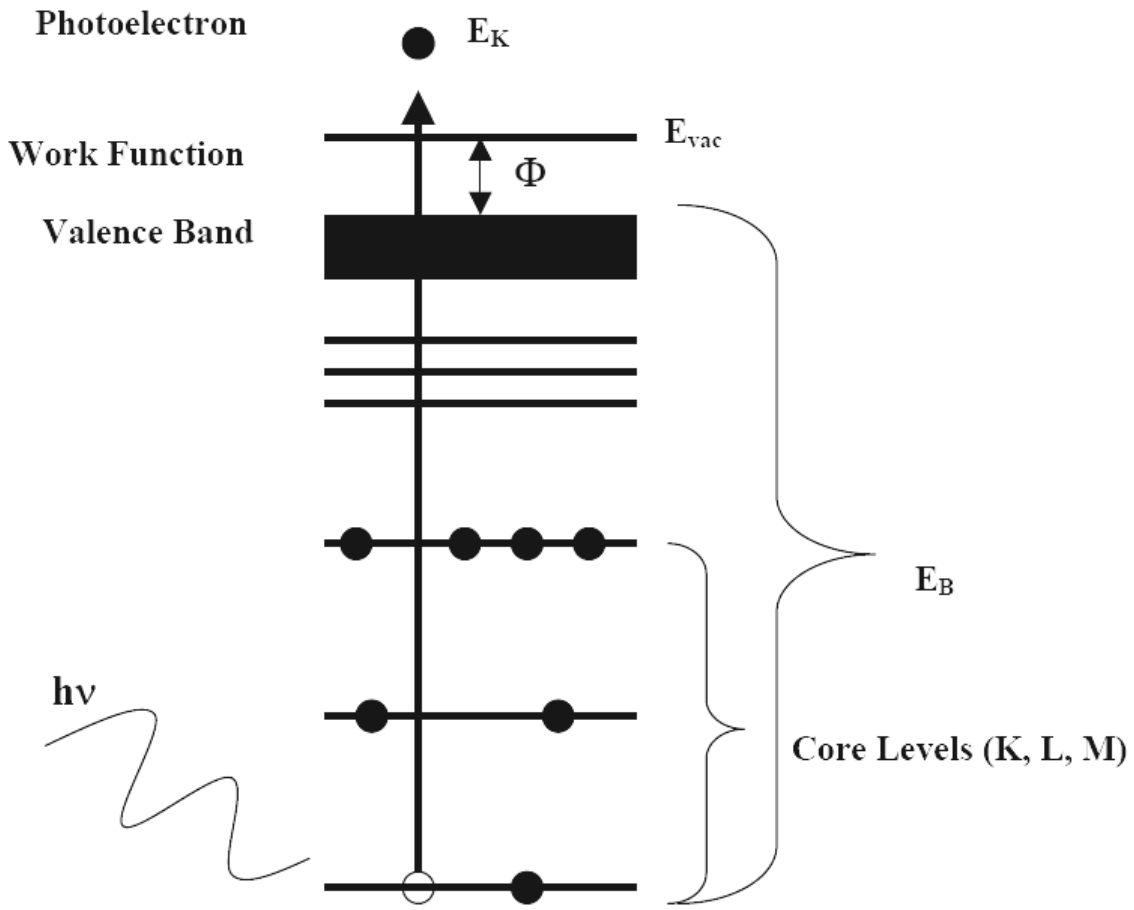

Figure 3.11 Energy level diagram of the process involved in a photoelectron emission from a solid.

By convention, the kinetic energy of a core level photoelectron is measured with respect to the highest occupied level of the solid, the Fermi level, using a hemispherical electrostatic energy analyzer. The analyzer consists of two electrically isolated concentric hemispheres with a potential difference placed between them (the pass energy), thus creating an electrostatic field. This electrostatic field separates photoelectrons by only allowing ejected electrons of the chosen pass energy through to the detector to be measured as a function of their kinetic energy. Electrons with kinetic energy higher than the chosen pass energy will be attracted to the outer negatively biased hemisphere, while electrons exhibiting kinetic energy less than the chosen pass energy are attracted towards the inner positively charged hemisphere and neutralized. The

photoelectron spectrum is achieved by scanning the electron kinetic energy using a retarding plate (negative electrode) to slow down the electrons to the chosen pass energy on the detector.

In this work, all XPS measurements were made using a Kratos Analytical Axis 165 system. The system is equipped with a monochromatic Al K_{α} source (1486.6 eV). Initially, survey spectra were recorded for all samples in the fixed analyzer transmission (FAT) mode, 160 eV pass energy, 1.0 eV/step, and normal takeoff angle. High-resolution narrow band spectra were recorded in the FAT mode, 80 eV pass energy, 0.1 eV/step size, and normal take off angle. Peak deconvolution was performed using standard Kratos software with Shirley background correction when area under the curve calculations was done. However, for viewing purposes, XPS peaks in this dissertation are shown with linear backgrounds. Sample charging was corrected by referencing the Si 2p to 99.3 eV (when applicable, the Au 4f spectral region was used as the reference) and shifting all other features accordingly[62].

3.7 TRANSMISSION ELECTRON MICROSCOPY

A JEOL JEM 200 CX TEM and JEOL JEM 2000 FX STEM were used for high magnification grain structure imaging and grain size distribution analysis as well as electron diffraction experiments. The basic principles of TEM[63] are summarized below. As the electrons travel through the specimen, they are either scattered by a variety of processes or they may remain unaffected by the specimen. The end result is that a nonuniform distribution of electrons emerges from the exit surface of the specimen, as shown schematically in Figure. 3.12. It is this nonuniform distribution that contains all of the structural and chemical information about the specimen. The TEM is constructed to display this nonuniform distribution of electrons in two

ways. First, the spatial distribution of scattering can be observed as contrast in images of the specimen (Figure 3.12 (a)), and the angular distribution of scattering can be viewed in the form of Diffraction Patterns (Figure 3.12 (b)). A simple operational step in the TEM is to use a restricting aperture of a size such that it selects electrons that have suffered less than a certain angular deviation.

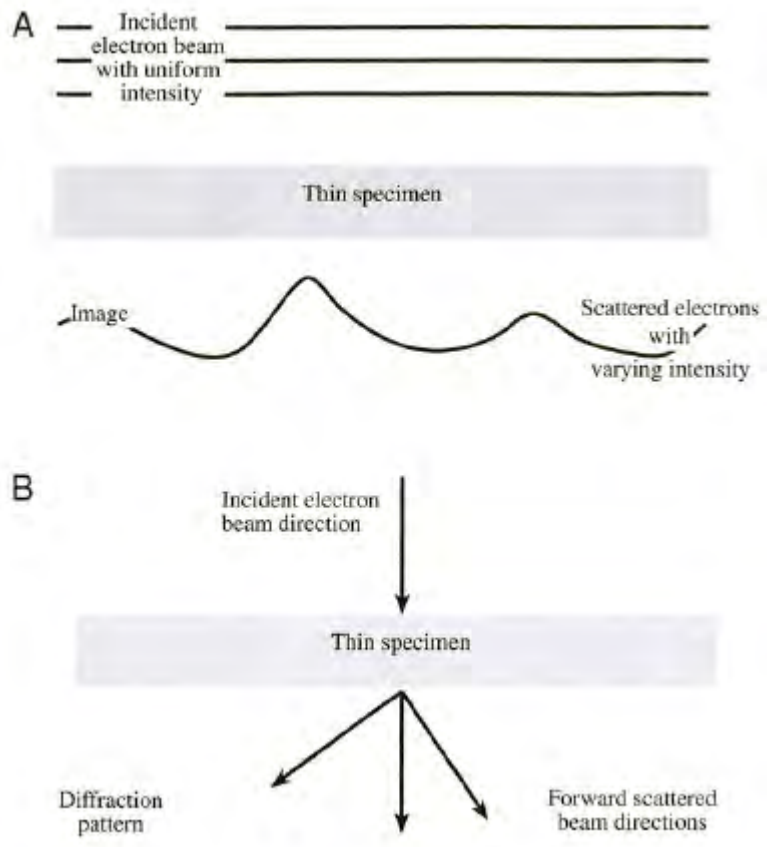

Figure 3.12 (a) A uniform intensity of electrons, represented by the flat line, falls on a thin specimen. Scattering within the specimen changes both the spatial and angular distribution of the emerging electrons. The spatial distribution (intensity) is indicated by the wavy line. (b) The change in angular distribution is shown by an incident beam of electrons being transformed into several forward-scattered beams.

Figure 3.13 shows how this operation is achieved in a TEM to obtain the diffraction patterns and images. To see the diffraction pattern, the imaging system lenses should be adjusted so that the back focal plane of the objective lens acts as the object plane for the intermediate lens. Then the diffraction pattern is projected onto the viewing screen (See Figure 3.13 (L)). To see the image, the intermediate lens should be readjusted so that its object plane is the image plane of the objective lens. Then the image is projected onto the viewing screen (See Figure 3.13 (R)).

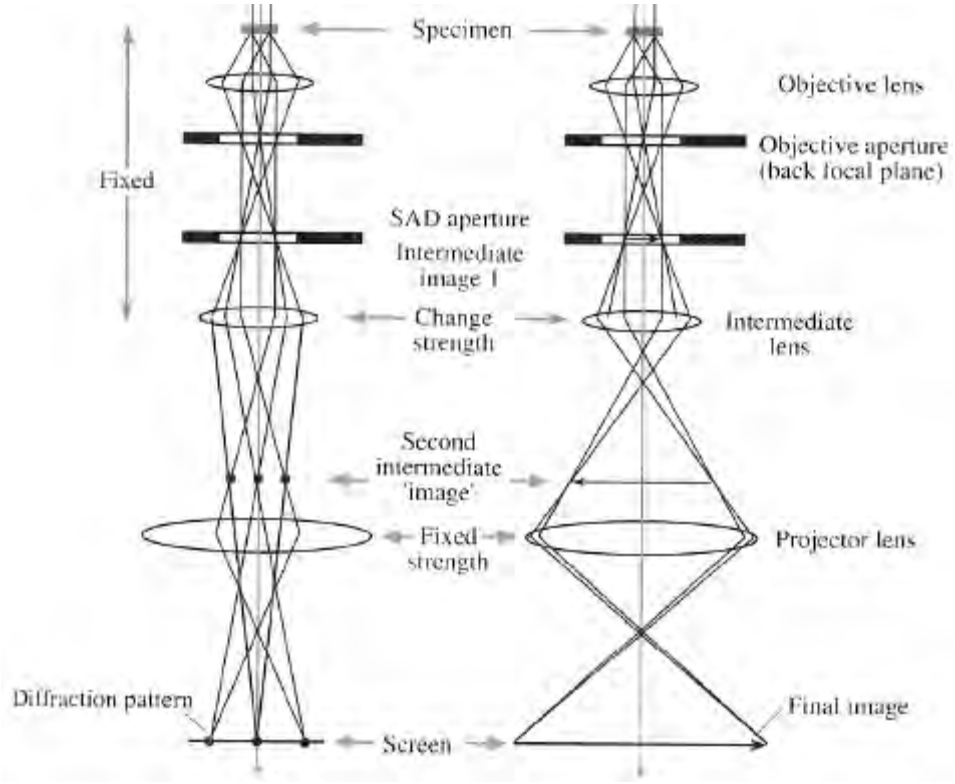

Figure 3.13 Two basic operations of the TEM imaging system involve (L) projecting the diffraction pattern on the viewing screen and (R) projecting the image onto the screen. In each case the intermediate lens selects either the back focal plane or the image plane of the objective lens as its object.

3.8 OTHER EXPERIMENTAL TECHNIQUES

Listed below are other standard experimental techniques for materials characterization that have been used in the dissertation. The detailed principles of operation can be found elsewhere.

X-ray Diffraction (XRD)[64] and X-ray Reflectivity (XRR)[65-67]: A Philips X'Pert-MRD system with Cu Kα radiation and in line focus is used.

Scanning Electron Microscope (SEM)[68]: The SEM experiments are carried out in a Philips XL 30 scanning electron microscope.

Ellipsometer[34]: A Variable Angle Spectroscopic Ellipsometer from J. A. Woollam Co. Inc® is used.

4.0 DISSERTATION PROPOSAL PROJECTS

4.1 DENDRIMER MONOLAYERS AND INTERFACIAL INTERACTIONS (CHAPTER 5)

The interaction of metals with organic layers (e.g., metalized polymers) has received considerable attention due to its importance in determining the reliability and durability of many technological devices and its relevance to future applications based on hybrid organic/inorganic nanoscale systems. The interaction of ultrathin (< 20 nm) metal layers with dendrimer monolayers adsorbed on the native oxide of silicon wafers has also been studied to a limit extent. Among the findings to date are significant reductions in the roughness of deposited metal films mediated by dendrimer monolayers[34]; a substantial increase in the nanomechanical hardness of ultrathin Au when deposited on a dendrimer adlayer[31]; and the occurrence of interfacial reactions, including the formation of metal nitrides, following deposition of reactive metals such as Co and Cr on amine-terminated dendrimer monolayers[33, 34]. To date there has been no systematic study of the role of dendrimer mediation on nanotribology, e.g., the nanoscratch behavior of thin metal films with and without a dencrimer interlayer, as schematically shown in Figure 4.1. Many potential applications of dendrimer mediation will involve intentional or unintentional sliding contact and the presence of a dendrimer monolayer may well influence nanoscratch behavior.

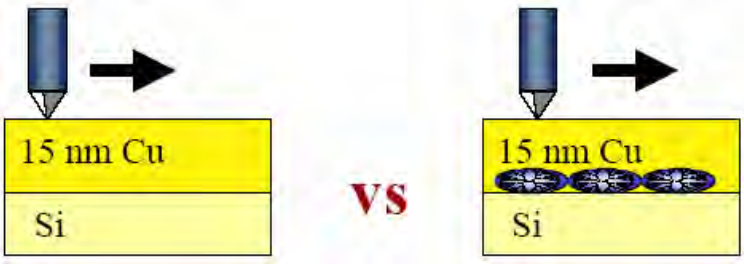

Figure 4.1 Schematic of nanoscratch experiments on dendrimer free and dendrimer mediated metal films.

In this work commercially available PAMAM (polyamido-amine) dendrimers are used. These amine-terminated dendrimers spontaneously adsorb from μmol ethanolic solutions onto SiOx forming complete, densely packed, self-limiting monolayers (denoted Gn/Si, where n is the generation number)[32]. Subsequent sputter deposition of metal onto the monolayer yields hybrid dendrimer/metal nanocomposite ultrathin films[39]. A comparative study of the nanoscratch response of Cu/Si versus Cu/G8/Si and Cr//Si versus Cr/G8/Si is carried out in Chapter 5.

4.2 DENDRIMER DOMAIN FORMATION (CHAPTER 6)

As previously mentioned, flat, complete monolayers of dendrimers formed on technologically interesting substrates can be realized by using standard cleaning, dipping, and rinsing procedures[32, 41, 42]. By contrast, the self-organized growth of complex submonolayer dendrimer patterns observed when finite volumes of dendrimer solution are cast on a substrate in a thin layer and allowed to evaporate[44-47] has received comparatively little attention. A thorough understanding of dendrimer/substrate interactions and their effect on dendrimer attachment/detachment, surface mobility, and layer growth (mode and kinetics) is lacking. The basic physical picture envisaged for dendrimer layer growth by immersion of a substrate into a dendrimer containing solution is that isolated dendrimer molecules in solution randomly adsorb

on the substrate surface. Dendrimer molecules progressively fill the surface forming a dense monolayer. Simultaneous or subsequent multilayer formation also may occur. Rinsing of these films removes the more loosely bound dendrimers leaving behind a flat and uniform monolayer.

The situation is more complicated for thin cast films where the reservoir of dendrimer molecules is finite and dendrimer attachment at the substrate occurs during evaporation and eventual dewetting. In this case, reduction of the fluid film thickness through evaporation leads to the onset of dewetting[69-72] via nucleation of holes (dry patches). For the case of an evaporating dendrimer solution it is not clear to what extent the forces associated with the dewetting phenomena influence the final dried dendrimer structure.

In this dissertation aerosol deposition is used to generate thin fluid dendrimer solution films which yield complex and diverse two-dimensional patterns on drying as shown in Figure 4.2. Two different solution systems are used. One is standard PAMAM G4 in ethanol solution; another is 25% C_{12} PAMAM G4 in pentanol solution. There are two main distinctions: (1) pentanol evaporates much slower than ethanol - at 25°C, the vapor pressure of ethanol is 7.9 kPa while that of pentanol is only 0.33 kPa; and (2) in 25%C_{12} PAMAM G4 the 2-hydroxydodecyl chains replace 25% of the NH_2 terminal groups which may modify the dendrimer molecule / substrate interaction. The difference in both evaporation rate and the strength of the molecular adsorption to substrate may lead to different observed domain formation mechanisms. The dewetting mechanism may be expected to dominate the formation of the final dried dendrimer patterns in the fast evaporated ethanol and standard PAMAM G4 solutions. In the slower evaporating pentanol using the stronger molecule / substrate interactions found in 25%C_{12} PAMAM G4 systems, dendrimer domains may be stable against the dewetting forces. Chapter 6 explores the relevant issues in dendrimer assembly during evaporation and demonstrates the

importance of electrostatic interactions. A study of charge patterning, motivated by the results in Chapter 6 is described in Appendix A and summarized below in section 4.4.

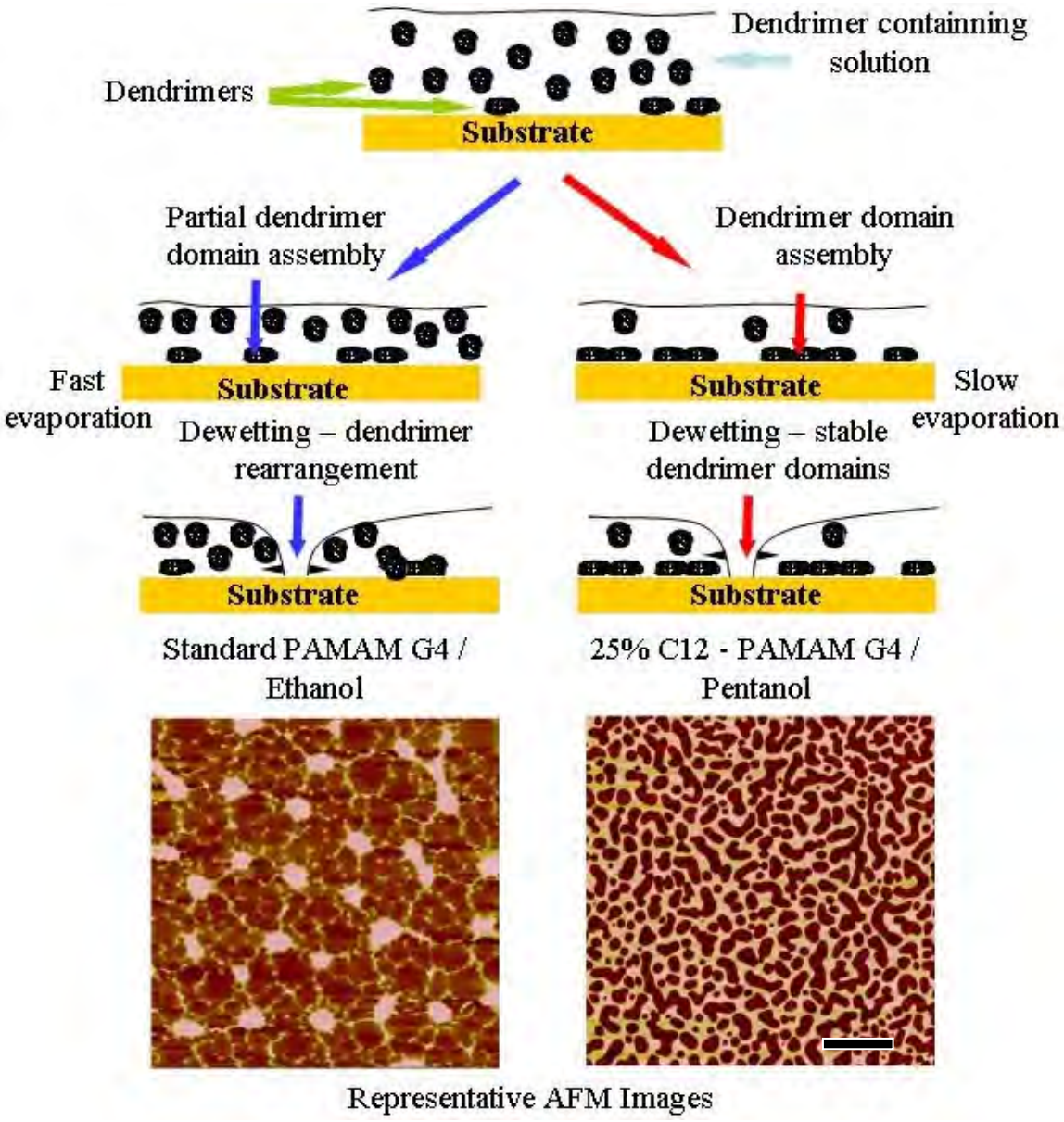

Figure 4.2 Dendrimer domain formation schematics. (Lower shown are two typically AFM images formed by the methods described above). The bar marks 2 μm.

4.3 PHYSICAL INTERMIXING (CHAPTER 7)

As summarized in Section 4.1, we have examined the interaction of ultrathin (< 20 nm) metal layers with dendrimer monolayers adsorbed on the native oxide of silicon wafers. Subsequent vapor or sputter deposition of metal onto the monolayer yields hybrid metal/dendrimer/substrate with surprising physical and mechanical behavior – including nanohardness, surface roughness, nanoscratch mechanisms, etc. The effects observed are likely related to at least partial penetration of the deposited metal into the dendrimer underlayer. Preliminary analysis of the penetration by X-ray Photoelectron Spectroscopy (XPS) analysis and Atomic Force Microscopy (AFM) profilometry has been reported [33, 34]. In chapter 7 the work summarized in Sections 4.1 and 4.2 will be combined to study the physical interpenetration of Au into discontinuous dendrimer monolayers. This method conveniently allows for simultaneous metal film formation on both the bare substrate and the dendrimer monolayer on a single sample, as shown in Figure 4.3. The upper part of Figure 4.3 schematically illustrates dendrimer patterns with monolayer thickness made by aerosol spray deposition. The lower part of Figure 4.3 schematically illustrates Au deposition onto the monolayer dendrimer domains. The physical intermixing between metal overlayers and dendrimers is studied directly by AFM-based step height and force measurements for different metal film thicknesses.

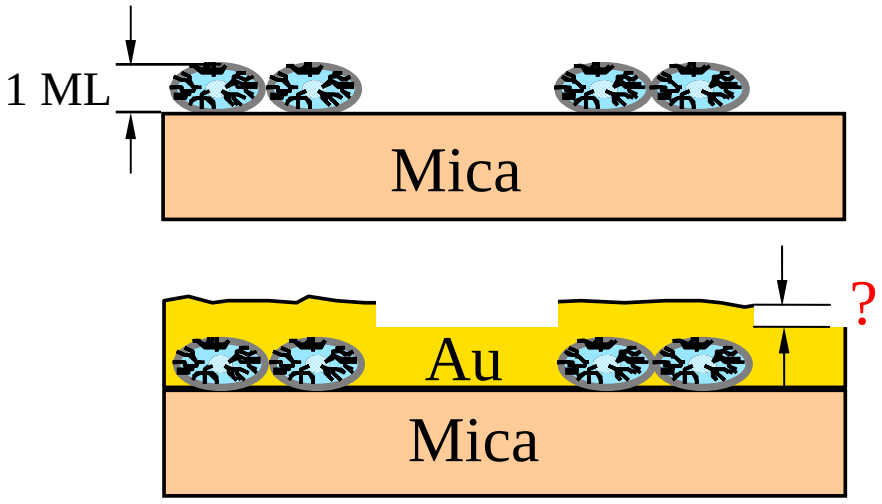

Figure 4.3 Physical intermixing between metal overlayers and dendrimer monolayer domains.

4.4 CHARGE PATTERN OF GRANULAR THIN FILMS (APPENDIX A)

The importance of electrostatic interaction in monolayer dendrimer domain formation revealed in Chapter 6 motivated a study of charge patterning in granular materials found in Appendix A. This feasibility study demonstrates that metal nano-granules embedded in an insulating matrix can store charge locally and with great stability and may serve to direct assembly of charged objects, such as protonated dendrimer molecules. This concept is illustrated in Figure 4.4.

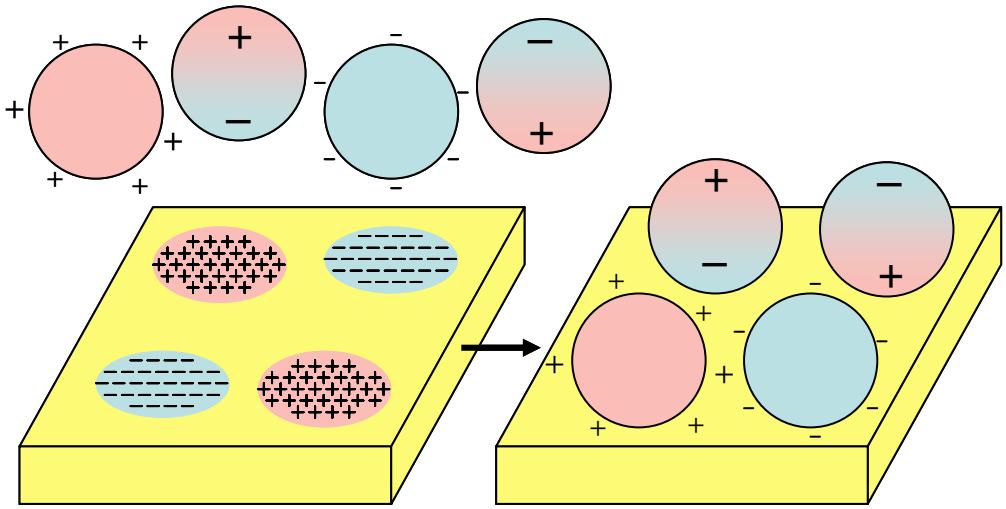

Figure 4.4 Schematic of charge-patterned assembly of charged/polarized objects.

5.0 RESULTS PART 1 – DENDRIMER MONOLAYERS AND INTERFACIAL INTERACTIONS

5.1 INTRODUCTION

As reviewed in Chapter 2, dendrimers are three-dimensional, globular, highly branched macromolecules made up of a central core surrounded by repetitive units all enclosed by a terminal group "shell". They can be synthesized with highly controllable sizes determined by the core type, extent of branching, and nature of the end groups, in the range from ~1 - ~10 nanometers in diameter[1, 2]. They have received intensive interest associated with their variable size, the controllable chemistry of their surfaces, and their potential for serving as the host for metal (and other) nanoparticles. Dendrimers also readily form monolayers on technologically interesting substrates using simple cleaning, dipping, and rinsing procedures.

Dendrimer monolayers are just beginning to receive attention with regard to their adhesive and frictional behavior and related potential applications. The unique nanomechanical and nanotribological properties recently reported for dendrimer-mediated metal ultrathin films suggest their potential for utilization in novel protective coatings. For example, Crooks and co-workers explored the use of amine-terminated PAMAM dendrimer monolayers as adhesion layers for 200 nm Au on SiO_x. They pointed out that organic adhesion layers might be useful alternatives to metallic interlayers. Metallic interlayers may interdiffuse and form intermetallic compounds, adversely affecting physical properties. In addition, relatively simple solution phase deposition might be preferable to more technically demanding methods for forming the

interlayer. It was demonstrated that the amine-terminated dendrimers do provide an adequate adhesion layer for Au. Street, et al reported significant improvements in the nanomechanical / nanotribological response of ultrathin metal/dendrimer composites prepared on Si (100) substrates. For example, the hardness of ultrathin (12.5 nm) Au films was observed to increase nearly two-fold when a dendrimer intermediate layer (adlayer) was added between the metal and the underlying substrate. This effect has been tentatively attributed to the compressed nature of the dendrimer interlayer. The surface roughness also decreased from 1.2 nm to 0.4 nm when a dendrimer monolayer was used to "mediated" the Au film growth[31]. In this case it was proposed that the dendrimer layer enhanced the wettability of the substrate and limited the diffusion of Au atoms which might otherwise lead to agglomeration and increased surface roughness.

Recently, ramped load scratch tests showed that scratch load-bearing capacity was improved by the presence of a dendrimer monolayer used to mediate the growth of 10 nm Ti thin films[39]. Moreover, larger critical loads were observed in films containing a higher generation dendrimer (larger dendrimer molecules). This observation may favorably impact the application of dendrimer-mediated Ti metallic films as tribo-materials or protective layers. Despite the promising preliminary observations of enhanced scratch resistance, it is fair to say that the details of the scratch mechanism have yet to be elucidated in dendrimer-mediated films. This Chapter will focus on developing a comparative understanding of the operative scratch mechanisms for dendrimer-mediated and dendrimer-free metal thin films, as shown schematically in Figure 5.1.

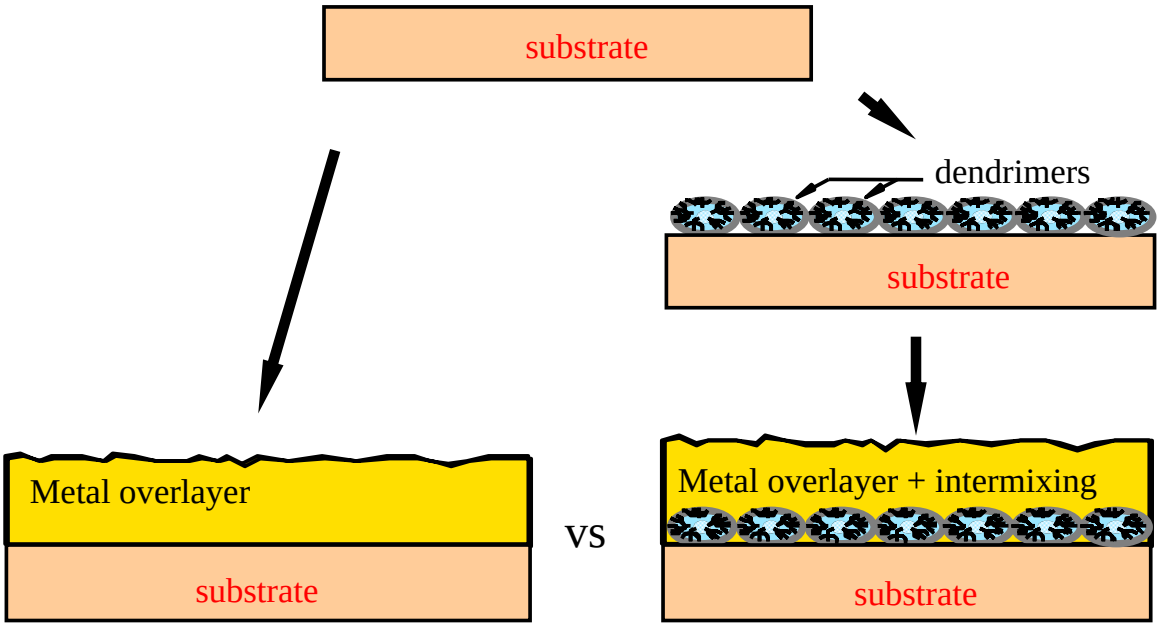

Figure 5.1 Sample schematic illustrating the substrate, dendrimer monolayer, and dendrimer-free and dendrimer-mediated metal overlayer films.

5.2 NANOSCRATCH BEHAVIOR IN DUCTILE MATERIALS

Two elemental metal films were selected for study – Cu and Cr. Cu is expected to be relatively inert with respect to chemical interactions with dendrimer molecules while Cr is likely to be comparatively reactive (for metal nitride formation). Keeping in mind that Cu and Cr arrive at the substrate atomically dispersed, the opportunity for interaction with any mediating molecular layer is high. The difference in intrinsic reactivity highlighted here should be helpful in determining the potential role of chemical interaction between metal overlayers of various types and dendrimer monolayers on the observed scratch mechanisms.

The generally accepted classification of scratch mechanisms in ductile metal films (high purity Cu and Cr are ductile in this sense) are plowing, wedge formation, and cutting[73], as shown

in Figure 5.2. All three scratch modes result in a certain amount of plastic deformation. It is important to note that these mechanisms have been developed in the context of 'macroscopic' wear and their application to very thin films, very sharp scratch tips, and very small loads is still in its early stages. As such, the three scratch mechanisms are more descriptive than quantitative in nature.

Plowing:

During the *plowing* scratch, the motion of the loaded tip creates a permanent trench in the near surface region by lateral displacement of material to the sides (perpendicular to the scratch direction). Plowing usually occurs for light loads and thus for many applications involving 'bulk' materials does not result in serious damage.

Wedge formation:

When the ratio of the shear strength of the contact interface relative to the shear strength of the bulk rises to a sufficiently high level (from ~ 0.5 to ~ 1.0), it has been found that the *wedge* formation mechanism will begin to supplement or replace the *plowing* mechanism. A *wedge* of material is developed at the front of the moving abrasive tip. This wedge will increase in volume as the scratch proceeds. In the wedge mechanism, the total volume of material displaced from the scratch trench is greater than the volume of material displaced to the sides. Wedge formation reflects more aggressive loading conditions but is still considered a fairly mild form of abrasive wear in bulk systems.

Cutting:

Cutting is the most severe form of wear for ductile materials. During the *cutting* process, the abrasive tip removes a 'chip' in a fashion analogous to bulk machining processes. Cutting

results in complete removal of material, but leads to very little displacement of material relative to the size of the scratch trench.

During a scratch process involving a sharp tip, there is critical angle between the scratch tip and the surface being scratched at which the plowing mechanism can transform to the cutting mechanism. This critical angle depends on the material being abraded. It has been shown that the critical angles range from 45° for copper to 85° for aluminum[73].

There are a variety of material characteristics that have been shown to either have an effect on or correlate with abrasive wear. Some of these properties are[73]

Hardness:

There is a linear relationship between hardness of worn surface and wear resistance (different slopes for pure materials and alloys).

Crystal structure:

It has been shown that cubic metals wear at about twice the rate of hexagonal metals, which was attributed to the lower work-hardening rate of hexagonal metals.

Microstructure:

The higher the strain hardening and the ductility, the better the wear resistance. A common way to improve wear resistance is to produce a second phase.

Nature of the Tip:

Changing the abrasive will change the wear rate. Characteristics of the abrasive that will contribute are the scratch angle, hardness, as well as the toughness of the abrasive tip. When the hardness of the abrasive exceeds that of the worn material, wear will become much worse. And a tough abrasive will induce more wear.

Temperature:

One generally expects more wear as the temperature increases. This has been attributed to the fact that small areas of contact are heated during abrasion. The metal will flow at these contact points. For high initial temperatures, the flow stress will be reduced, which will result in less heating due to abrasion. The result will be that the points of abrasive contact will have a similar steady state temperature regardless of initial temperature. Thus, the wear rates will be similar.

Speed of contact:

The wear rate increases slightly with increased speed in the range 0–2.5 m/s. This may be attributed to a slight increase in frictional heating.

Normal load:

Wear is proportional to applied load as long as the load levels do not lead to fracture of the abrasive. In this case, the wear rate will decrease if the abrasive is rounded or may increase if the fractured abrasive has sharp corners.

Humidity:

The effect of humidity on wear rates is far from clear. Results are often contrary. All of our tests were conducted in standard ambient laboratory conditioned air but there was no direct control of humidity or temperature.

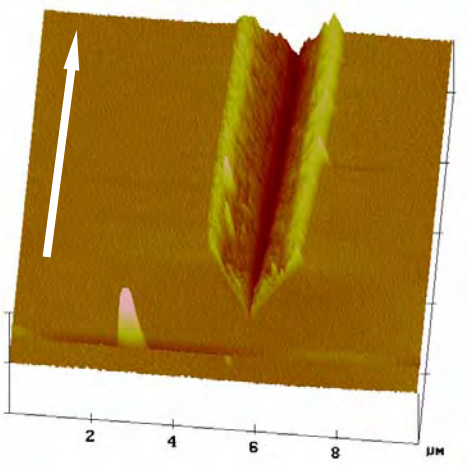

(a)

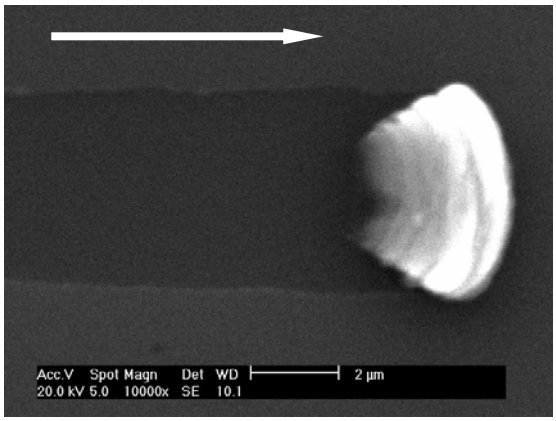

(b)

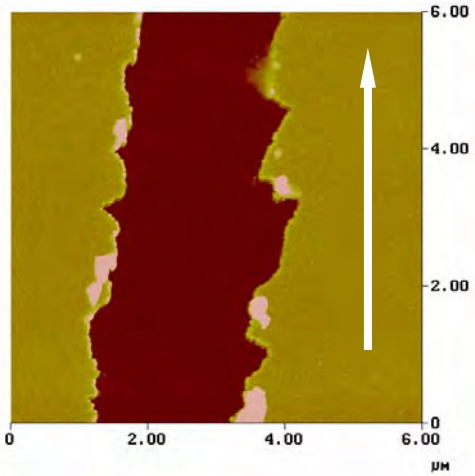

(c)

Figure 5.2 Typical observations of scratch mechanisms in plastic materials (a) plowing, (b) wedge, and (c) cutting.

5.3 NANOSCRATCH BEHAVIOR OF CU FILMS

5.3.1 Metal film deposition

The methods used to fabricate a dendrimer monolayer have been reviewed previously. Here the metal film deposition is summarized. A 99.99% Cu (or Cr) target was used to make the Cu (or Cr) thin films by DC magnetron sputtering at a power density of 1.97 W/cm^2 yielding a deposition rate of 1.8 Å/s for Cu and 2 Å/s for Cr, respectively. The distance between the target and substrate is 50 mm. The base pressure was 3.1×10^{-5} Pa ($2.3\cdot10^{-7}$ Torr). The working gas is 99.999% Ar and the working pressure is 5mTorr. The behavior of ~ 15 nm thick Cu films and ~ 12 nm thick Cr films sputter deposited on the native oxide of silicon wafers, with and without the presence of a generation 8 (G8) PAMAM dendrimer monolayer, are presented here. This work describes the core results of the first nanotribological tests performed on dendrimer-mediated metal films.

5.3.2 X-ray reflectivity characterization

The thicknesses of the films were determined by X-ray reflectivity (XRR) experiments and appropriate curve fitting, as seen in Figure 5.3. XRR is one of the few techniques in thin-film characterization that, with high accuracy, can provide quantitative insight into film thickness, density, and rms roughness of each constituent layer[65-67]. XRR has also been utilized in investigating the oxidation of thin films[74-77] and bulk materials[78]. It is highly sensitive only to the electron density gradients in the system of interest, irrespective of the crystalline nature[66]. The curve-fitting simulations were conducted by using the Philips Win-GIXA program[79] which adopts the Parratt formalism[80] to calculate the reflectivity.

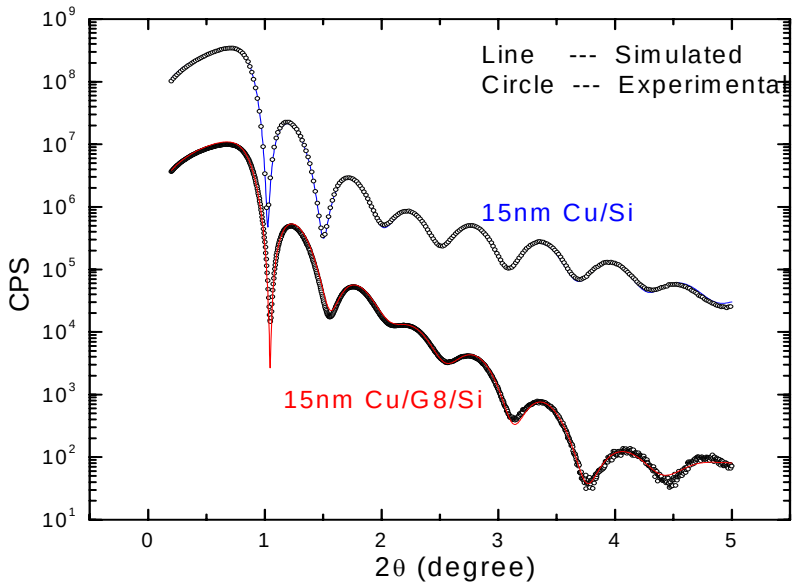

Figure 5.3 The X-ray reflectivity experimental data and fit for 15 nm Cu films on Si with and without dendrimer interlayers.

The results extracted from the fitting procedures are shown in Table 5.1. The two sample types, with and without a dendrimer interlayer, are denoted Cu/G8/Si and Cu/Si. The calculated thicknesses of the films are close to the nominal 15 nm, indicating that the calibration of the sputtering rate was correct. In Cu/G8/Si films, a mixed layer (~ 1.1 nm thick) of Cu and dendrimer is introduced to obtain the optimum fit. (The nature of the mixing can be found in Chapter 7). The density of the mixed layer is 7.04 g/cm^3 – about 20% less than that of pure Cu. The likely presence of this mixed layer has also been observed in Au/G8/Si films[31]. Note that both Cu/Si and Cu/G8/Si films have a native copper oxide layer ~ 2 nm thick at the surface of the sample.

Table 5.1 Tabulated XRR data of 15 nm Cu/G8/Si and Cu/Si.

Nominal and proposed layer structure	Thickness (nm)	RMS Roughness (nm)	Density (g/cm^3)
15 nm Cu/Si			
Cu	12.6 ± 0.1	0.8 ± 0.1	8.92 - 0.1
CuO	2.0 ± 0.1	0.6 ± 0.1	4.84 ± 0.1
15 nm Cu/G8/Si			
G8	2.4 ± 0.1	0.4 ± 0.1	1.58 - 0.1
Mixed Layer	1.1 ± 0.1	0.4 ± 0.1	7.04 ± 0.1
Cu	11.1 ± 0.1	0.9 ± 0.1	8.84 ± 0.1
CuO	2.1 ± 0.1	0.9 ± 0.1	4.98 ± 0.1

5.3.3 Nanoscratch characterization of Cu films

Five identical 4 mN constant load nanoscratches, 100 μm long, were made on each sample using a Nano Indenter II mechanical properties microprobe (other loads of the same order produced very similar results and are not reported here). A Berkovich-shaped diamond tip which had been flattened by repeated use in scratch experiments on harder materials was aligned to scratch the surface in a face-forward direction. Figure 5.4 is an atomic force microscope (AFM, Digital Instruments Dimension 3000) image of the residual impression left by the scratch tip in a thick sputtered Cu film after a simple nanoindentation event. The flattening of the tip is apparent; the line of contact between the forward edge of the tip and the sample surface during a scratch is ~ 1.5 μm long. The direction of motion of the tip during the scratch is illustrated by the direction of the arrow. For this set of experiments each scratch was made at a constant tip

velocity of 1μm/s. After scratching, wear tracks were imaged by scanning electron microscopy (SEM, Philips XL30) and AFM.

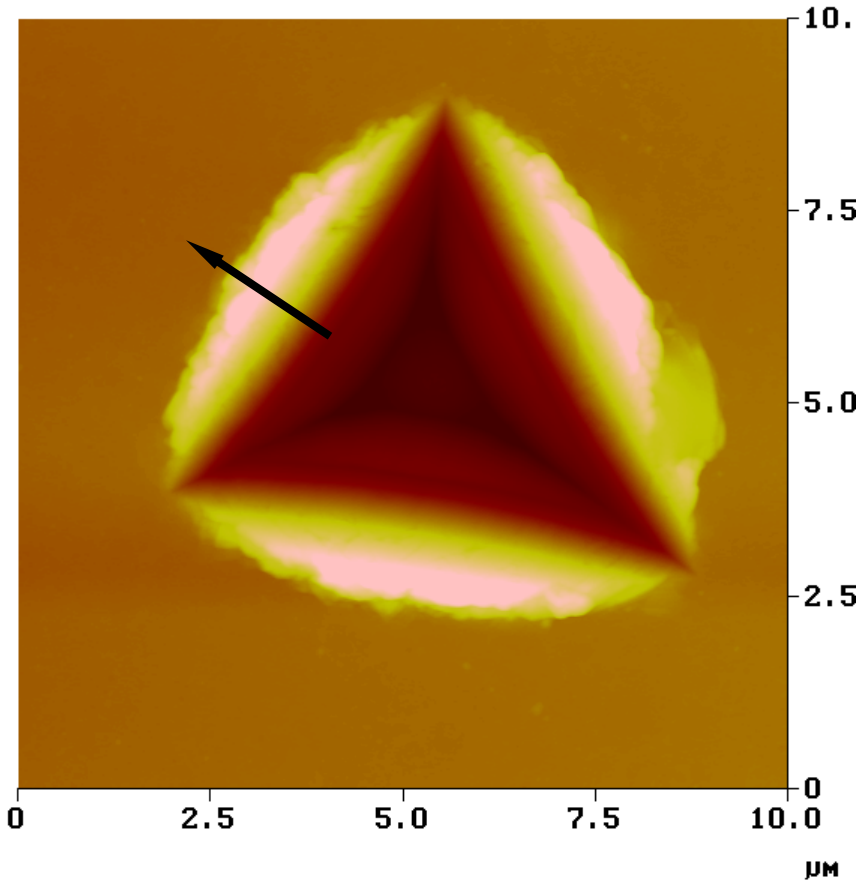

Figure 5.4 AFM image of the residual impression left by the scratch tip in a thick (~ 200 nm) sputtered Cu film after nanoindentation.

SEM images of the regions containing the two sets of five scratches, all made using identical 4 mN constant load conditions, appear in Figure 5.5. Panel (a), shows the nanoscratch wear tracks generated on dendrimer-free Cu/Si, while panel (b) shows the nanoscratches found on dendrimer-mediated Cu/G8/Si. In the absence of a dendrimer interlayer, the scratches are highly regular, with systematically increasing wear track width as the scratch front proceeds from left to right. At the end of each scratch, rounded pile-ups of material are clearly observed,

left behind after unloading and withdrawal of the scratch tip. These observations are consistent with abrasive wear of a ductile metal by a combination of plowing and wedge formation mechanisms[73], as discussed above. By contrast, when Cu deposition is mediated by a dendrimer monolayer the appearance of the wear tracks is completely different Figure 5.5 (b). The wear track widths do not increase as the scratch proceeds, the wear track edges are not smooth, significant material debris is left along the wear track, and the pile-ups, when present, are much less regular. In addition, material removal is inconsistent. Even on the basis of these plan-view SEM images it is apparent that the operative wear mechanism has clearly been dramatically altered by the presence of the dendrimer monolayer.

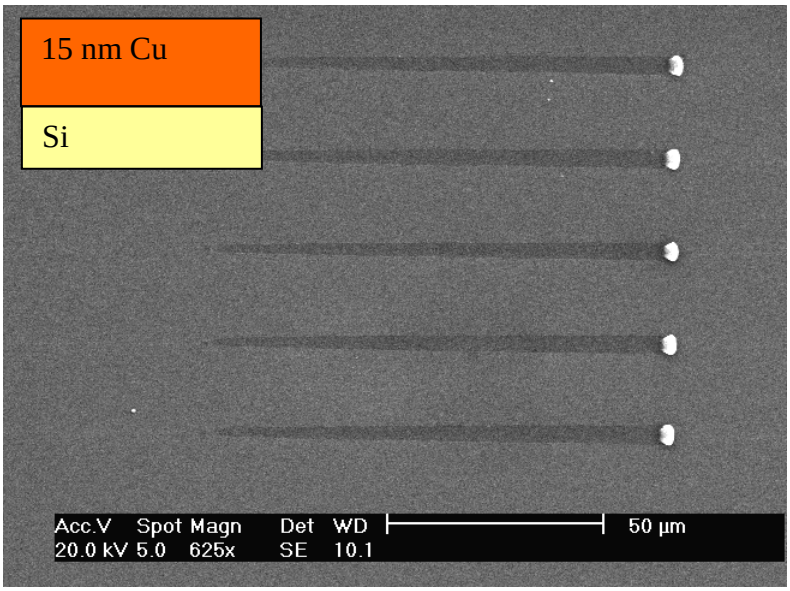

(a)

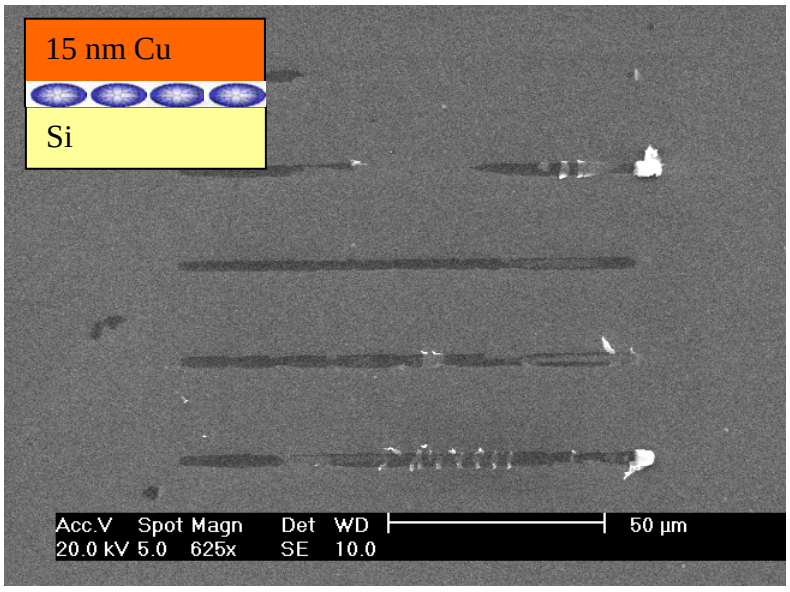

(b)

Figure 5.5 SEM images of sets of nanoscratches carried out at 4 mN constant load; a) Cu/Si, b) Cu/G8/Si.

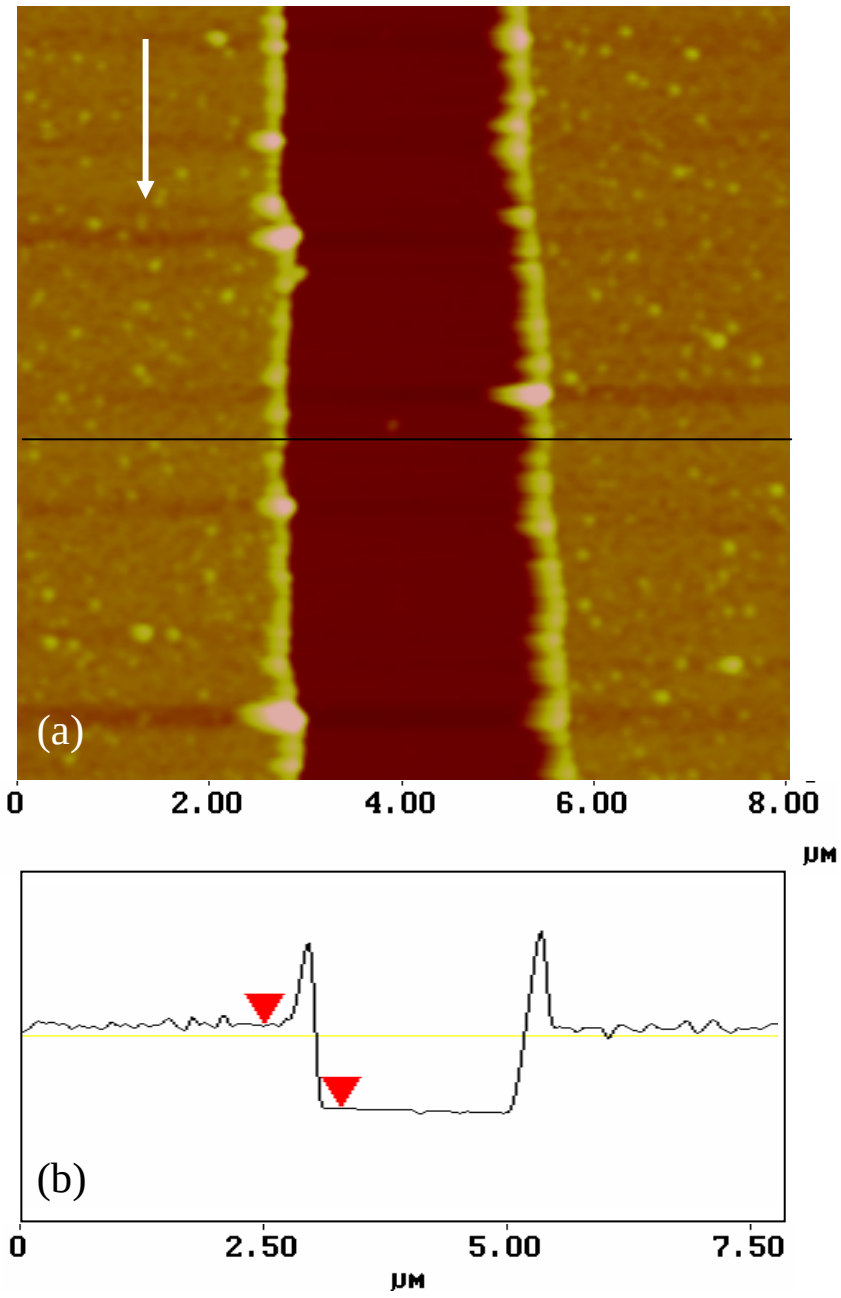

Figure 5.6 AFM images of Cu/Si wear tracks; (a) plan view, (b) cross-sectional line scan.

A much clearer picture of the differences in the wear of Cu/Si versus Cu/G8/Si is provided by AFM imaging of specific sections of the wear tracks. Figure 5.6(a) shows a plan view AFM image of a segment of a wear track on the Cu/Si sample. This segment is from the

narrower end of the track toward the beginning of the scratch. Figure 5.6(b) is a representative AFM line scan through the scratch, perpendicular to the scratch length and direction. Along both edges of the wear track ridges of laterally displaced material are clearly evident confirming that some degree of plowing has occurred. Note that the bottom of the wear track is very flat – in fact flatter than the undisturbed surface of the Cu film. The depth of the track at this point is ~ 16 nm, just slightly thicker than the XRR calculated and calibrated expected thickness of the Cu film. The width of the track at this point is ~ 2.4 μm. Presumably, essentially all of the Cu has been removed from the track leaving the essentially undisturbed surface of the Si wafer at the bottom of the trench. For the loads used in these experiments the deformation is confined to the metal layers – there is no evidence of abrasive wear of the Si substrate or its native oxide. In keeping with the observation of significant displacement of material along the wear track by wedge formation, it is clear that the volume of material in the ridges is much less than the total removed from the track.

Moving further down the same wear track (Figure 5. 7a, b) the trench is now considerably wider (~ 3.8 μm) but the bottom is still very flat. Clear ridges, somewhat higher than those in Figure 5.6b, are again observed. The depth of the track is ~ 17 nm, again just slightly thicker than the Cu film. The approximate angle between the wall of the wear track and the film surface for the Cu/Si samples is found to be ~ 20º, as shown in Figure 5.7b. The mechanism of wear and deformation for Cu/Si remains consistent with a combination of plowing and wedge formation along the length of the scratch.

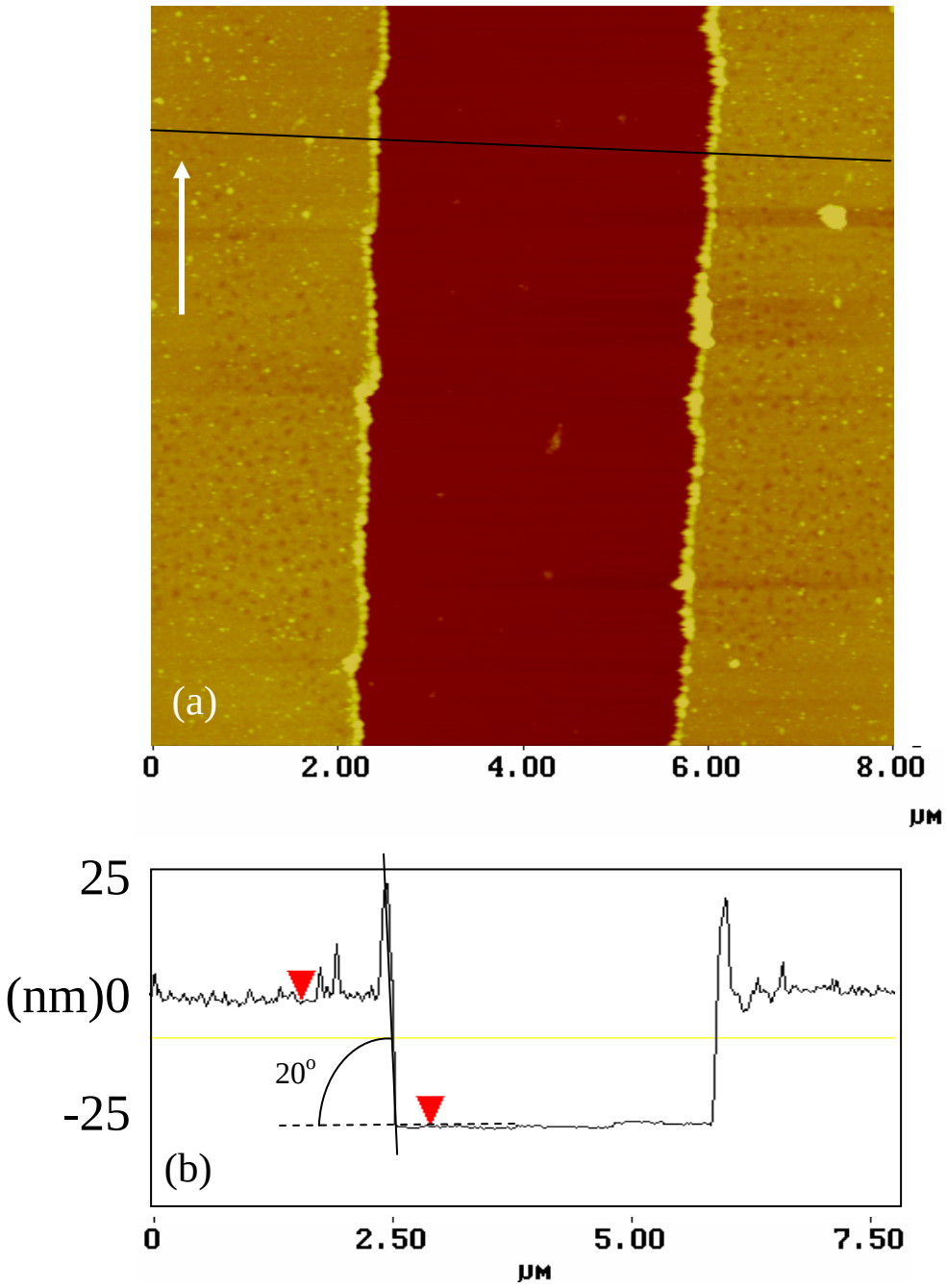

Figure 5.7 AFM images of Cu/Si wear tracks; (a) plan view, (b) cross-sectional line scan (images are from a region further along the same wear track seen in Figure 5.6). The appearance of the angle is distorted by the compressed lateral scale.

Consider now two representative sections along a wear track for Cu/G8/Si, Figure 5.8 and Figure 5.9. These plan view AFM images and line scans through the wear track illustrate

clearly that the presence of a monolayer of dendrimer molecules at the Si surface during growth of the 15 nm Cu film has dramatically altered the operative abrasive wear mechanism. The edges of the wear track are highly irregular with stop-and-start cuts, or tears, of the Cu layer evident. Substantial debris is also left behind the moving tip near the trench. Note that the roughness of the Cu film in areas away from the wear trench has been decreased by the presence of the dendrimer interlayer in agreement with previous reports[31, 33]. The bottoms of the trenches are again remarkably flat with trench depths at both locations of ~ 15 nm, consistent with the thickness of the Cu layer. The width of the wear track obviously varies significantly with position along the track. In the AFM line scans the near absence of ridges is quite striking; lateral displacement has been minimized. The mean approximate angle between the wall of the wear track and the film surface for the dendrimer mediated wear tracks is ~ 40º, i.e., about twice as steep as for Cu/Si samples. These observations are consistent with the removal of Cu film in the form of a rather jagged edged 'ribbon' by a cutting mechanism, a dramatic alteration of the abrasive wear mode caused by the presence of the dendrimer monolayer.

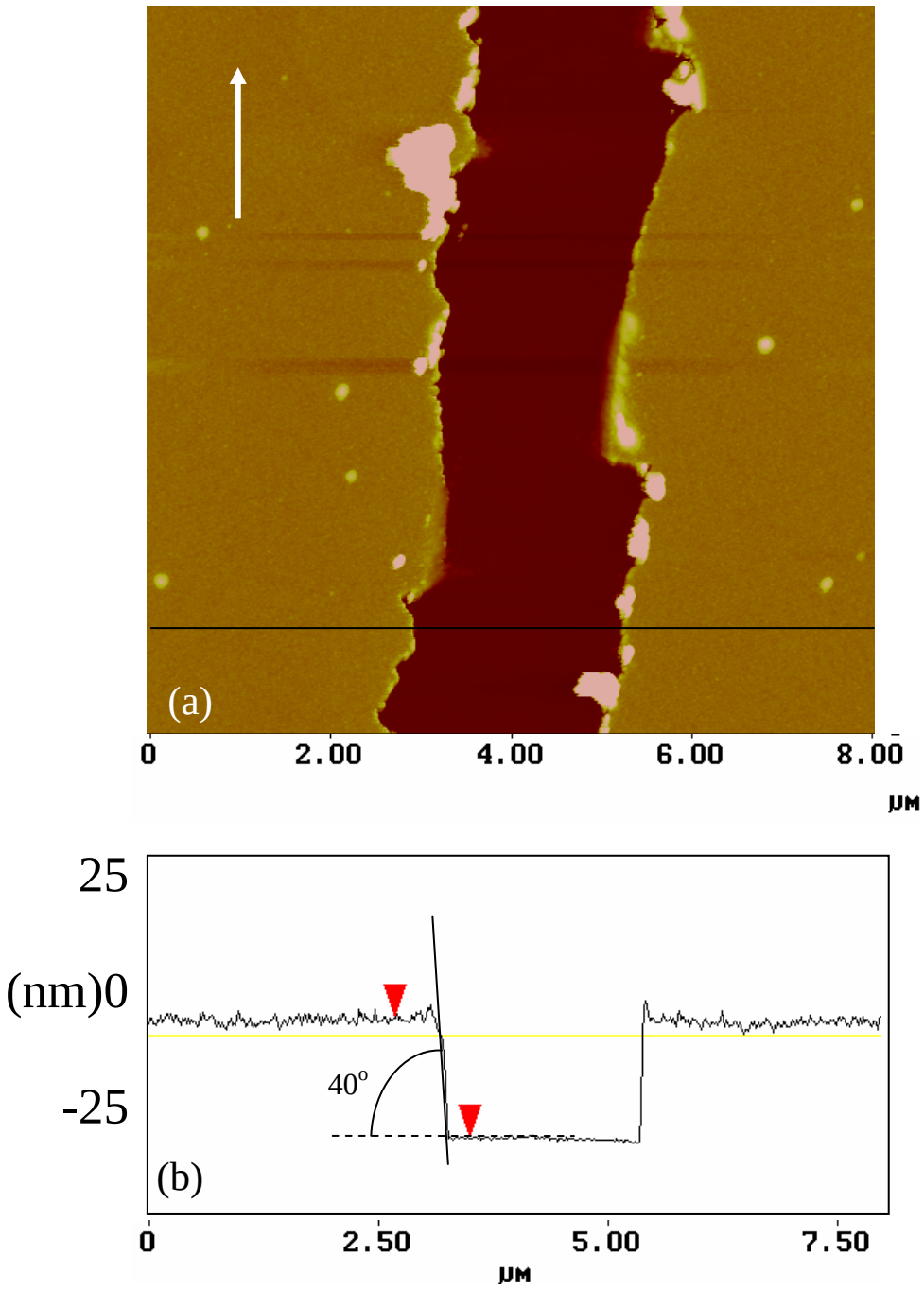

Figure 5.8 AFM images of Cu/G8/Si wear tracks; (a) plan view, (b) cross-sectional line scan.

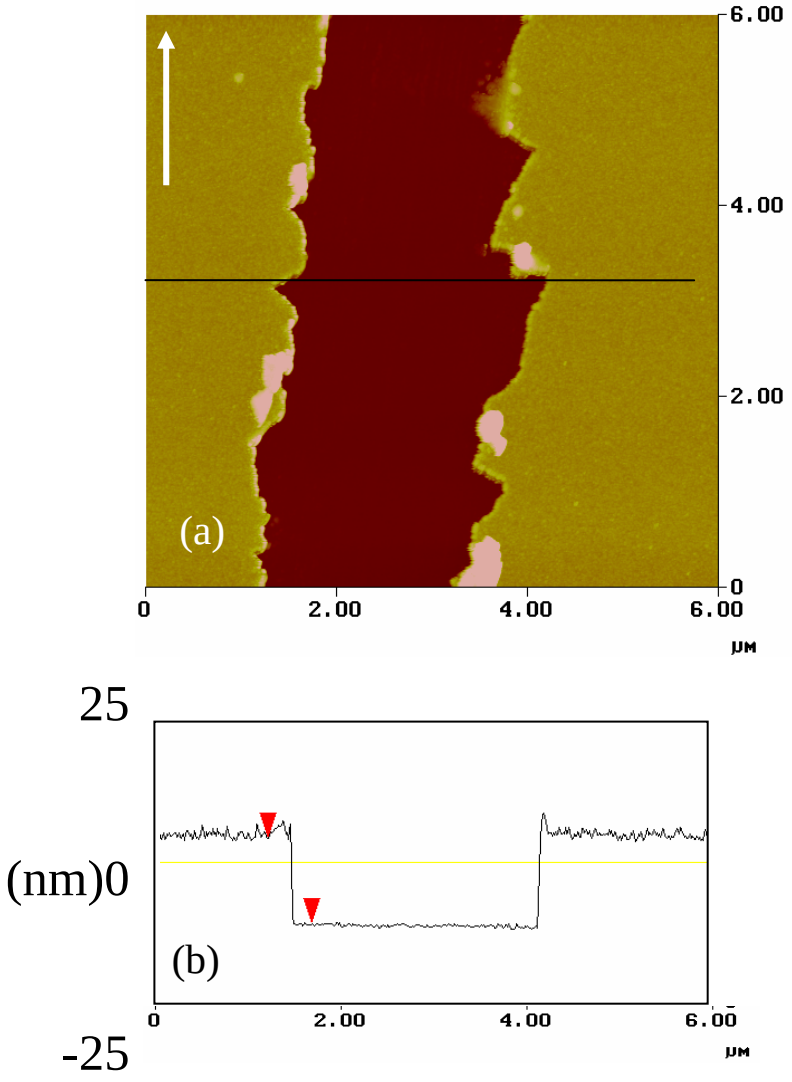

Figure 5.9 AFM images of Cu/G8/Si wear tracks; (a) plan view, (b) cross-sectional line scan (images are from a region further along the same wear track seen in Figure 5.8).

5.4 NANOSCRATCH BEHAVIOR OF CR FILMS

12 nm thick Cr films were also used to study the effect of dendrimer monolayers on the nanoscratch mechanism of thin metal overlayers. In this case the Cr is expected to chemically interact with the dendrimer molecules more readily than Cu. Unfortunately, due to an accident

with the blunted tip, a newer, and thus sharper Berkovich-shaped diamond tip aligned to scratch the surface in a face-forward direction was used for the Cr series. Thicknesses were confirmed by XRR.

SEM images of the regions containing the two sets of five scratches appear in Figure 5.10. Figure 5.10 (a) shows the nanoscratch wear tracks generated on Cr/Si while Figure 5.10 (b) shows the nanoscratches found on Cr/G8/Si. The direction of scratch is indicated with the white arrow. It is clear that the results from multiple scratch experiments are very consistent in both films. At this scale it is difficult to draw conclusions about differences between the two sets of scratches.

A clearer picture of the differences in the wear of Cr/Si versus Cr/G8/Si was provided by higher magnification SEM imaging of sections of the wear tracks. Figure 5.11 shows two SEM images of a segment of the wear tracks on the Cr/Si (Figure 5.11a) and Cr/G8/Si (Figure 5.11b) samples. The width of the scratch trench in Cr/Si sample is much larger than that of the Cr/G8/Si. In addition, the scratch trench in Cr/Si is smoother. By contrast, when Cr deposition is mediated by a dendrimer monolayer the appearance of the wear tracks is completely different. The wear track edges are not smooth, significant material debris is left along the wear track, and the pile-ups, when present, are irregular. In addition, material removal is inconsistent. The operative wear mechanism has clearly again been dramatically altered by the presence of the dendrimer monolayer.

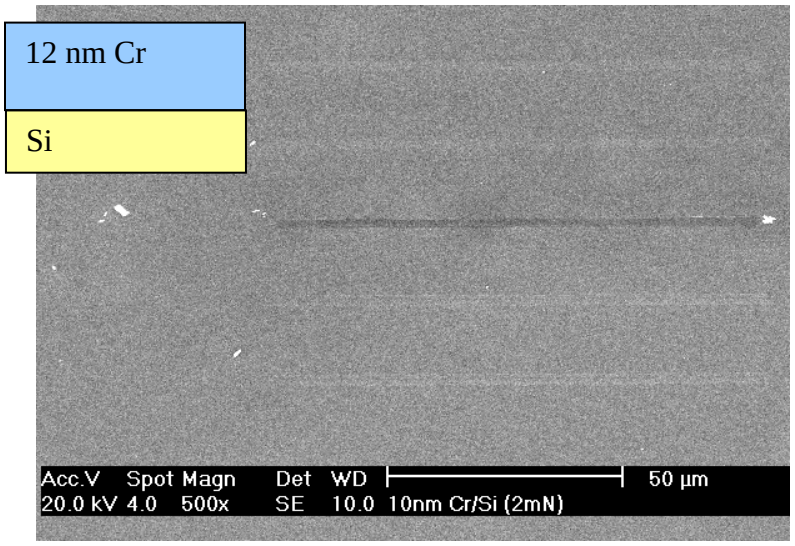

(a)

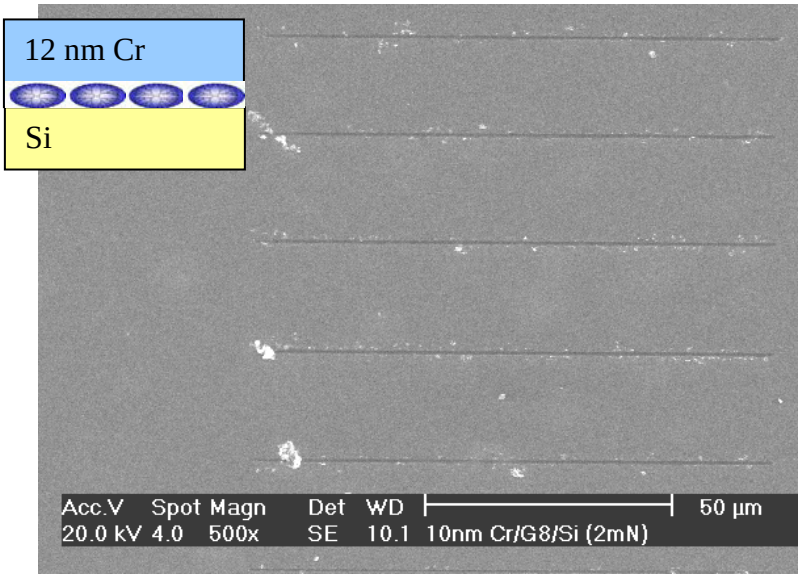

(b)

Figure 5.10 SEM images of sets of nanoscratches made using 2 mN constant loads; a) Cr/Si, b) Cr/G8/Si.

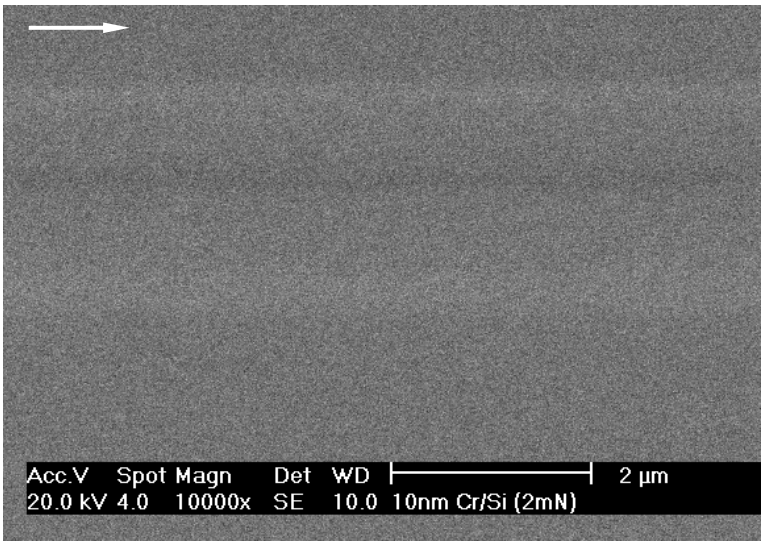

(a)

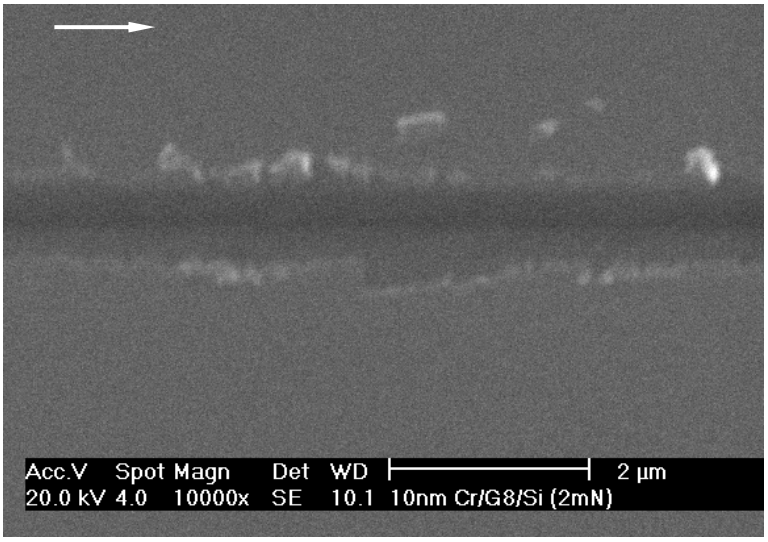

(b)

Figure 5.11 SEM images of a section of the wear tracks on a) Cr/Si and b) Cr/G8/Si.

A much clearer picture of the differences in the wear of Cr/Si versus Cr/G8/Si is provided by AFM imaging of sections of the wear tracks. Figure 5.12 (a) shows a plan view AFM image of a segment of a wear track on the Cr/Si sample. Figure 5.12 (b) is a representative AFM line

scan through the scratch, perpendicular to the scratch length. Along both edges of the wear track ridges of laterally displaced material are clearly evident confirming that some degree of plowing has occurred. The depth of the track at this point is ~ 40 nm. The width of the track at this point is ~ 2.2 μm. The approximate angle between the wall of the wear track and the film surface for the Cr/Si samples is found to be ~ 6º. The mechanism of wear and deformation for Cr/Si remains a combination of plowing and wedge formation along the length of the scratch, which is in agreement with the nanoscratch result of Cu/Si and Cu/G8/Si samples.

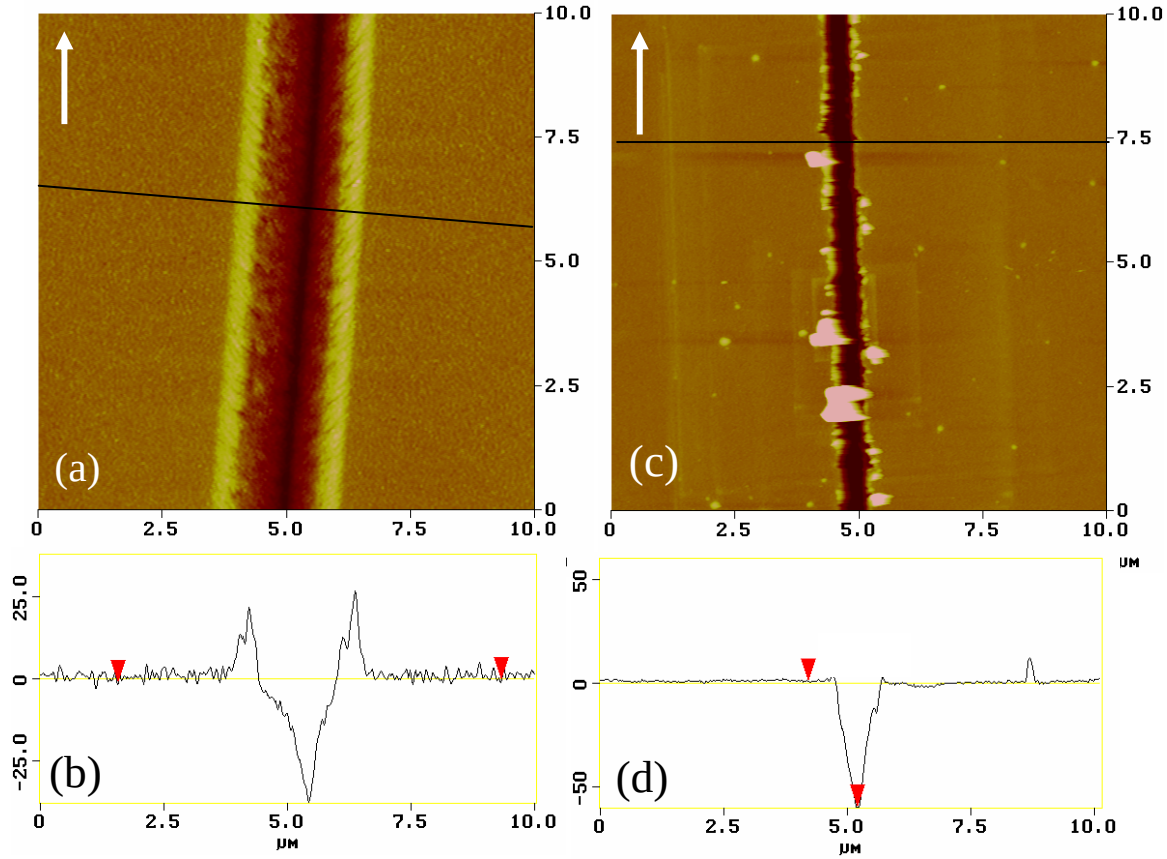

Figure 5.12 AFM images of Cr/Si wear tracks; a) plan view, b) cross-sectional line scan; and Cr/G8/Si wear tracks; c) plan view, d) cross-sectional line scan.

Consider now representative sections along a wear track for Cr/G8/Si (Figure 5.12 (c, d). These plan view AFM images and line scans through the wear track show that the presence of a monolayer of dendrimer molecules at the Si surface during growth of the 12 nm thick Cr film has dramatically altered the operative abrasive wear mechanism. The edges of the wear track are highly irregular with stop-and-start cuts, or tears, of the Cr layer evident. Substantial debris is left behind near the trench. Note that the roughness of the Cr film in areas away from the wear trench has again been decreased by the presence of the dendrimer in agreement with previous reports [9,12]. The width of the track obviously varies widely. The average width is only about 1 μm, half of that of Cr/Si sample. In the AFM line scans the near absence of ridges is quite striking. The mean approximate angle between the wall of the wear track and the film surface for the dendrimer mediated wear tracks is ~ 9º, i.e., about one and half times as steep as foı Cr/Si samples. It appears that the Cr along the wear track has been removed as a rather jagged edged ribbon by a cutting mechanism, a dramatic alteration of the abrasive wear mode caused by the presence of the dendrimer monolayer, very similar to the result in Cu films.

5.5 DISCUSSION

Simple interpretation of these results is unfortunately partially compromised by the unavoidable change in the tip geometry from blunted for Cu to sharp for Cr. The sharper tip used for the Cr experiments led to deeper wear tracks (including probable wear of the significantly more brittle Si substrate) as well as steeper-walled and narrower tracks. Nevertheless the similarity in the effects of dendrimer mediation for both Cu and Cr is quite clear. The clear change in wear mechanism observed in both Cu and Cr films when a dendrimer

monolayer is present may be explained in a variety of ways. The primary possibilities are discussed below.

5.5.1 Chemical Interaction

XPS spectra were obtained from the bare Si surface, the G8 monolayer, and from 3.5 nm of metal film deposited on the dendrimer monolayers. The 3.5 nm thickness was chosen because of the surface sensitivity of XPS – from the 'universal curve' of electron inelastic mean free path λ (IMFP) versus kinetic energy (KE, eV) [81], 95% of electrons come from within 3λ of sample thickness, which is about 2.5 - 3 nm for the N1s peak in Cu/G8 and Cr/G8 films. In order to maximize the information from the dendrimer/metal intermixed zone thinner metal films were used for this chemical analysis. Thicker layers of metal would have 'buried' the important intermixed region and made its chemistry inaccessible to XPS.

The N1s spectral region of the G8 dendrimer monolayer on Si was measured and compared to the dendrimer-mediated metal films, see Figure 5.13. In short, the dendrimer N1s consists of a main peak with a binding energy of 399.9 eV and a small shoulder with a binding energy of ~ 401.5 eV. The main peak is associated with covalently bonded nitrogen. Although nitrogen exists in three different chemical environments in the dendrimer, these states cannot be resolved. They may, however, contribute to peak broadening. Essentially the same spectral features are observed for dendrimer molecules regardless of generation. A new feature with binding energy ~ 397.2 eV is observed in the N1s spectral region corresponding to a metal nitride-like feature in 3.5 nm Cr/G8/Si sample[26]. The higher binding energy feature (around 400.0 eV) is attributed to nitrogen found in the dendrimer that does not participate in reactions with deposited Cr, indicating the presence of the adsorbed dendrimer monolayer. This peak is

not found in 3.5 nm Cu/G8/Si films, although broadening of the N1s spectrum may be associated with bonds broken inside the dendrimer after the deposition of the Cu films. Based on this relatively straightforward XPS analysis it is clear that there is a strong chemical interaction between Cr and G8 molecules, and very little interaction between Cu and G8 molecules. This observation indicates that the different wear mechanisms observed in dendrimer-free and dendrimer-mediated films are not primarily due to a chemical interaction between the metal and dendrimer.

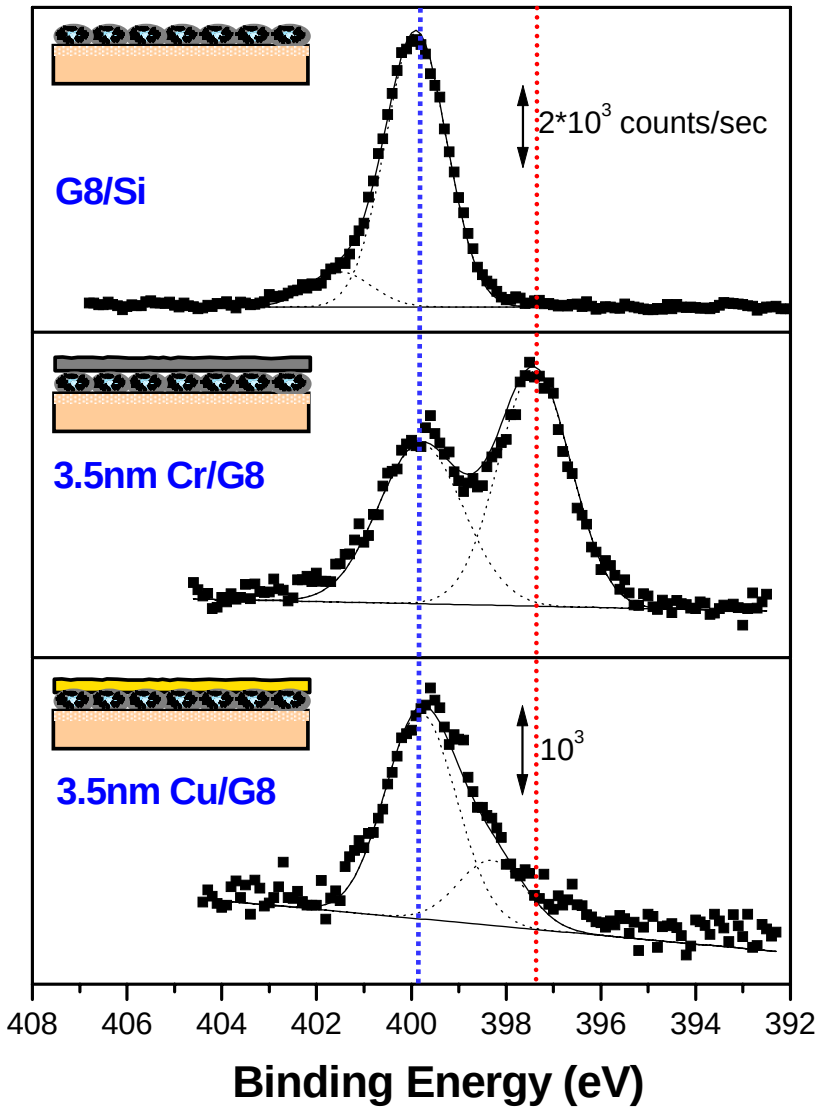

Figure 5.13 XPS spectra for the N1s region, G8 dendrimer monolayer adsorbed on Si(100) (top) and 3.5 nm of as deposited Cr (middle) and Cu (bottom) grown on a G8 dendrimer monolayer.

TEM electron diffraction was also used to evaluate the chemical interaction between metal films and the dendrimer monolayer. TEM samples were prepared on commercially available 50 nm thick silicon nitride (Si_3N_4) membrane window grids obtained from SPI (Structure Probe, Inc). In order to yield similar environments to metal films grown on dendrimer-coated and dendrimer-free Si substrates, a layer of SiO_2 (~ 2.5 nm thick) was sputter deposited on silicon nitride grids at room temperature. AFM investigations of SiO_2 films grown

on Si_3N_4 window grids showed similar topographical structures and rms roughness (data not shown). In both cases, the SiO_2 layer on the Si_3N_4 grids and Si substrate is expected to be amorphous. Each SiO_2-coated grid was cleaned and prepared using the dendrimer monolayer preparation procedures discussed earlier.

Figure 5.14 shows the bright field TEM image and corresponding diffraction pattern from 12 nm Cr/Si and Cr/G8/Si films. Both diffraction patterns indicate that the Cr has a body center cubic (BCC) crystal structure, as expected. It is found that the diameter of the (110) diffraction pattern ring of Cr/G8 is ~5% smaller than observed for Cr/Si (Figure 5.15). This is an indication that the crystal lattice of Cr has been expanded – forming a nitride or carbide like material - due to the interaction between Cr metal and the dendrimer molecules. Such differences were not observed in Cu samples (not shown here). Again, since both Cr and Cu exhibited dramatically different scratch mechanisms when a dendrimer monolayer was present, we draw the conclusion that the 'chemical' interaction between metal and dendrimer is not responsible for the distinct scratch modes observed.

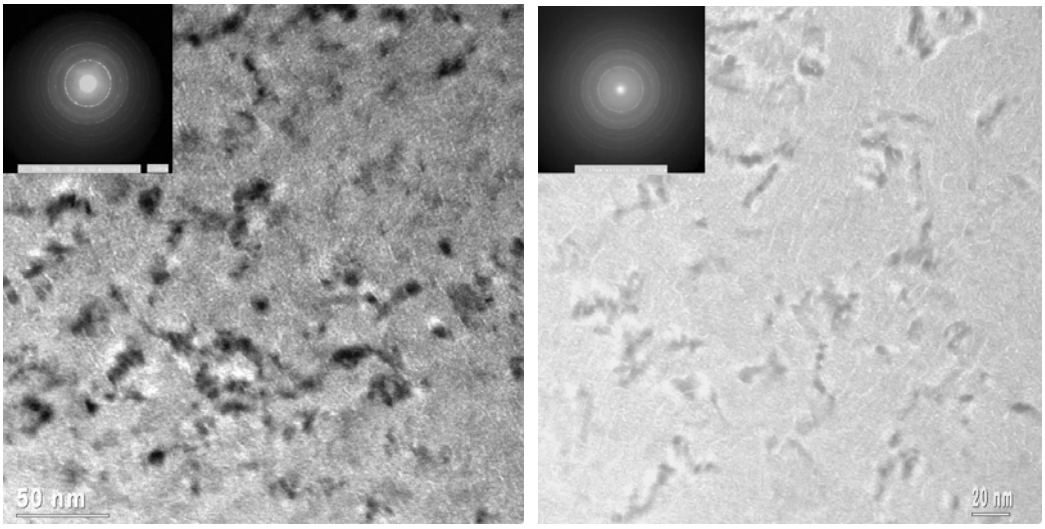

Figure 5.14 Transmission Electron Microscope (TEM) bright field image and electron diffraction pattern (inset) of 12 nm Cr/Si (L) and Cr/G8/Si (R).

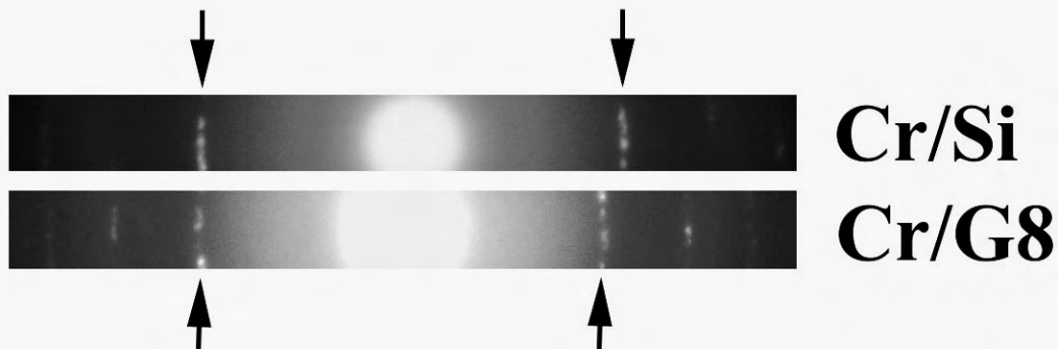

Figure 5.15 Comparison of Cr/Si and Cr/G8/Si electron diffraction.

5.5.2 Grain size effects

A second possible explanation for distinct nanomechanical properties in dendrimer mediated metal films is their grain size and/or grain size distribution. The dendrimer-free and dendrimer-mediated metal films might be expected to have different average grain sizes and grain size distributions which might contribute to the transition in the observed nanoscratch mechanism. Several models, such as the Hall-Petch relationship[82, 83], have been developed to elucidate the connection between mechanical behavior and grain size in metals and alloys.

TEM imaging experiments were carried out on Au, Cu, and Cr films with and without dendrimer interlayers. The films were deposited on Si_3N_4 TEM windows as described in the last section. The observed grain size in the Cu and Cr samples was found to be very small and the contrast between grains was poor. It thus proved very difficult to perform a reliable statistical analysis in these films. In order to gain some information on whether dendrimer-mediation produces significant changes in grain size and size distribution a study of a model film of Au was performed. The non-reactive nature of Au is likely to better represent the behavior of Cu than

Cr. Figure 5.16 shows representative TEM images of 10 nm Au/Si and 10 nm Au/G8/Si samples. Grain contrast here is sufficient to permit more detailed analysis. It appears that the grain size of Au/Si is less homogeneous than Au/G8/Si. In order to understand the grain size distribution statistically, magnified micrographs were used and a quantitative analysis was performed on two data sets pertaining to dendrimer-mediated and dendrimer-free films. For both sets, 150 data points consisting of two perpendicular diameter measurements for each dark, clearly-delineated grain were gathered. These two diameter values are averaged together and multiplied by an appropriate scale value, converting the millimeter measurements into nanometers. A simple mean and arithmetic standard deviation were calculated from both sets' averaged actual grain diameters; these values are displayed in Figure 5.17.

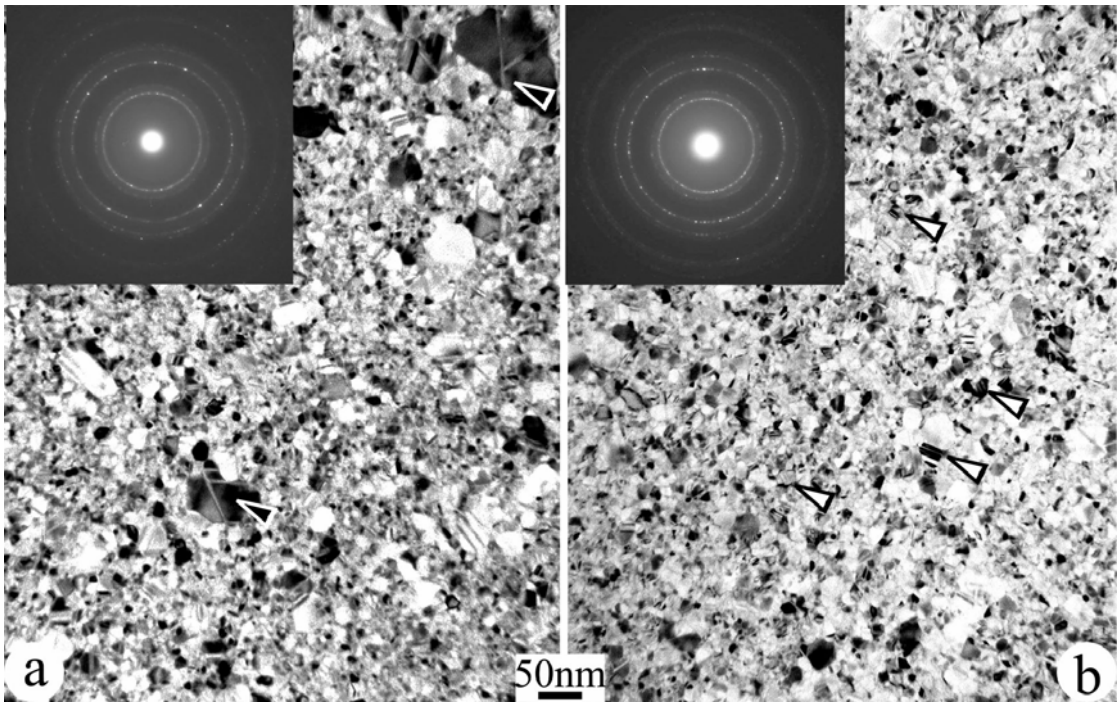

Figure 5.16 TEM bright field plan view image and electron diffraction (inset) pattern of 10 nm Au/Si (a) and 10 nm Au/G8/Si (b) deposited on Si_3N_4 TEM window.

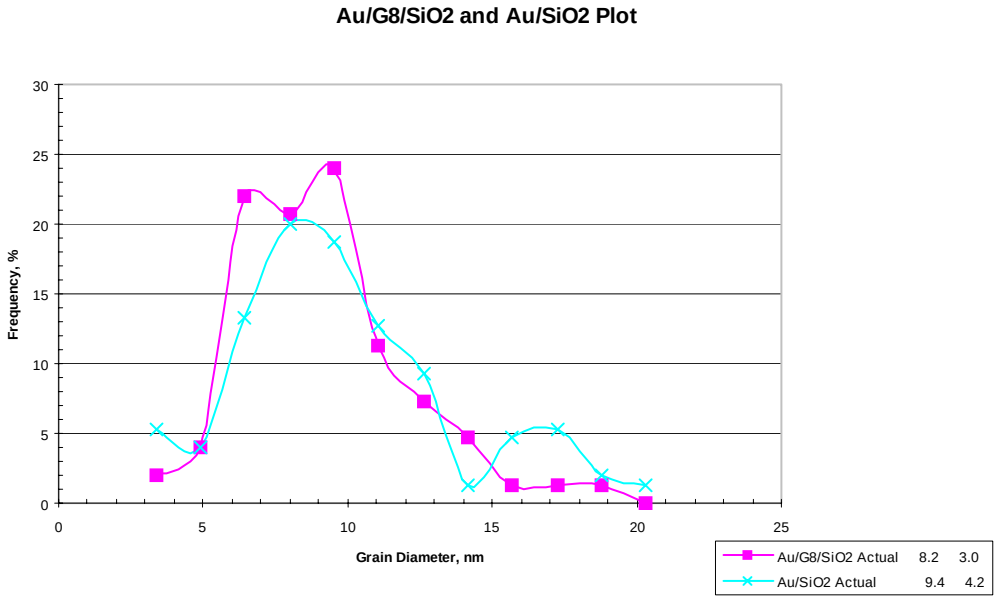

Figure 5.17 Statistical calculation and distribution of grain sizes in Au/G8/Si and Au/Si films.

Both the simple statistical information and the plot indicate that while there is some difference in the data sets extracted from the TEM micrographs of Figure 5.16, the difference is very subtle. A simple mean of 8.2 nm and a arithmetic standard deviation of 3.0 nm are calculated for the dendrimer-mediated films, while the dendrimer-free sample has slightly larger grain size, 9.4 nm, and a larger standard deviation of 4.2 nm.

Although TEM observations of analogous Cu and Cr films were of insufficient quality to permit statistical analysis, no qualitatively obvious differences were observed in the nanostructure of dendrimer-mediated and dendrimer-free films. These results, taken as a whole, indicate that the difference in nanoscratch mechanism is not likely due to grain size or grain size distribution effects.

5.5.3 Physical Intermixing

The distinct nanomechanical properties of dendrimer-mediated films might certainly be due to physical intermixing, i.e., penetration of metal into the dendrimer molecular layer forming an organic/inorganic nanocomposite material. Previous study by XPS has shown that there is penetration of both Au and Al atoms into G8 dendrimer monolayers (Figure 5.18)[34]. Penetration into adlayer molecules is expected to be more likely for chemically inert atoms[23]. Thus, if Al penetrates into the dendrimer molecule, it is assumed that Au will also do so. To confirm Au penetration inside the dendrimer molecules, three samples were prepared: G8/SiO_x, 3 nm Au/G8/SiO_x, and 2nm Al/G8/SiO_x.

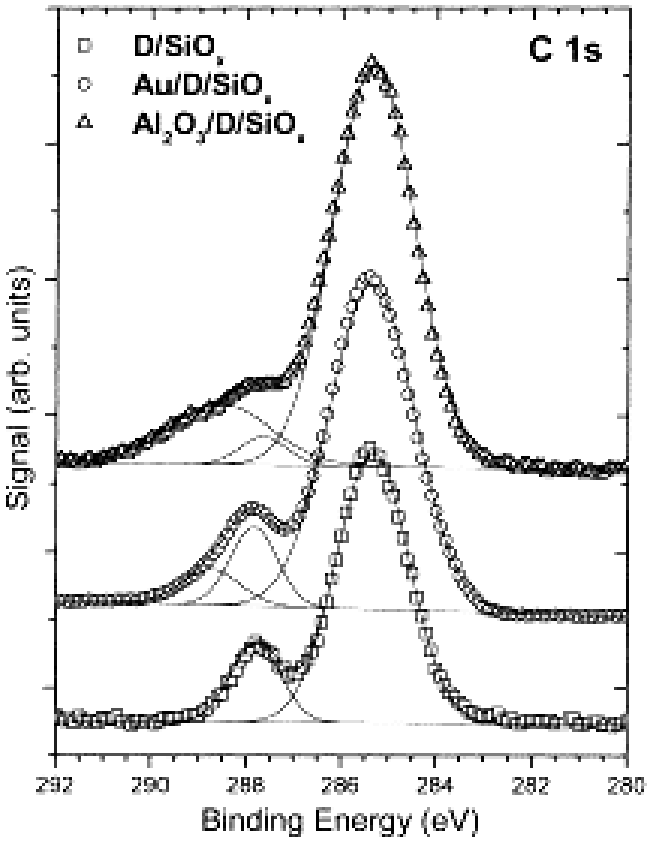

Figure 5.18 XPS C1s spectral region for dendrimer on Si with Au and Al overlayers.

XPS C1s spectra measured along the surface normal with a pass energy of 40 eV are shown in Figure 5.18. Peak deconvolution was performed with standard Kratos software using Shirley background correction and Gaussian peak shapes according to standard methods. The deconvolutions shown in Figure 5.18 illustrate these deconvolutions.

The C1s line of the G8 dendrimer consists of two well-resolved peaks with binding energies of 285.4 and 287.8 eV and FWHM 1.8 and 1.2 eV. Relative peak areas are 84 and 16% (80:20 in ideal G8). The peaks are assigned to carbon from CH_2 and C=O groups of the dendrimer, respectively. After Au and Al deposition, the main carbon peak (CH_2) shows almost no change. The minor peak becomes broader and may be deconvoluted into two peaks, indicative of metal penetration into dendrimer molecules. Metal-dendrimer interaction apparently occurs through the polar C=O group, not CH_2. This interaction is much stronger with Al than with Au, as expected. It is clear that there is some physical intermixing between metal overlayers and dendrimer molecules, which might be the reason for the different nanomechanical properties observed. However, it is still unknown how the physical intermixing occurs and whether it is possible to observe the intermixing more directly.

5.6 CHAPTER SUMMARY

In Summary, the nanoscratch behavior of ultrathin Cu films has been found to change dramatically if a dendrimer monolayer interlayer is present. This basic observation is confirmed in Cr films. In the absence of the dendrimer interlayers, distinct ridge formation along the wear track indicative of plowing and wedge formation are observed. By contrast, dendrimer monolayer-mediated films exhibit ridgeless scratches apparently formed in a nearly pure cutting

mode. Grain size effects, nanostructural uniformity, and obvious differences in chemical interactions seem to be relatively unimportant in accounting for the observed effects. The physical intermixing of metal with dendrimer molecules to form a nanocomposite with distinct properties may be at the root of these observations.

6.0 RESULTS PART 2 – DENDRIMER DOMAIN FORMATION

6.1 INTRODUCTION

Self-assembled monolayers have received increasing scientific interest in the last two decades. Perhaps the first study of self-assembled monolayers (SAMs) can be attributed to Zisman who prepared a monomolecular layer in 1946[84]. Today, they are widely studied in chemistry, physics, biology and engineering. SAMs are molecular assemblies that are formed spontaneously by contacting an appropriate substrate with an active surfactant.

There are many substrate-surfactant systems that yield organic monolayers. These include organosilanes on hydroxylated surfaces, (e.g., native oxide of silicon), alkanethiols on Au, Cu or Ag, and fatty acids on metal oxides. The ability to tailor both the head and tail group of the constituent molecules make SAMs excellent systems for many applications[27, 85]. SAMs can be used to prevent corrosion, increase lubrication, modify wetting and wear properties of solid surfaces, and generate micropatterns on a surface[86].

Dendrimer monolayers are receiving increasing attention with regard to their adhesive, frictional, and tribological behavior as well as for their potential for mediating the growth mode and quality of ultra-thin metal films[87]. By contrast, the self-organized growth of complex dendrimer patterns observed when finite volumes of dendrimer solution are cast on a substrate in a thin layer and allowed to evaporate[44] has received much less attention.

A thorough understanding of dendrimer/substrate interactions and their effect on dendrimer attachment/detachment, surface mobility, and layer growth (mode and kinetics) is lacking. However, the basic physical picture envisaged for dendrimer layer growth by immersion (dipping) of a substrate into a dendrimer containing solution is that isolated dendrimer molecules in solution randomly adsorb on the substrate surface and stick with some (unknown) probability. Dendrimer molecules progressively fill up the surface forming a more or less close-packed monolayer, although simultaneous or subsequent multilayer formation may also occur. Rinsing of dendrimer films fabricated in this way removes the more loosely bound dendrimer molecules (those not in direct contact with the substrate) leaving behind a flat and uniform monolayer. Little is known about dendrimer molecule surface diffusion, although patterned dendrimer monolayer stripes have been found to dissipate into a disordered, incomplete monolayer under ambient conditions over a period of days[47]. Dendrimer mobility enhanced by adsorption of water from the ambient has been proposed as the mechanism of the dissipation.

In this context we have explored the use of an alternative method to deliver dendrimer molecules in a controlled fashion to a substrate of interest. The objective is to develop a processing path that will yield a pattern of dendrimer domains of consistent monolayer height, with completely bare substrate separating the domains. A simple but effective aerosol deposition technique is used in this work to rapidly generate thin fluid dendrimer solution films. These thin fluid layers are found to yield complex and diverse two-dimensional patterns on drying. Using the aerosol method, there is no rinsing away of dendrimers as in the conventional immersion process. All dendrimer molecules in the solution are eventually incorporated in the resulting dried dendrimer patterns. Two dendrimer solution systems with different characteristics –

standard PAMAM G4/ethanol, and 25% C_{12} PAMAM G4/pentanol – are used to study dendrimer domain formation by aerosol spray methods (the aerosol method is described in further detail in the experimental section 3.2.2).

For the case of a thin film of evaporating dendrimer solution it is not clear to what extent the forces associated with the dewetting phenomena may influence the final dried dendrimer structure. Little is known quantitatively about dendrimer mobility at the substrate/dendrimer solution interface. Significant lateral diffusion in the presence of a solvent, if not desorption/readsorption, as well as the dewetting of the solvent during the evaporation process, are generally assumed and are necessary in accounting for many dendrimer film structures including those described in the next section.

6.2 AEROSOL SPRAY OF STANDARD G4/ETHANOL ON TO MICA SUBSTRATE – DEWETTING

6.2.1 Dewetting processes

For thin cast films containing a finite reservoir of dendrimer molecules, with dendrimer attachment to the substrate occurring during evaporation and eventual dewetting, the physical situation is quite complicated. In this case, reduction of the fluid film thickness through evaporation leads to the onset of dewetting[69-72, 88] via nucleation of holes (dry patches). Once nucleated, the holes grow and ultimately impinge to produce contact lines which form a cellular structure. The contact lines themselves may further break-up into droplets before final, complete evaporation. Two mechanisms for the nucleation of holes are considered: heterogeneous nucleation (e.g., nucleation of the dry patch at substrate defects such as airborne contamination)

and ‘spinodal’ dewetting where thermal fluctuations of a critical wavelength grow exponentially and determine a characteristic length scale (the critical wavelength).

The basic physics of the nucleation of holes in drying liquid films was investigated initially by Rayleigh and Marangoni about 100 years ago. Figure 6.1 shows a schematic of the dewetting process initiated with the nucleation and growth of the dry patches or holes in the liquid film. During the nucleation and growth process, the dewetting starts with the nucleation event – formation of a dry patch (hole) which proceeds to grow by the transport of material away from the nucleating site to a retreating rim surrounding the hole. As a hole continues to grow, it will impinge on adjacent holes eventually resulting in the formation of ‘walls’ of the fluid material along their contact line. The ‘walls’ may further break up into a series of droplets. Complete dewetting is reached when all holes have grown to impingement forming polygons composed of droplets of the fluid. The final stages of evaporation remove the remnants of the fluid network structure.

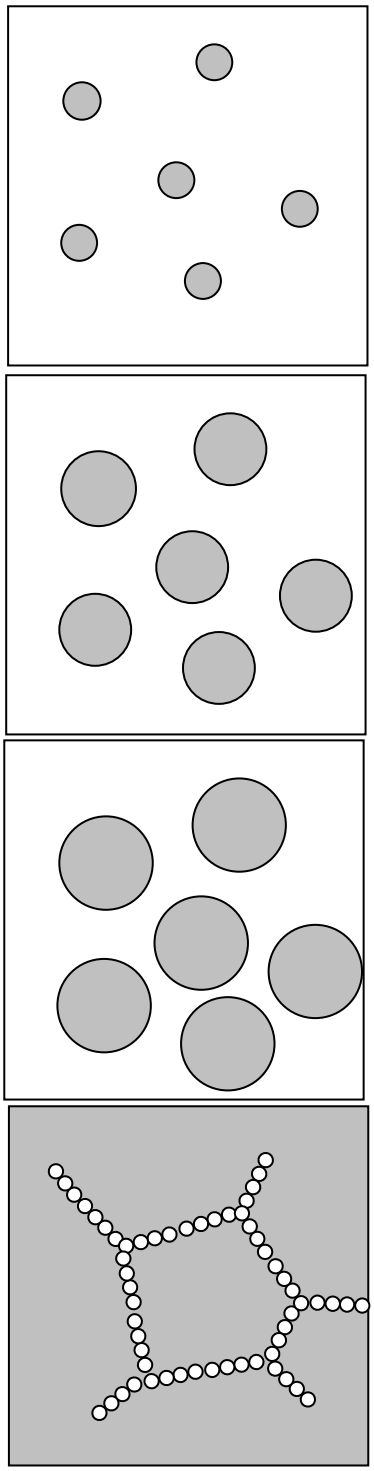

Figure 6.1 Schematics of the dewetting process of a thin liquid film. (a) nucleation of dry patches or holes in the film; (b) growth of the holes; (c) the holes impinge on each other forming a ribbon of fluid between them; and (d) complete dewetting resulting in the formation of cellular structures containing the remnants of the liquid solution.

Homogeneous dewetting (or "spinodal dewetting") has recently been clearly treated by Herminghaus et. al[72]. The term "spinodal dewetting" has been coined because of its mathematical similarity to the symmetry breaking mechanism involved in more general decomposition or phase separation processes[89, 90]. Spinodal dewetting occurs when the long-range forces across a wetting layer, such as the van der Waals forces, favor wetting. They act as the principal restoring forces stabilizing lateral film thickness fluctuations, such as those caused by thermally activated surface waves. Their amplitude is usually small relative to the film thickness, such that thermally activated nucleation of dry patches can be safely neglected. However, as the film thickness continues to decrease due to evaporation and the amplitude of the thermal fluctuations increase exponentially with time, spinodal dewetting can occur when the amplitude reaches the size of the film thickness.

If the fluid of interest has dispersed molecules (or particles) in solution which do not evaporate with the fluid, then the molecular structures left behind (their scale, arrangement, organization) after complete evaporation may be interpretable in terms of the likely dewetting processes which occurred. Clearly the strength of the molecule-substrate and molecule-molecule interactions will influence and complicate the analysis of the dry structures.

6.2.2 Results and Discussion

This section is organized in terms the structure and morphology of the dried dendrimer features as a function of increasing equivalent dendrimer layer thickness. As will become apparent, although the dendrimer structures are laterally heterogeneous, distinct layering is observed with thicknesses which correspond closely to integral multiples of the mean monolayer

(ML) thickness reported by Tsukruk for G4 PAMAM dendrimers on Si wafers by XRR (~ 1.8 nm)[36].

At the low end of the thicknesses studied (~ 0.3 nm) the dendrimers tend to be organized into dispersed, quite circular islands of varying diameters (Figure 6.2). In regions where the islands are smaller, ~ 0.5 μm diameter (Figure 6.2a), they are more uniform in size. Islands up to 1.5 μm are observed (Figure 6.2b). Many of the islands have two discrete levels: around the perimeter the height is ~ 3.4 nm while at the center the height is ~ 7.1 nm. These thicknesses correspond closely to 2 and 4 ML of G4 dendrimer, respectively. This two level structure can be seen in Figure 6.2c and more clearly in the enlarged plan and section of an individual island in Figure 6.3. The radial symmetry of these two level islands is apparent.

In the background much smaller (~ 100 nm) and less regularly shaped features are found. The height of these features is ~ 1.5 nm, roughly corresponding to 1 ML of G4 dendrimer. Particularly for the larger islands there is a significant increase in the areal density of the small features near the islands. The overall organization and morphologies of the dried dendrimer structures found here at low equivalent thicknesses do not appear to correspond well to the cellular patterns which often result from dewetting.

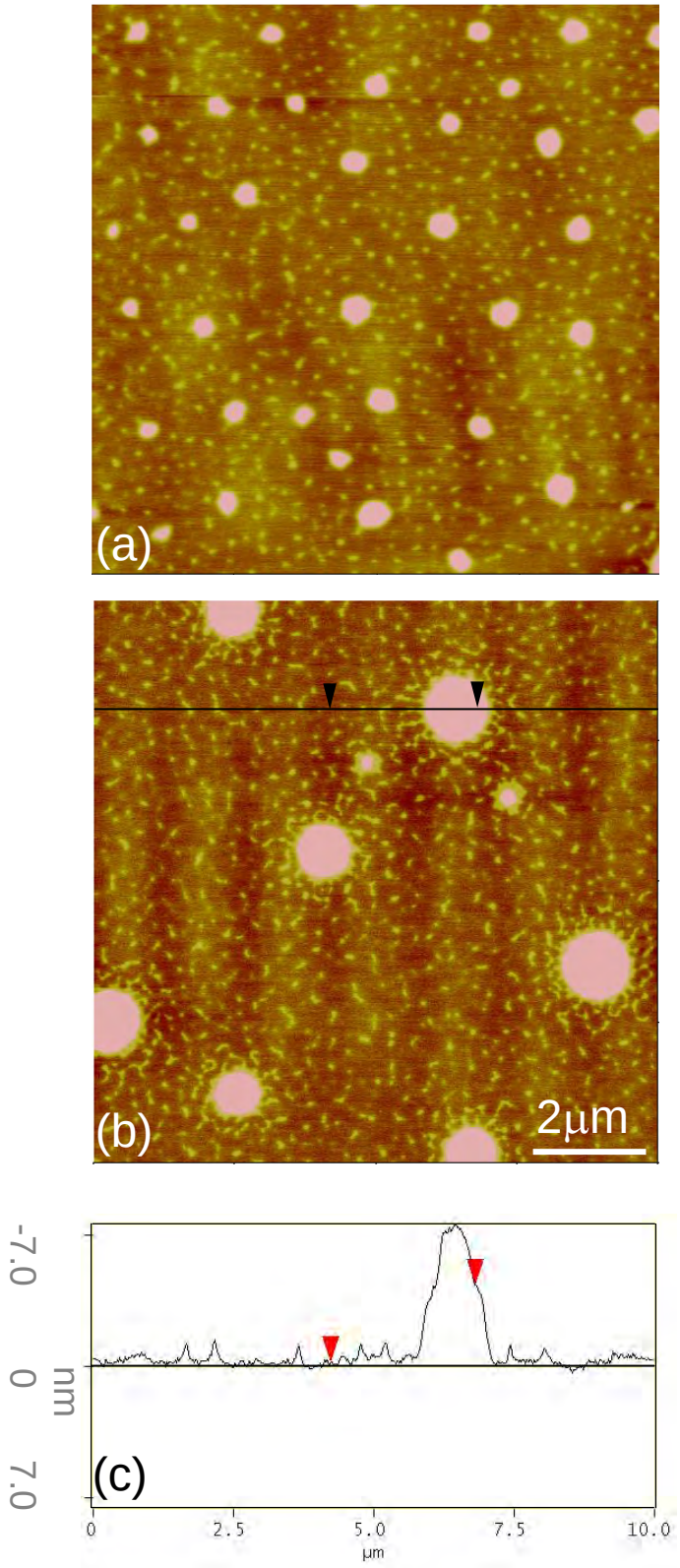

Figure 6.2 Representative plan-view AFM images and cross-section for ~ 0.3 nm equivalent thickness of G4 PAMAM dendrimer aerosol deposited on mica.

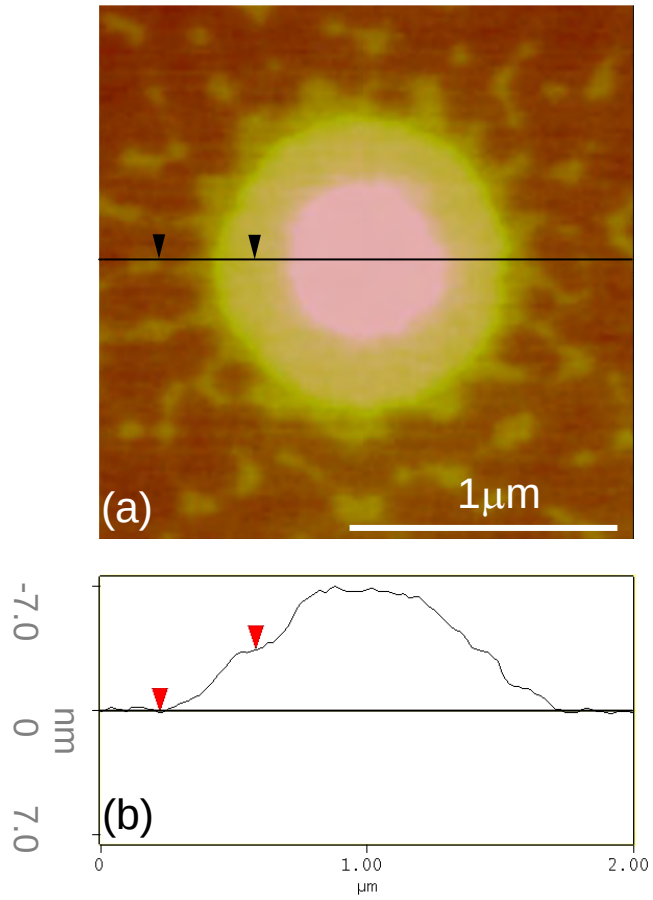

Figure 6.3 Enlarged plan-view AFM image and cross-section of a dendrimer island from Figure 6.2b

As the equivalent thickness of the dendrimer film increases to ~ 0.6 nm very different morphologies are found (Figure 6.4). A cellular substructure is now clearly observed. The irregular and discontinuous cell 'walls' are ~ 1.5 nm high. Superposed on the cellular background are regularly spaced and sized islands with essentially the same two height levels (~ 3.6 and ~ 7.0 nm) observed above at 0.3 nm equivalent thicknesses. The islands are now irregularly shaped, not circular (as found in Figure 6.4b), but the two level structure of a 4 ML central region surrounded by a 2 ML perimeter recurs and is shown in Figure 6.5.

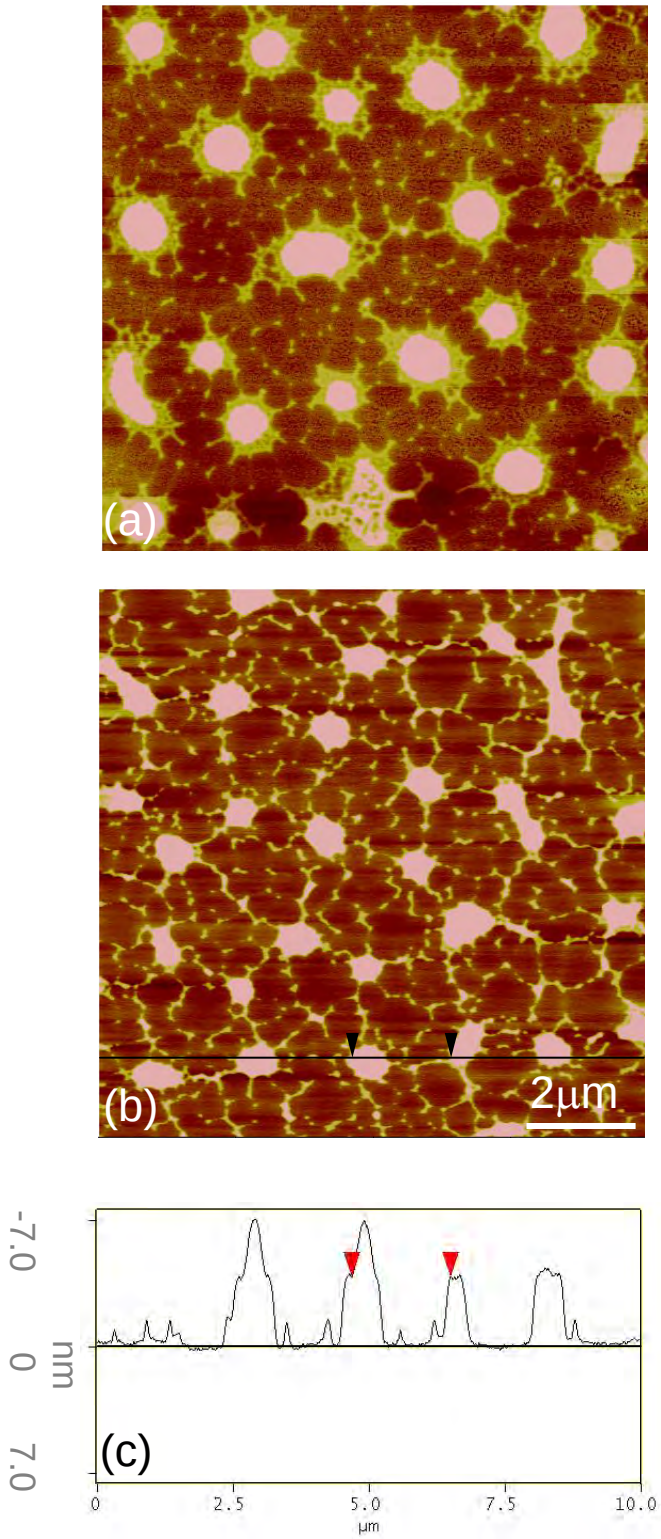

Figure 6.4 Representative plan-view AFM images and cross-section for ~ 0.6 nm equivalent thickness of G4 PAMAM dendrimer aerosol deposited on mica.

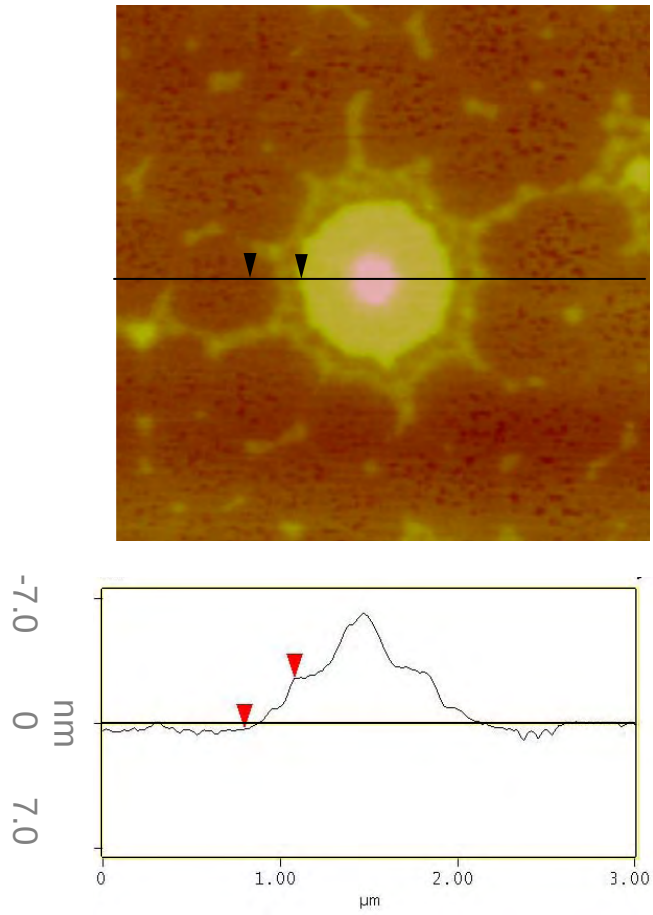

Figure 6.5 Enlarged plan-view AFM image and cross-section of a dendrimer island from Figure 6.4a.

The section shown in Figure 6.4c cuts through the center of two islands and through the edge of two adjacent islands revealing the consistent height of the perimeter region from island to island. The patterns observed in Figure 6.4 are explainable in terms of dewetting phenomena. A logical scenario is that dendrimer molecules initially accumulate in cell walls (the 'contact lines' generated during evaporation). The cell walls then serve to 'feed' nearly uniformly spaced junction points with dendrimer molecules. These junction points eventually evolve into the observed pattern of islands. Two in-plane correlation lengths deduced from power density spectrum analysis (see Figure 6.6) are apparent in Figure 6.4a and b. The power spectral density,

PSD, describes how the power (or variance) of a time series is distributed with frequency. Mathematically, it is defined as the Fourier Transform91 of the autocorrelation sequence of the time series. An equivalent definition of PSD is the squared modulus of the Fourier transform of the time series (or length), scaled by a proper constant term.

The typical AFM scan of a surface might appear to exhibit "random" features. The PSD function can reveal its periodic characteristics and provides a graphical representation of how such features are distributed. The 2D isotropic PSD is used in analyzing our AFM measurements. This is a two dimensional power spectral density. Its units are length squared divided by a two dimensional frequency, or 1 over length squared. The isotropic means that it is an average taken over all directions in the data.

A representative 2D isotropic PSD analysis of a G4 PAMAM dendrimer aerosol deposited onto mica is shown in Figure 6.6 analyzed from Figure 6.4b. There is a spike in the middle of the PSD spectrum which corresponds to the periodic wavelength of the main surface features (dendrimer islands). It is also interesting to note that there is a shoulder to the curve in the lower wavelength region. This shoulder corresponds to the periodicity of the 'cellular' or 'network' substructure revealed by the thin interconnected 'walls' of dendrimer molecules. For this case one extracts a mean spacing of islands of 1.7 μm and a mean cell to cell distance of 0.28 μm. These two lengths are superposed on the figure as solid bars whose length is drawn to scale.

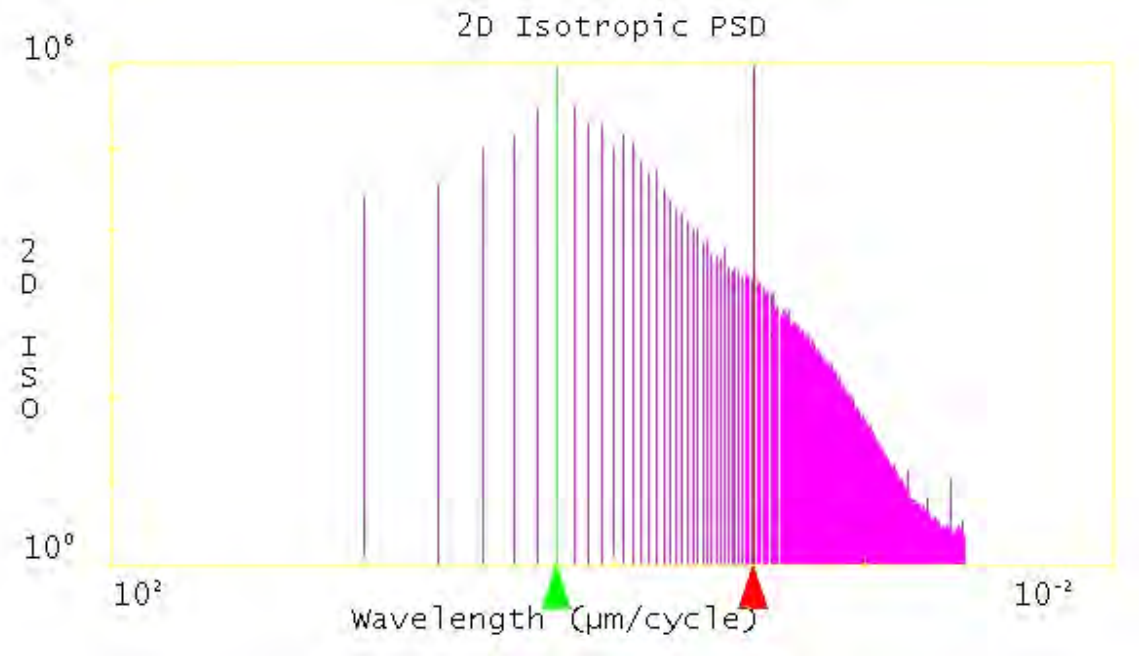

(b)

Figure 6.6 A 2D Isotropic PSD analysis of Figure 6.4b. The main wavelength (green line) corresponds to 1.7 µm and secondary wavelength (red line) corresponds to 0.28µm.

In Figure 6.4b, the shorter correlation length is ~ 0.3 µm and corresponds well to the cell spacing and the longer one is ~ 2 µm which clearly correlates to the island spacing. If dewetting is in fact the operative physical process producing the final dried structure then the cell spacing can be said to determine the island spacing. However, the physical original of the cell spacing itself is not apparent. No obvious external defects were detected by AFM imaging and the mica surfaces are pristine. The absence of dendrimers on the mica surface within the cells indicates that the forces associated with the receding fluid contact during evaporation are able to strip away dendrimer molecules adsorbed in the early stages of deposition when the entire surface is submerged. It may be that the original source of the heterogeneous nucleation, perhaps very small airborne particles, are also stripped away by the receding fluid leaving no evidence behind.

On occasion a very different morphology is observed at ~ 0.6 nm equivalent thickness. Figure 6.7 illustrates the 'undulative' mode commonly associated with spinodal dewetting. In this case the height of the 'wormlike' dried dendrimer structures is ~ 1.8 nm (1 ML) and the critical wavelength is ~ 0.5 μm. This topography is very distinct from all the others observed in this study in its overall pattern which is inconsistent with heterogeneous nucleation of holes or dry patches. Similar spinodal structures have been reported for dewetting of carbosilane dendrimer[44] and liquid crystal films.

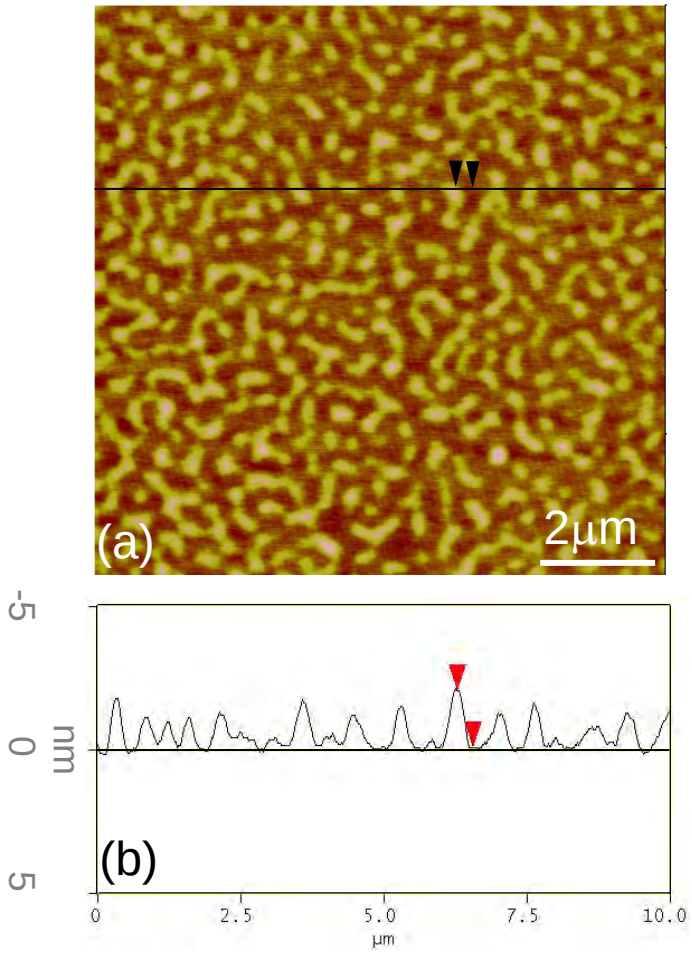

Figure 6.7 Representative plan-view AFM image and cross-section for ~ 0.6 nm equivalent thickness of G4 PAMAM dendrimer aerosol deposited on mica illustrating the spinodal topography.

As the amount of dendrimer reaches equivalent thicknesses of 1 nm and above a complex contiguous morphology emerges (Figure 6.8). The dendrimer layer is now a fully interconnected network penetrated by irregularly shaped large holes which themselves contain small dendrimer islands. Figure 6.8a is a representative structure observed at a thickness of ~ 1 nm while Figure 6.8b corresponds to ~ 1.4 nm. As more dendrimer is incorporated the size of the holes decreases along with the number of islands per hole. In Figure 6.8c the extremely consistent height of the contiguous dendrimer network from place to place is apparent and averages ~ 3.5 nm (again, ~ 2 ML). This molecular layer is also extremely flat. The section in Figure 6.8c was selected to avoid holes over a significant distance. The rms roughness along the line between the two triangular markers is ~ 0.1 nm, only slightly rougher than the bare mica substrate itself. The height of the small islands is less regular but consistently lower than the percolated network, typically ranging from 1.5 to 2.0 nm (~ 1 ML).

The structures in Figure 6.8 are also qualitatively consistent with dewetting. The narrow, discontinuous cell walls of Figure 6.3 have been replaced by a fully interconnected 2 ML thick dendrimer film network with cross-sectional widths between holes as large as 2 μm. The islands remaining inside the holes may be associated with the adsorption process prior to nucleation of dry patches. In this case these island structures were apparently stable against the receding contact line during evaporation.

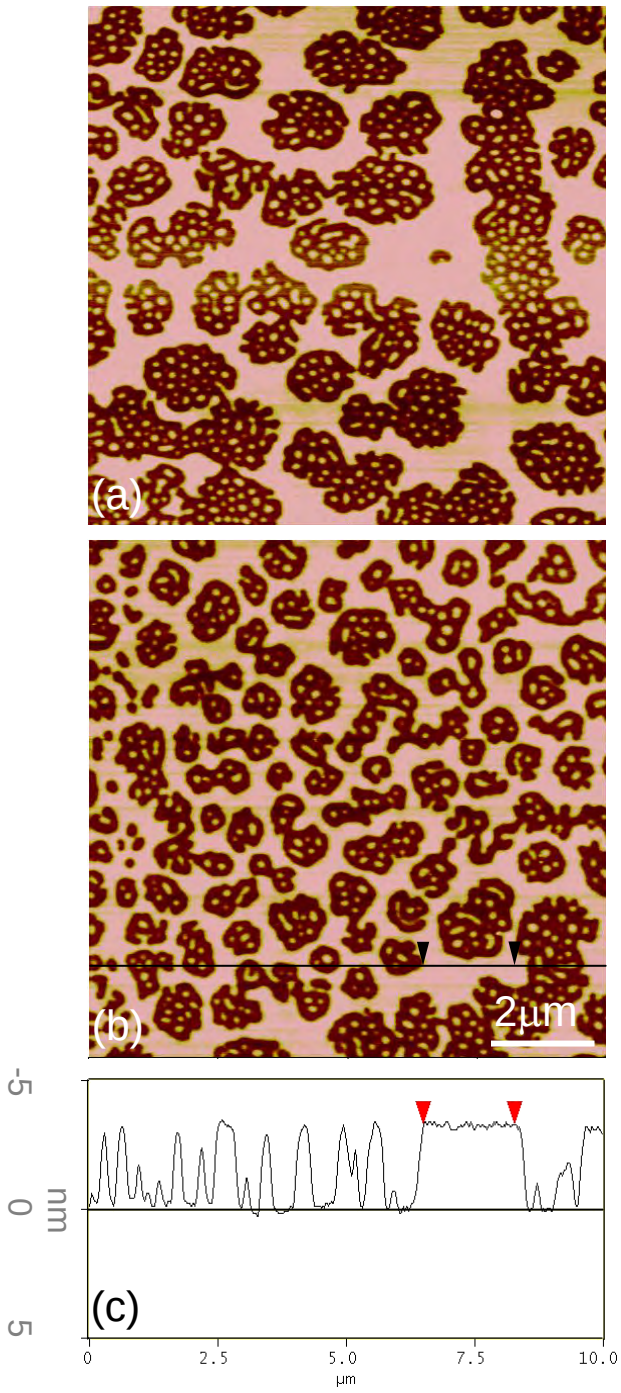

Figure 6.8 Representative plan-view AFM images and cross-section for (a) ~ 1.0 nm and (b) ~ 1.4 nm equivalent thickness of G4 PAMAM dendrimer aerosol deposited on mica.

As the equivalent dendrimer thicknesses approach and exceed the G4 monolayer thickness, film morphologies continue to evolve (Figure 6.9). Figure 6.9a is representative of an equivalent thickness of ~ 1.6 nm. A contiguous dendrimer film is observed with ~ 0.2 μm diameter circular holes distributed over the surface. The holes penetrate to the mica substrate. In Figure 6.9b at an even higher equivalent thickness (~ 2.1 nm) the number density of holes is lower and they are slightly larger. A dispersion of much smaller holes which do not penetrate all the way through to the substrate is also observed. The thickness of the molecular layer in this nearly continuous film is ~ 3.0 nm (Figure 6.9c). This thickness is not as large as observed for the less condensed structures discussed above but is still within the range of expected values for 2 ML of G4 dendrimer. Although a cellular substructure is no longer obvious the dendrimer structures observed at high equivalent thicknesses still remain consistent with dewetting via heterogeneous nucleation of dry patches.

The prevalence of 2 ML (and, on occasion, 4 ML) thick stable G4 dendrimer film patterns as observed in this study is unexpected. Controlled multilayer deposition of dendrimers is well known, but it is a product of intentionally tailored electrostatic interactions between positively charged dendrimers and negatively charged polyanhidrides[30], polyoxometalates[92,93], poly(styrene-sulfonate)[94], enzymes[95], and PAMAM dendrimers of generation [X-1/2][28]. No such electrostatic interaction of this form is expected to exist for G4 PAMAM dendrimers assembling on mica substrates. Dendrimer films of irregular thickness composed of multiple layers do form by accretion during growth using the immersion/adsorption process but there is no known preference for bilayer systems and molecules above the first layer are readily rinsed away. The patterns fabricated here are stable against exposure to both ambient air and immersion in water. We propose that the forces of dewetting tend to strip away dispersed dendrimer molecules from

the mica surface and compact them into apparently more stable and adherent bilayer films. The widespread occurrence of a second level of growth at 4 ML for low equivalent thickness samples (not 3 ML or 5 ML) remains puzzling.

To summarize, aerosol deposition of dilute dendrimer ethanolic solutions onto mica substrates has been used to fabricate a sequence of two-dimensional dried G4 PAMAM dendrimer film patterns with structures and morphologies very different from those observed for standard dipping/rinsing procedures. The processes of rapid evaporation followed by dewetting via heterogeneous nucleation of dry patches appear to determine most of the complex film structures observed, except at low equivalent layer thicknesses. Spinodal topographies have also been noted in a narrow range of equivalent thicknesses. A clear transition from dispersed dendrimer islands, to cellular structures with a superposed island pattern, to contiguous dendrimer network films has been documented as a function of increasing equivalent dendrimer layer thickness. Under these processing conditions there is a strong tendency for G4 dendrimers to organize themselves into 2 ML thick structures (sometimes with a partial second level at 4 ML). This may be associated with the enhanced stability/adhesion of 2 ML structures against the forces of dewetting which may tend to ‘strip’ dispersed dendrimer molecules from the mica surface. Logical extensions to this work include experiments to determine the effect of evaporation rate, dendrimer molecule termination chemistry, and substrate material on dendrimer domain formation, structure, morphology, and stability.

In the context of this dissertation, the G4/ethanol dried dendrimer structures observed in this section are clearly not ideally suited to serve as substrates for subsequent deposition of metal overlayers. They do not consist of single monolayer height domains cleanly separated by bare substrate and thus are not appropriate for the planned physical intermixing studies.

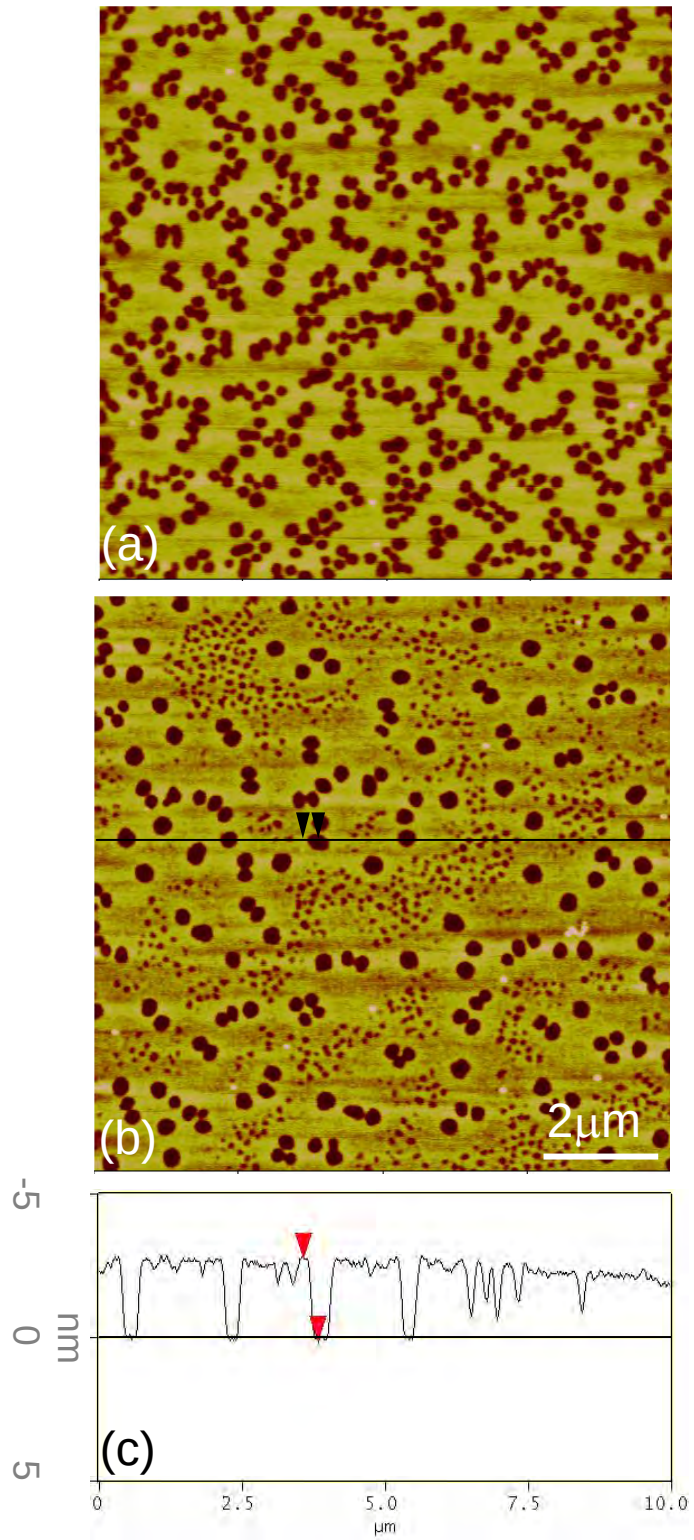

Figure 6.9 Representative plan-view AFM images and cross-section for (a) ~ 1.6 nm and (b) ~ 2.1 nm equivalent thickness of G4 PAMAM dendrimer aerosol deposited on mica.

6.3 AEROSOL SPRAY OF 25% C_{12} PAMAM G4/PENTANOL ON TO MICA SUBSTRATE – COMPETING INTERACTIONS

In the G4/ethanol system used above, the evaporation rate of ethanol is very fast because of its high vapor pressure (7.9 *kPa* at 25 ^{o}C) and the standard G4 dendrimer is expected to have only a modest adhesive interaction with the mica substrate. Not surprisingly, the dewetting mechanism dominated dendrimer domain formation in these conditions. In this section, a much slower evaporating solvent – pentanol (vapor pressure: 0.33 *kPa* at 25 ^{o}C) is used. The dewetting forces which tend to 'strip' molecules from the substrate are expected to decrease due to the slower evaporation. In addition, a 0.05 weight percent (wt.%) pentanolic solution of 25%C_{12} PAMAM G4 dendrimers obtained as a 10 wt.% methanolic solution from Aldrich (Milwaukee, WI) has been selected to replace the G4/ethanol system as the source for the self assembly of dried dendrimer molecule structures.

In 25%C_{12} PAMAM G4 dendrimer molecules there are 48 primary amino surface groups and 16 [N-(2-hydroxydodecyl)] surface groups, with theoretical molecular weight 20,113 amu. This modified G4 PAMAM dendrimer has not, to our knowledge, been studied in the open literature. It was selected because the N-(2-hydroxydodecyl) chains which replace 25% of the terminal amine groups found in a standard G4 PAMAM dendrimer were expected to enhance the dendrimer molecule/substrate interaction leading to stronger adhesion while hopefully maintaining sufficient surface mobility to allow the system to approach equilibrium. The dewetting mechanism is clearly dominant in forming dendrimer patterns in the rapidly evaporating ethanol and standard G4 PAMAM solutions, while in slower evaporating pentanol solutions containing 25%C_{12} PAMAM G4 molecules with stronger molecule/substrate interactions, a totally different domain formation mechanism may be observed.

Dendrimer film structures are again prepared by aerosol deposition using an EFFA® Spray Mounter MK II (Ernest F. Fullam, Inc.). Droplets coalesced on arrival at the substrate forming a continuous fluid film. The average droplet diameter is at least an order of magnitude larger than the dendrimer domain sizes and spacings observed by AFM of the subsequently dried adsorbed dendrimer patterns, convincing evidence that the droplets are not determining pattern formation which extend over hundreds of μm. Dynamic light scattering has been used to determine a hydrodynamic diameter of ~10.7 nm for 25%C_{12} PAMAM G4 as received in 10% w.t. methanolic solution. Based on the general tendencies noted in table 2.1, a 25%C_{12} PAMAM G4 monolayer (ML) adsorbed on a substrate would be expected to have a height of 4 – 5 nm, a little less than half of the diameter in solution. The pentanolic solutions were prepared by simple volumetric dilution using pipettes with disposable tips from fresh commercial methanol-based solutions.

The extremely uniform thickness (1 ML) and flatness of the dendrimer film structures discussed below are consistent with dendrimers dispersed at the molecular level both in the aerosol droplet and following coalescence on the substrate, and not agglomerated into various sized assemblies prior to deposition. The total volume of fluid used and the substrate area coated yielded a continuous fluid film ~ 15 μm thick (neglecting evaporation in flight) on a substrate of freshly cleaved mica. The pentanolic fluid film evaporated slowly (~10 minutes). Evaporation does cause observable 'pooling' of fluid ahead of growing dry patches leading to variations in the size of the 'local' reservoir of dendrimer molecules available to form film structures. This accounts for the variation observed in film structure at the scale of hundreds of μm. The dried dendrimer surface structures were characterized by atomic force microscopy (AFM) in 'tapping mode' with a standard tip (Digital Instruments, Inc., model D-3100). Freshly cleaved bare mica

surfaces exhibit rms roughness of 0.085 nm, while the roughness at the free surface of the 25%C_{12} PAMAM G4 dendrimer domains is just slightly higher, 0.124 nm. All images shown are representative of regions extending several hundred microns or more. The patterns shown are stable under ambient conditions over many weeks.

6.3.1 Competing interaction background

The dendrimer domain patterns observed in this series of experiments are found to correspond well with the prediction of a rather general theory of competing interactions in self-assembling materials systems. The background to this theory will be presented before discussing the experimental results for 25%C_{12} PAMAM G4 on mica.

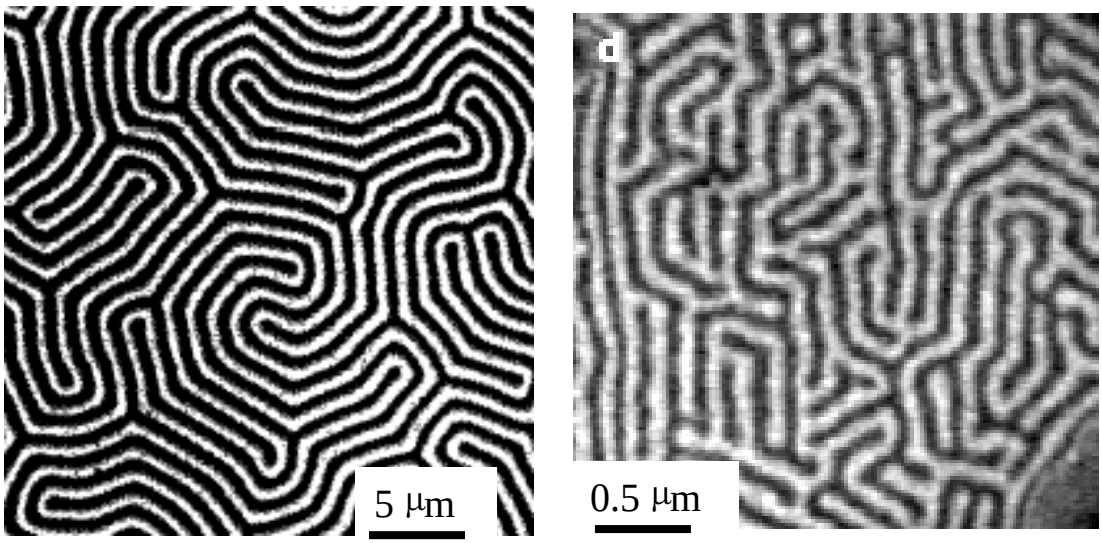

Figure 6.10 Different long-range repulsive interactions (magnetic interactions, left, and elastic interactions, right) yield similar domain patterns.

The formation of stable, two-dimensional (2D), two-phase domain patterns resulting from competing short-range attractive and long-range repulsive interactions has been explored theoretically[96-100] and observed experimentally[101-108] in a number of quite different materials

systems. The long-range repulsive interactions could be magnetic, e.g., transparent films of magnetic garnet of composition $(YGdTm)_3(FeGa)_6O_{12}$ grown on single-crystal substrates of gadolinium gallium garnet (GGG) of (111) orientation[101], shown in the left image of Figure 6.10. They could also could be elastic (surface stress) in origin, e.g., the right image of Figure 6.10 shows 2D stripes of Pb and Pb/Cu surface alloy obtained by vapor deposition of Pb on the clean Cu (111) surface at room temperature and above[108]. The short-range attractive interaction is always associated with minimization of interphase boundary length while the long-range repulsive interaction is attributed, as we have seen, to electrostatic, magnetic, elastic, etc., interactions, depending on the physics of the system. For systems with domain sizes much larger than the domain boundary width, the characteristic domain length scale, l_0, at thermodynamic equilibrium is given by[99]

$$l_0 = \pi a \exp(\gamma_b/\gamma_d + 1) \qquad (6.1)$$

where γ_b is an energy per unit length of interphase boundary, γ_d is proportional to the square of the difference in the 'dipole density' between the two phases, and a is a length quantifying the sharpness of the interphase interface. In the simplest cases γ_b can be assumed to be isotropic. The appropriate 'dipole density' in each phase depends on the physical situation (the screened electric dipole density normal to the water/air interface is used for Langmuir layers while surface stress is invoked for overlayer structures on surface alloys). The opportunity to control l_0 and thus pattern formation at the nanoscale over large areas by controlling the γ_b/γ_d ratio has exciting technological implications.

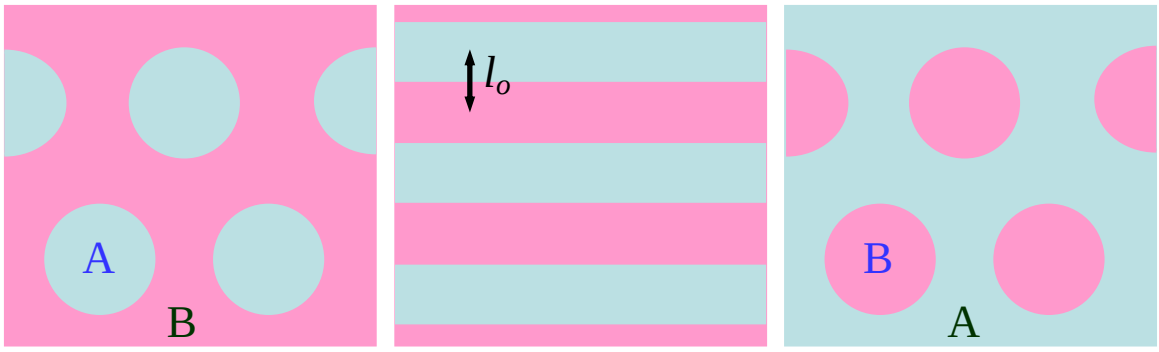

Figure 6.11 The evolution of domain patterns as a function of area fraction, f, should follow the sequence: circular islands of A in a matrix of B (the droplet phase) → alternating elongated domains of A and B (the striped phase) → circular islands of B in a matrix of A (the inverted droplet phase).

For a two-phase system of A and B, and competing interactions as described above, the evolution of domain patterns as a function of the area fraction, $f = f_A = 1 - f_B$, has been predicted[4] to follow the sequence (Figure 6.11): circular islands of A in a matrix of B (the droplet phase), alternating elongated domains of A and B (the striped phase), and circular islands of B in a matrix of A (the inverted droplet phase). The degree of long range order and the uniformity of domain sizes and shapes actually observed depend on both the thermal noise present and the proximity to equilibrium. This very basic prediction of pattern evolution has only very recently been experimentally confirmed[108] for the first time for incommensurate Pb overlayers grown on a Pb/Cu surface alloy prepared under ultrahigh vacuum conditions and imaged by low-energy electron microscopy. Surface stress differences between the overlayer and alloy structures are the origin of γ_d in this case. In the following we demonstrate that the predicted domain pattern evolution is also found in a completely different materials system consisting of dendrimer molecules adsorbed onto the surface of freshly cleaved mica. In this case the domain patterns are fabricated by simple aerosol deposition of dilute solutions of dendrimer molecules in pentanol under ambient conditions followed by slow evaporation. γ_d is proposed to be

electrostatic in origin in this case and is associated with the contact potential between the negatively charged surface of mica submerged in pentanol and the positively charged surface of the dendrimer molecule domains.

6.3.2 Results and Discussion

This section discusses systematically the evolution of dendrimer domain structure and morphology as a function of area fraction (or 'coverage') of the mica substrate covered by dendrimer molecules, *f*. As will become apparent, all of the dendrimer domains have essentially the same thickness (~ 4.7 nm) independent of *f* which corresponds well to the 1 ML thickness expected for 25%C_{12} PAMAM G4. The structures discussed below are purely 2D with no evidence for formation of a partial second or subsequent dendrimer layer as observed and described above in the ethanol/G4 system. Under these conditions this is an experimental realization of a 2D, two-phase system with the 1 ML thick dendrimer domains and the bare mica serving as the two phases. The dark contrast in all the images is the mica substrate. For clarity, all images shown are 5 μm x 5 μm but the quantitative image analysis reported is based on a 10 μm x 10 μm region which encompasses the displayed area.

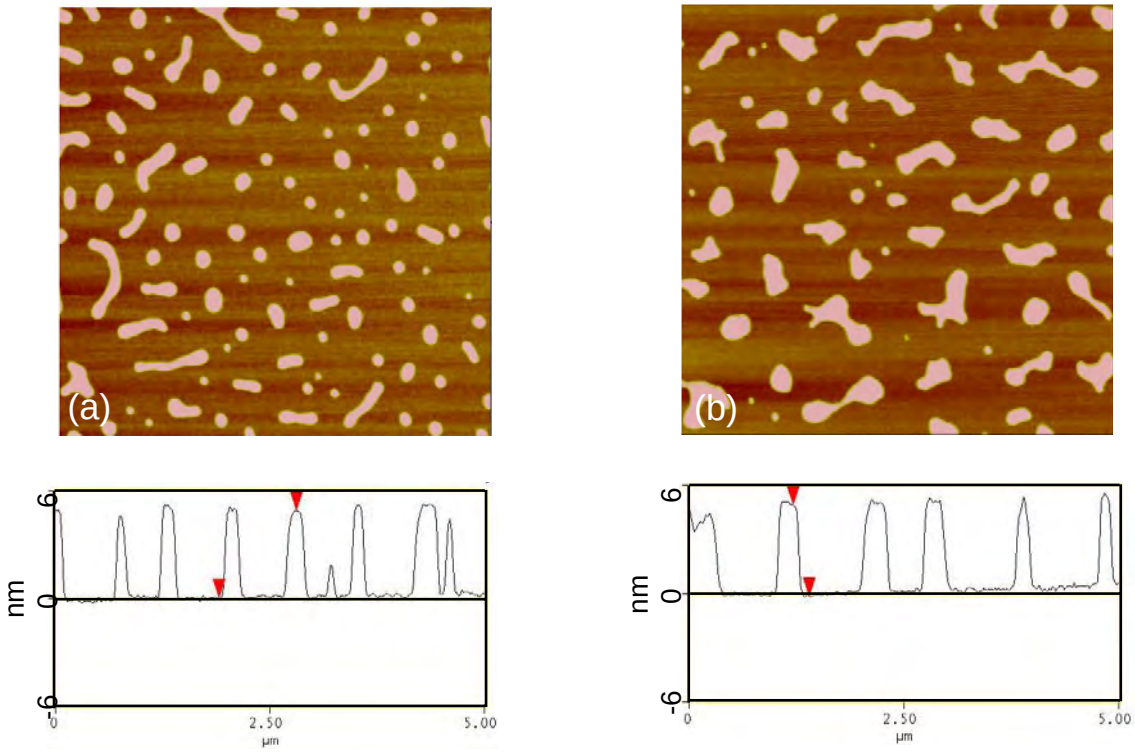

Figure 6.12 Representative plan-view AFM images (5µm x 5µm) and cross-sections of domain structures formed by aerosol deposition of 25%C_{12} PAMAM G4 dendrimer solution on mica; a) f = 0.13, b) f = 0.16.

At the lowest coverages studied (f = 0.13; Figure 6.11a) the dendrimers are organized into dispersed, primarily circular domains (islands) of varying diameters. Some of the domains are extended in form and these linear shapes are consistent with coalescence of neighboring circular domains. All of the dendrimer domains have rounded perimeters. At this coverage, the mean domain size expressed as the diameter (d) of the equivalent circle calculated from the mean area of the domains is ~ 190 nm. Domains of this size contain hundreds of individual dendrimer molecules, although no internal contrast is apparent. A topographic profile along a line selected to pass through a number of domains reveals the fact that the domains have a very consistent height, h, in this case averaging 4.76 nm. The only height deviations observed are when the

section line cuts close to the edge of a domain where the finite size of the AFM tip introduces a non-physical slope from the top of the domain down to the mica surface.

Increasing the coverage to f = 0.16 (Figure 6.12b) leads to similarly dispersed domains with a greater preponderance of larger elongated shapes. The mean domain diameter as defined above is ~ 250 nm. The cross-section again confirms that the domains have a single height (in this case averaging 4.74 nm).

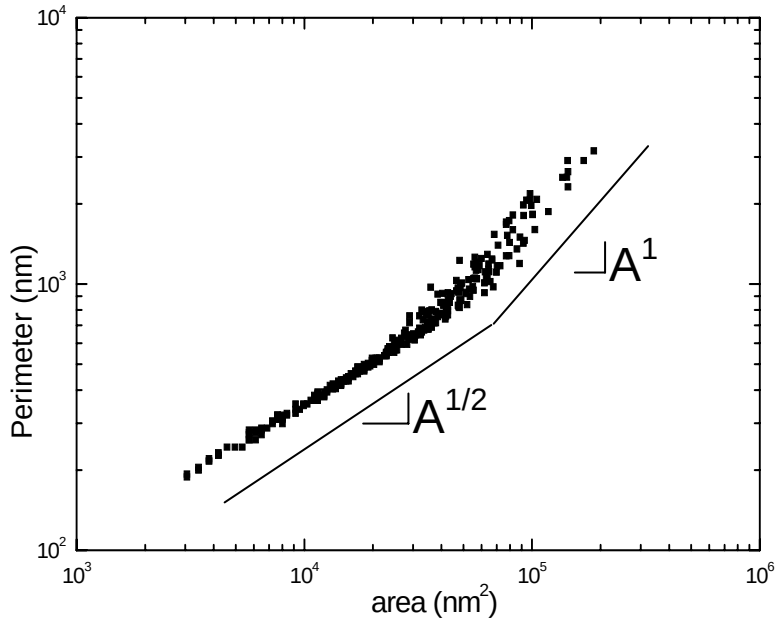

Figure 6.13 Perimeter, P, versus area, A, of the dendrimer domains in Figure 6.12 (a).

It is also useful to quantify the perimeter, *P*, and area, *A*, of the domains in Figure 6.12a and plot them as shown in Figure 6.13. The slope of the *P* versus *A* plot has been used to suggest plausible mechanisms of microstructural evolution[109]. For the smallest domains, each domain is roughly circular and thus $P \propto A^{1/2}$, as observed. The microstructure which evolves at or very near equilibrium as the coverage changes should be independent of the mechanism by which molecular rearrangements may occur. Nevertheless, a possible mechanism for formation of the

larger, elongated domains consistent with both the appearance of the domains and the clearly observed $P \alpha A$ dependence is that these ramified domains could have formed by development of a 'neck' between neighboring, smaller, more circular domains. The coexistence of ramified and compact domains in certain coverage ranges was also observed in the Pb overlayer system[108] and island migration was proposed as the mechanism responsible for microstructural evolution.

To further quantify the structures of the dendrimer self assembly through domain size analysis, individually measured domain areas were converted to equivalent area circles and the diameters of the circles are used as the grain diameter, *d*, in the following statistical analysis. For each experimental domain size distribution a simple arithmetic mean, *d*, and standard deviation, *s*, are reported along with the mean and standard deviation extracted from the lognormal fit to the data, μ and σ, respectively. The lognormal distribution is given by

$$p(x)=[bx(2\pi)^{1/2}]^{-1}\exp[-(\ln x-a)^2/2b^2], \quad (6.2)$$

where *a* and *b* are independent fit parameters. μ and σ are given by

$$\mu = \exp(a+b^2/2), \quad (6.3)$$

and

$$\sigma = \{\exp(2a+b^2)[\exp(b^2)-1]\}^{1/2}, \quad (6.4)$$

respectively.

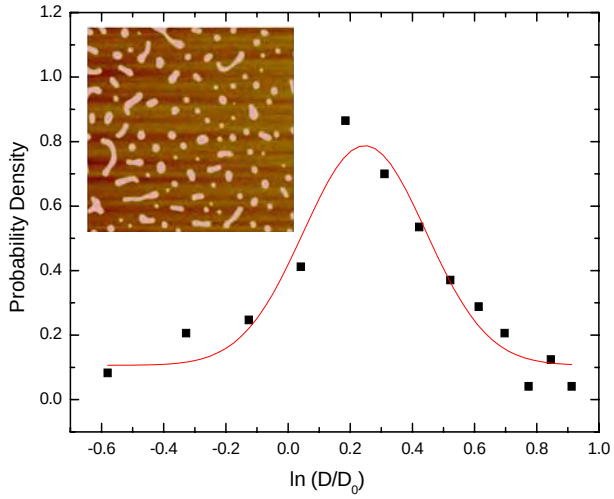

Figure 6.14 Domain size distributions and fit at coverage of f = 0.23.

Two images with dendrimer coverages of f = 0.23 and 0.73 are chosen for the fit. These two coverages represent the 'droplet' and 'inverted droplet' phase as described in Figure 6.11. The experimental domain size distribution for coverage 0.23 appears in Figure 6.14 along with a lognormal fit to the data. The data is in reasonable agreement with the lognormal distribution and yields d = 312.7 nm (μ = 311.3 nm) and s = 197.2 nm (σ = 86.6 nm). The domain size distribution fitting is better in higher coverage 0.73 shown in Figure 6.15. Here the holes are chosen for the analysis. The analysis yields d_{hole} = 236.3 nm ($\mu_{\text{hol e}}$= 227.0 nm) and s_{hole} = 60.0 nm (σ_{hole} = 48.9 nm). For intermediate coverages the dendrimer domains are interconnected networks, making this type of statistical analysis impossible.

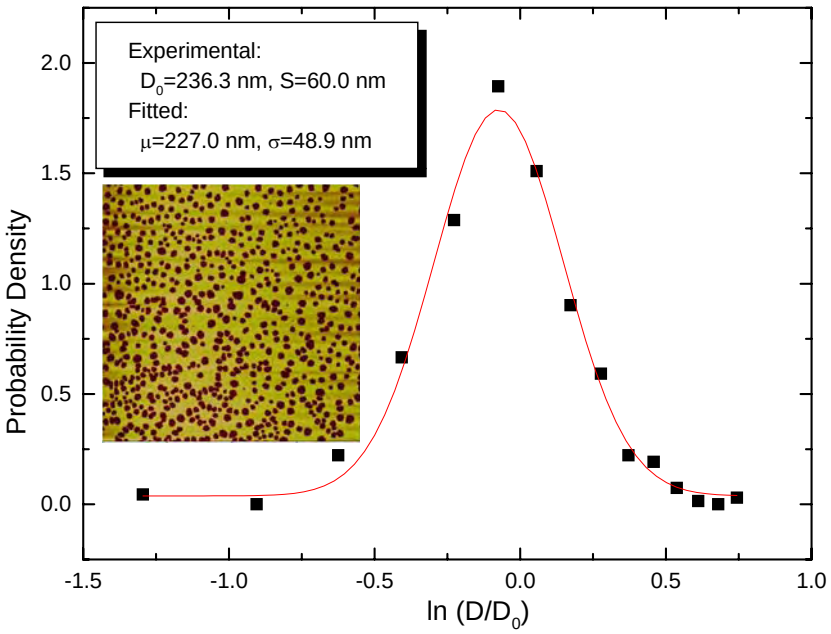

Figure 6.15 Domain size distributions and fit at coverage 0.73.

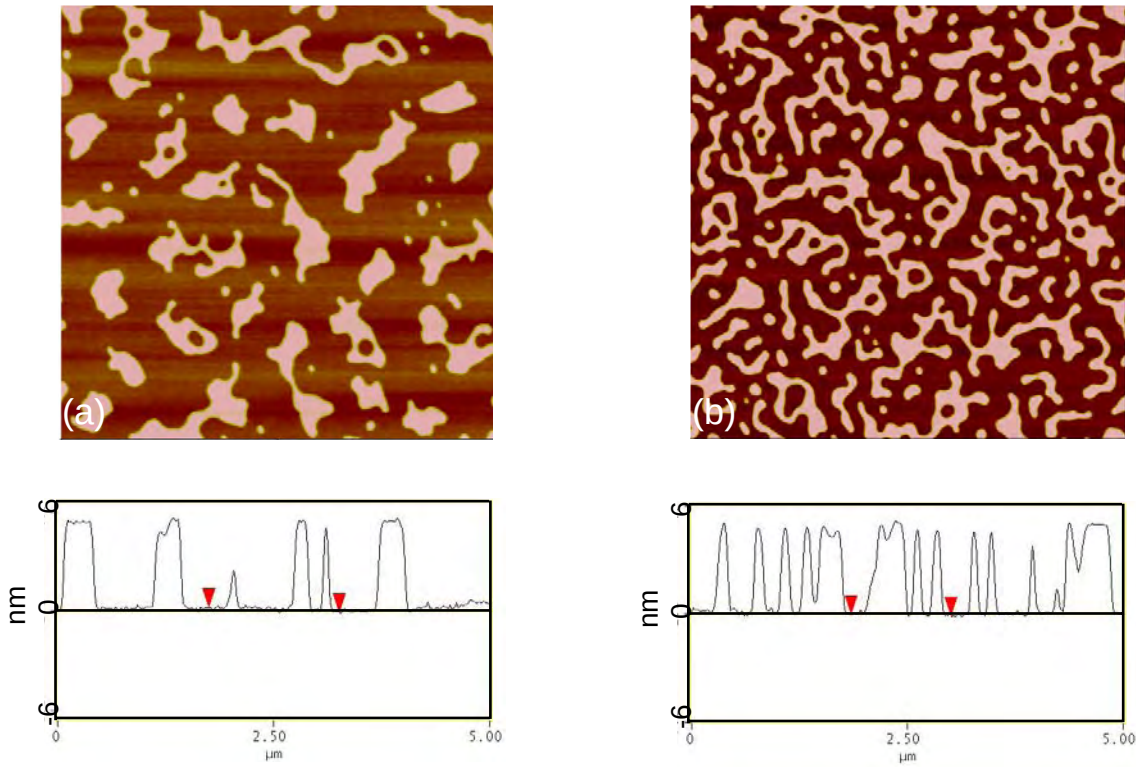

Figure 6.16 Representative plan-view AFM images (5μm x 5μm) and cross-sections of domain structures formed by aerosol deposition of 25%C_{12} PAMAM G4 dendrimer solution on mica; a) f = 0.23, b) f = 0.33.

As the coverage is furthered increased to f = 0.23 (Figure 6.16a), several important features are noted. Most of the domains are elongated but not necessarily along a single direction. Variations in domain width along the length are noted and, very interestingly, many domains contain circular 'holes' which penetrate all the way to the mica surface. The domains are significantly larger (d ~ 310 nm) and the cross-section yields a domain height of h = 4.63 nm. At f = 0.33 (Figure 6.16b) somewhat smaller (d ~ 270 nm), elongated domains creating a labyrinthine structure dominate although some small rounded domains still remain. The holes noted at f = 0.23 are even more prevalent. The dendrimers continue to organize themselves into 1 ML thick structures with h = 4.70 nm at this coverage. The dendrimer domains are clearly nearing their 2D percolation threshold.

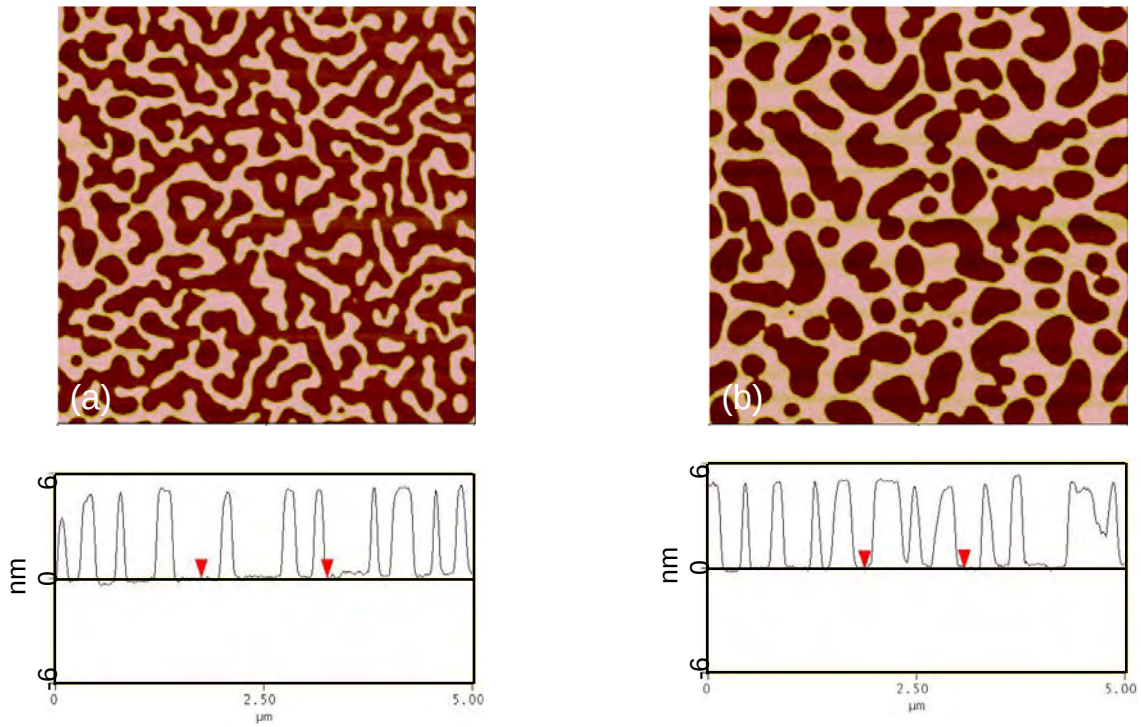

Figure 6.17 Representative plan-view AFM images (5µm x 5µm) and cross-sections of domain structures formed by aerosol deposition of 25%C_{12} PAMAM G4 dendrimer solution on mica; a) f = 0.39, b) f = 0.45.

At f = 0.39 (Figure 6.17a) percolation is reached and the resulting structure can be seen as two interpenetrating contiguous phases, the 1 ML thick dendrimer domains (h = 4.72 nm) and the bare mica surface. At all higher coverages the system is inverted with the dendrimer monolayer regions now the 'matrix' in the two-phase system. At f = 0.45 (Figure 6.17b) the bare mica patches assume primarily elongated forms with rounded edges. The thickness of the dendrimer monolayer remains remarkably consistent through the inversion (h = 4.71 nm at this coverage). As f continues to increase (Figure 6.18a and b; f = 0.52 and f = 0.64; h = 4.70 and h = 4.77) the bare mica patches become smaller and more circular, tracking, in reverse sequence, the evolution observed in the dendrimer domains at low coverage (Figure 6.12). In this coverage range the bare mica surface is the 'inverted droplet' phase. Perimeter versus area analysis of the bare mica patches, as illustrated in Figure 6.13 for the dendrimer domains, yields the same transition in behavior from $P \alpha A$ to $P \alpha A^{1/2}$ as the patches become smaller (Figure 6.18). At higher coverages (f > 0.7; Figure 6.19) the mica patches continue to decrease in size and nearly all are roughly circular (very few elongated forms), mainly $P \alpha A^{1/2}$.

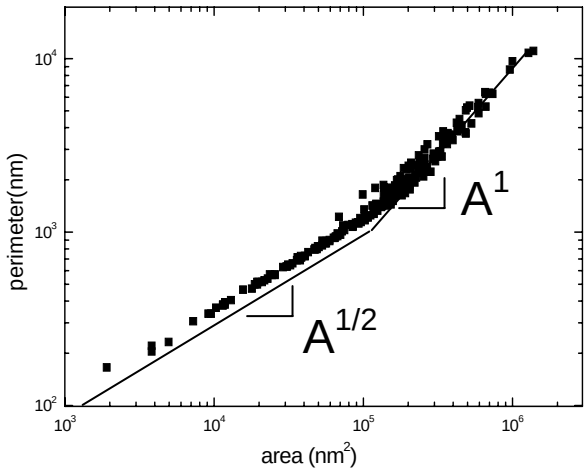

Figure 6.18 Perimeter, P, versus area, A, of the dendrimer domains in Figure 6.17 (b), f = 0.45.

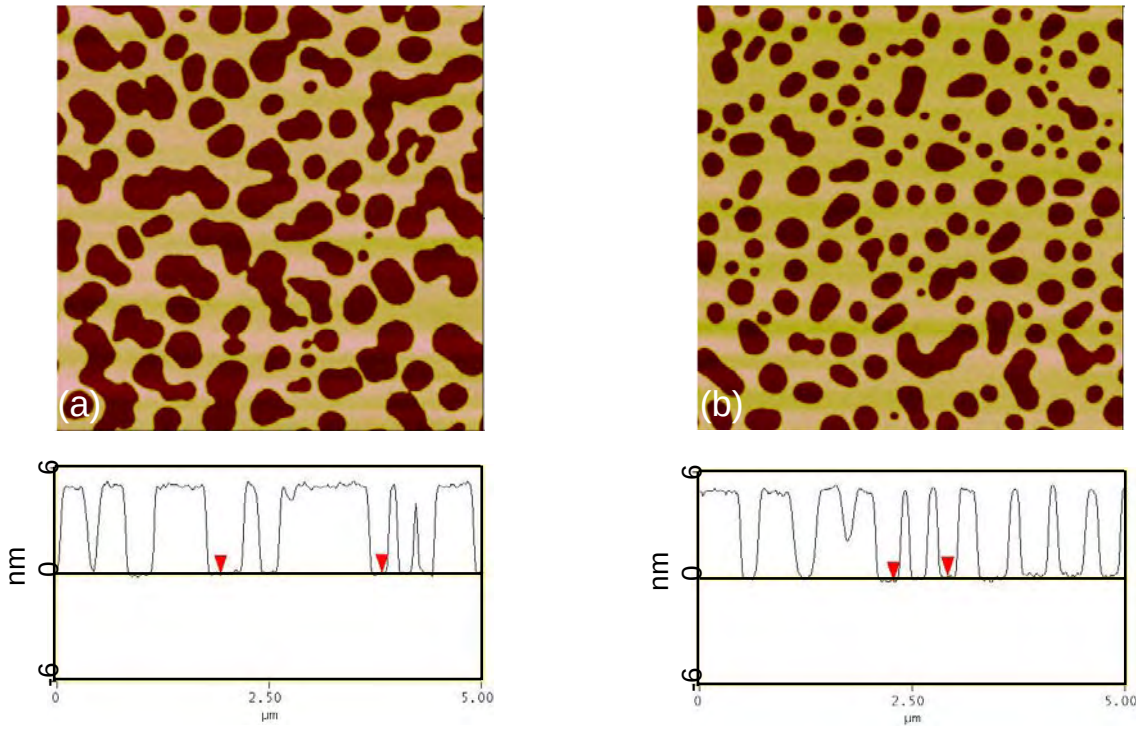

Figure 6.19 Representative plan-view AFM images (5µm x 5µm) and cross-sections of domain structures formed by aerosol deposition of 25%C_{12} PAMAM G4 dendrimer solution on mica; a) f = 0.52, b) f = 0.64.

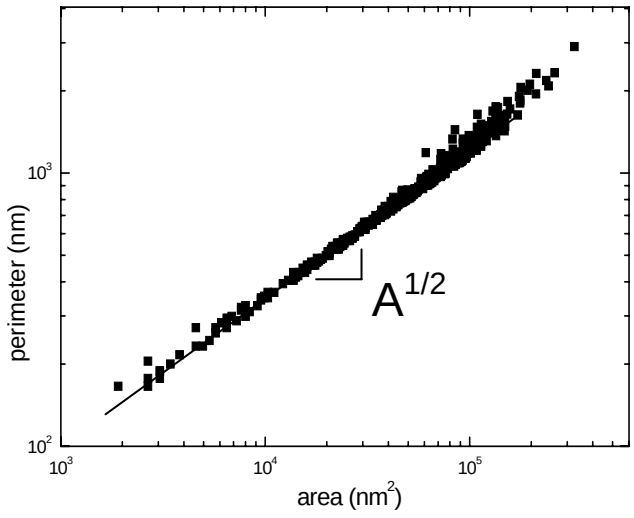

Figure 6.20 Perimeter, P, versus area, A, of the dendrimer domains in Figure 6.19 (b)

Figure 6.12, 16-17, and 19 clearly demonstrate the predicted droplet – stripe – inverted stripe sequence, albeit with a considerable amount of disorder. Figure 6.21 schematically illustrates the expected charge state of the mica surface and dendrimer domains which we propose as the origin of the long range repulsive interaction necessary to stabilize the observed sequence. The mica surface (which when freshly cleaved is covered with K^+ ions) is expected to exhibit a negative charge due to loss of K^+ ions from the mica surface into the pentanol. This surface dissolution and resulting surface charging has been invoked in surface force balance measurements of the interaction between mica surfaces submerged in water[110]. Our assumption is that a negatively charged mica surface is present during the growth of the 2D dendrimer domains. The dendrimer molecules themselves and the domains they form are expected to have a positive surface charge due to protonation of their terminal amine groups. Such positively charged G4 PAMAM dendrimers have been used as one component in electrostatic layer-by-layer deposition of multilayers of oppositely charged dendrimers [6]. In our case, mobile, positively charged dendrimers organize themselves into the observed domain patterns while submerged in pentanol. The dendrimer patterns which form are sufficiently stable to be preserved during evaporation, and show no evidence of the cellular structures which can result from the forces of dewetting[46].

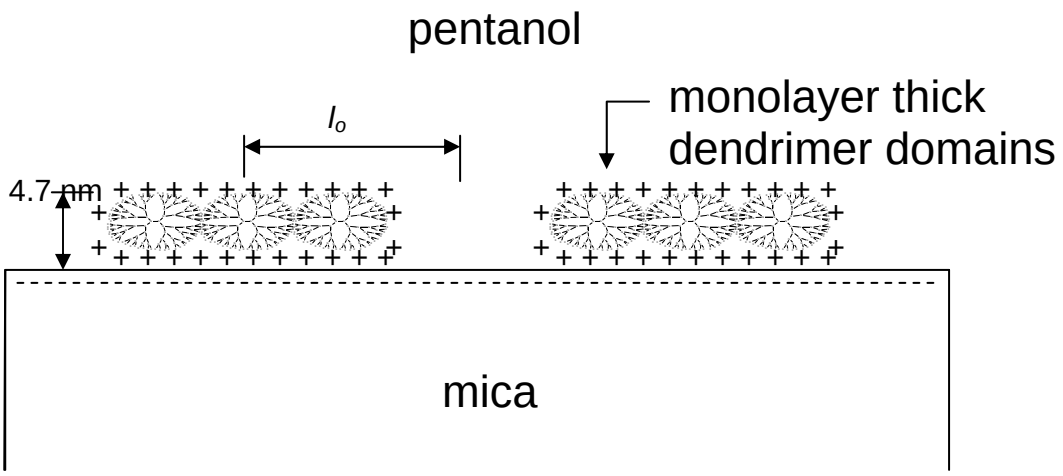

Figure 6.21 Schematic illustration of the expected charge state of the mica surface and dendrimer domains during growth of the 2D dendrimer domains.

A comparison of the predicted dependence of the characteristic length scale, l_o, on coverage, *f*, with experimental measurements, not previously reported, provides an additional test of the validity of physical picture proposed above. This dependence at zero temperature can be derived from reference[99].

$$n = l_0 \exp(I) \tag{6.5}$$

Where *n* is a constant, *I* depends only on the geometry of the domain structure, which is also a function of coverage, *f*, and

$$I(f) = -\ln\sin(\pi f) \tag{6.6}$$

Combine equations 6.5 and 6.6, one can get,

$$l_o \propto 1/\sin(\pi f). \tag{6.7}$$

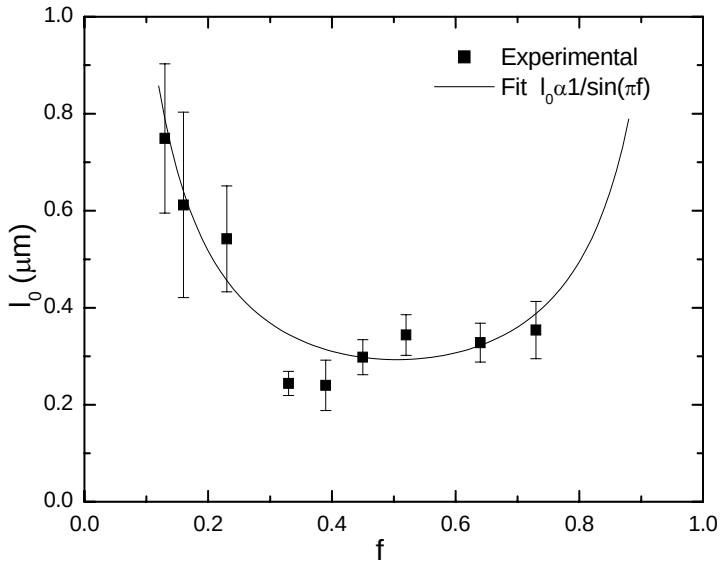

Figure 6.22 Characteristic length, lo, calculated from AFM images, plotted versus coverage, f. Superposed is a best fit using equation (6.7).

An appropriate characteristic length has been calculated from the AFM images by determining the mean number of domain boundary intercepts per length of test line. This is plotted versus coverage in Figure 6.22. Superposed is a best fit using equation 6.5. The general agreement between the theoretical form and the experimental data is good. It is certainly not possible to guarantee that the observed domain structures are completely equilibrated, however, the patterns were found to be stable (only very slight changes in the contours of some domains were noted) when resubmerged in pure pentanol for four hours at both room temperature and 60ºC (discussed in a later section). The degree of disorder and feature size variation found here at finite temperatures is not surprising when compared with related experimental observations. Finite temperatures and the presence of defects in real experimental conditions lead to significantly greater disorder than expected from the zero temperature simulations. The important point to note is that for these types of systems the equilibrium characteristic length is achieved in relatively short times while orientational order and domain shape refinement

continue to evolve over much longer time scales[111]. This behavior supports the significance of Figure 6.17.

The actual value of the characteristic length clearly depends sensitively on the ratio γ_b/γ_d (see equation 6.1). γ_d is proportional to the product of the dielectric constant of the liquid present during domain formation and the contact potential squared. Contact potential measurements with sufficient spatial resolution can, in principle, be made by electrostatic force microscopy (Kelvin probe force microscopy) and related techniques[112]. However, measurements in the presence of a mediating liquid have not been reported and the effect of the liquid on the contact potential (and the interphase boundary energy, γ_b) is not known. Alternatively, electrostatic forces acting on an AFM tip may be measured in solution by force distance curves[113]. A very approximate value for the characteristic length can be calculated by setting the sharpness of the interface equal to the measured molecular layer thickness (4.7 nm), the interphase boundary energy to 10^{-12} N (as reported for Langmuir films[104]), the dielectric constant to 13.9 (the value for pentanol[114]), and the contact potential to 0.5V (in the range reported for alkanethiols on gold[85]). For this set of values $l_o \sim 100$ nm. In order to effectively utilize competing interactions to design domain patterns with controllable length scale direct measurements of contact potentials and interphase boundary energies for various materials combinations are needed. By manipulating the chemistry of the substrate, solution, and dendrimer (or other) molecules to tailor the electrostatic interactions and interphase boundary energy, domain patterns with repeat distances ranging from a few times the molecular size to microns should be achievable.

In conclusion, the predicted domain pattern evolution by competing short-range attractive and long-range repulsive interactions theory is experimentally verified here for the case of dendrimer molecules on mica, a materials system amenable to control of the competing

interactions. This result, along with the coverage dependence of the characteristic domain length scale, is reported for the first time. The domain patterns are fabricated by simple aerosol deposition of dilute solutions of dendrimer molecules in pentanol onto mica followed by slow evaporation. The long range repulsive interaction in this case is electrostatic in origin and is associated with the contact potential between the negatively charged surface of mica submerged in pentanol and the positively charged surface of the dendrimer molecule domains. This interpretation accounts for our observations, is consistent with the physical conditions present in the experimental system, and is in agreement with related interpretations in the literature[108]. However, other possible mechanisms of domain formation, which do not rely on competing short-range and long- range interactions, have not been ruled out.

6.4 AEROSOL SPRAY OF 25%C_{12} PAMAM G4/PENTANOL ON TO HOPG – COMPETING INTERACTION

6.4.1 Introduction

In last section, the long-range repulsive and short-range attractive interaction of competition theory has been proposed to be responsible for the dendrimer domain formation in aerosol spray of 25%C_{12} PAMAM G4/pentanol on to mica surface. The short-range attraction is the interphase energy and the long-range repulsive interaction is electrostatic in origin and is associated with the contact potential between the negatively charged surface of mica submerged in pentanol and the positively charged surface of the dendrimer molecule domains. In this section, highly ordered pyrolytic graphite (HOPG) is used as the substrate. It is expected to remain neutral when submerged in pentanol which could change the long-range repulsive attractions during the dendrimer domain formation process. Different dendrimer domain structures may result.

HOPG is a relatively new form of high purity carbon with ABABAB hexagonal layer structure. The A-A layer distance is 6.7 Å. Like mica, HOPG has an atomically flat surface – making it an excellent substrate for scanning probe microscopy measurements. The fresh smooth surface can be cleaved like mica.

As in the last section, the 0.5% wt. of 25%C_{12} PAMAM G4/pentanol solution system is aerosol sprayed onto the freshly cleaved HOPG surface by using an EFFA® Spray Mounter. The experimental conditions were kept as much the same as possible. The dried dendrimer surface structures are again characterized by AFM in 'tapping mode' with a standard tip. Freshly cleaved bare HOPG surfaces are extremely flat exhibiting rms roughnesses of 0.09 nm, while the roughness at the free surface of the dendrimer domains is just slightly higher. All images shown are representative of regions extending several hundred microns or more. The patterns shown are stable under ambient conditions over many weeks.

6.4.2 Results and Discussion - HOPG

The evolution of dendrimer domain structure and morphology as a function of area fraction of HOPG substrate by dendrimer molecules will again be used to sort and discuss the results. For comparison, the dendrimer domain patterns on mica substrates at similar coverages will be presented as well. Again, all the dendrimer domains have essentially the ML thickness (~ 4.7 nm) of 25%C_{12} PAMAM G4 (to be shown later). The dendrimer domains show a pure 2D structure on HOPG with no evidence for formation of a partial second or subsequent dendrimer layer. This observation is in agreement with the results in section 6.3. This experimental realization of a 2D, two-phase system (1ML thick dendrimer domains and bare HOPG) is

characterized by AFM. The dark contrast in the image is HOPG substrate and the bright contrast is the dendrimer molecules.

At lower coverage, the dendrimer domains look similar on mica and HOPG substrates. Figure 6.23 shows the molecular domain structure on HOPG (f = 0.22, Figure 6.23a) and mica (f 0.23, Figure 6.23b) substrates. All of the dendrimer domains have rounded perimeters. On both substrates, most domains are elongated but not necessarily along a single direction. There are variations in domain width along the length and the domains also contain the circular “holes” which penetrate all the way to the mica surface. Note that on the HOPG substrate, there are several steps in the substrate (indicated by an arrow).

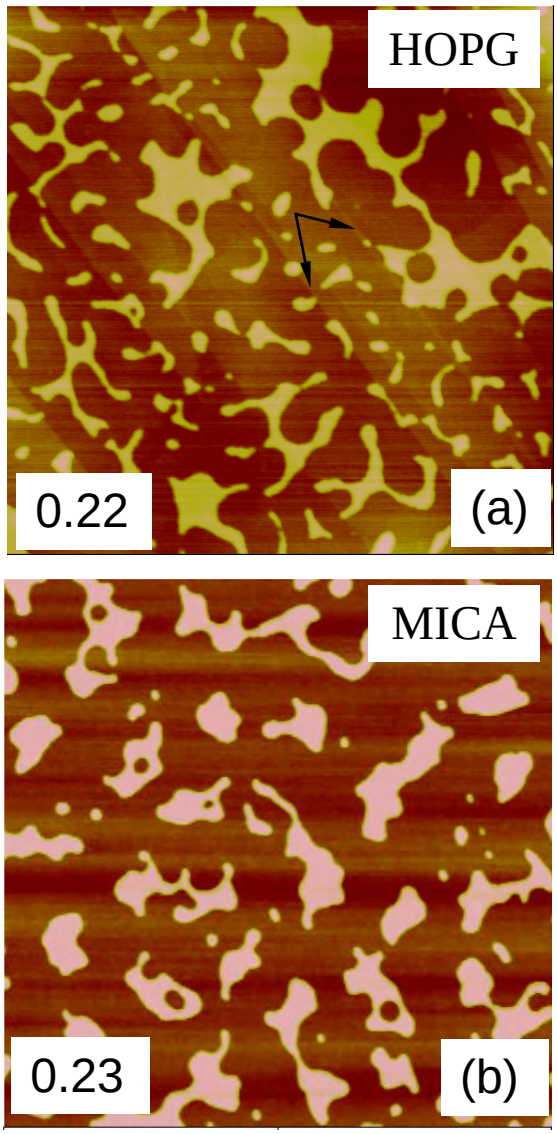

Figure 6.23 Representative plan-view AFM images (5μm x 5μm) of domain structures formed by aerosol deposition of 25%C_{12} PAMAM G4 dendrimer solution on (a) HOPG, f = 0.22 and (b) mica, f = 0.23.

When the coverage is increased to ~ 0.46 (Figure 6.24), the bare HOPG patches become smaller and the holes of HOPG become distinctly faceted. On the mica substrate, the dendrimer domains (or mica patches) assume primarily elongated forms with rounded edges. The dendrimer domains on HOPG seem to align along certain directions, the step edges of the HOPG substrate. Figure 6.25 shows a cross-sectional view of the HOPG substrate (shown in the line of

Figure 6.24a). We can see the depth between the dendrimer level and HOPG level remains consistent at ~ 4.7 nm – equivalent to a monolayer of 25%C_{12} PAMAM G4 dendrimer as was found in mica substrate. The steps found in HOPG substrate, directed by the arrow in Figure 6.24a, have a step height of 0.69 nm – essentially two of the HOPG atomic layers (ABA: 0.67 nm). This step is clearly seen in Figure 6.24a. It is clear that the dendrimer domain formation has been significantly influenced by the nature of the HOPG substrate structure and steps causing alignment and faceting. These features, while interesting, make a direct comparison with the competing interaction theory problematic.

When f is increased to 0.52 (Figure 6.26a), the faceted dendrimer domains (or HOPG patch holes) become more dominant. It is very obvious in Figure 6.26a that the bare HOPG patches are aligned in one direction – the step line of the substrate. By comparison, on mica substrates the bare mica patches become smaller and more circular, tracking, in reverse sequence, the evolution observed in the dendrimer domains at low coverage (see section 6.3). Dendrimer domain formation on HOPG exhibits features which still seem broadly similar to the mica results and yet highly influenced by the anisotropic HOPG substrate surface and its steps.

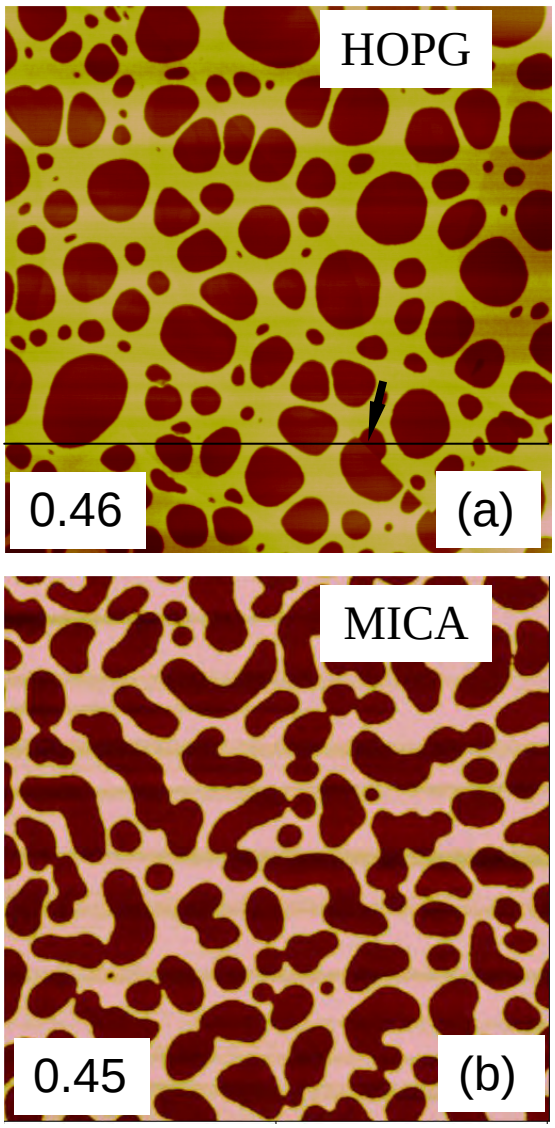

Figure 6.24 Representative plan-view AFM images (5μm x 5μm) of domain structures formed by aerosol deposition of 25%C_{12} PAMAM G4 dendrimer solution on (a) HOPG, f = 0.46 and (b) mica, f = 0.45.

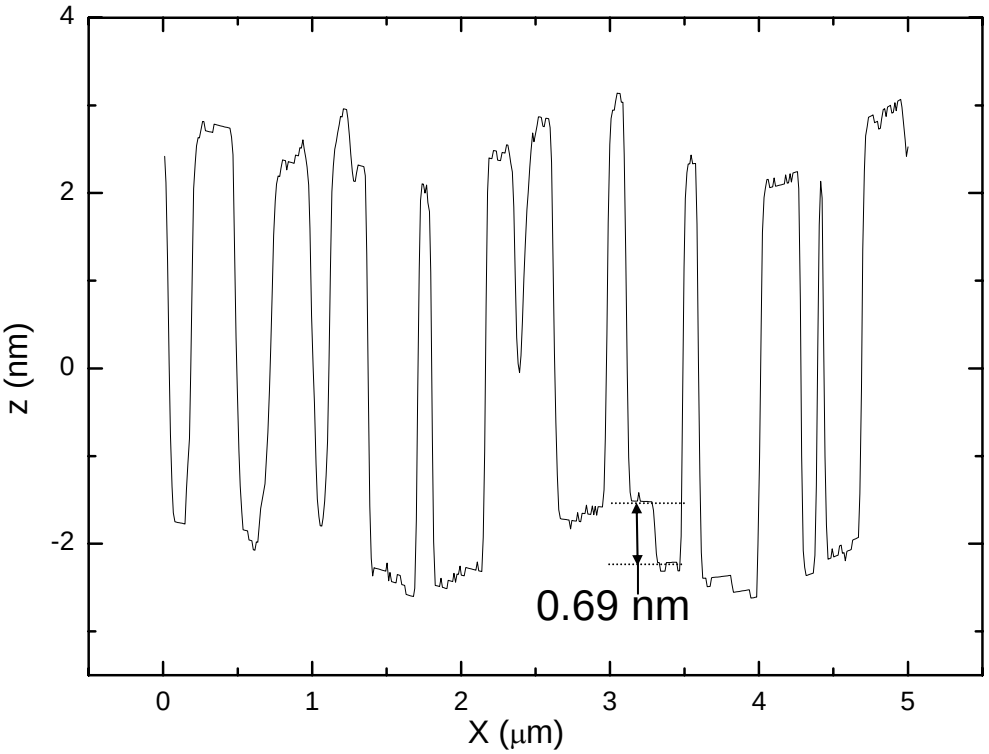

Figure 6.25 Section analysis of domain structures in Figure 6.19a.

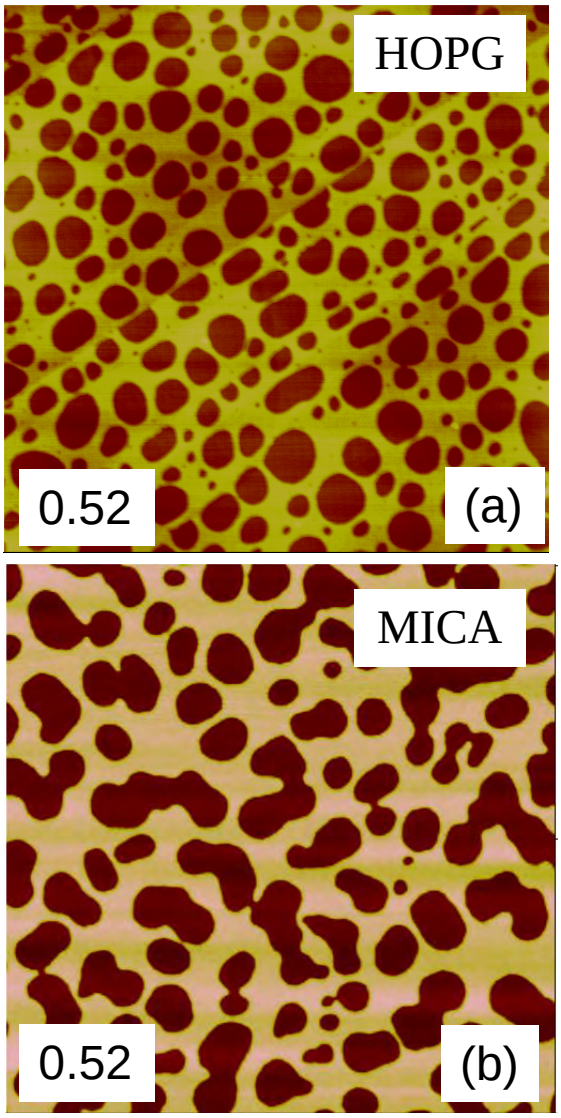

Figure 6.26 Representative plan-view AFM images (5μm x 5μm) of domain structures formed by aerosol deposition of 25%C_{12} PAMAM G4 dendrimer solution on (a) HOPG and (b) mica at f =0.52.

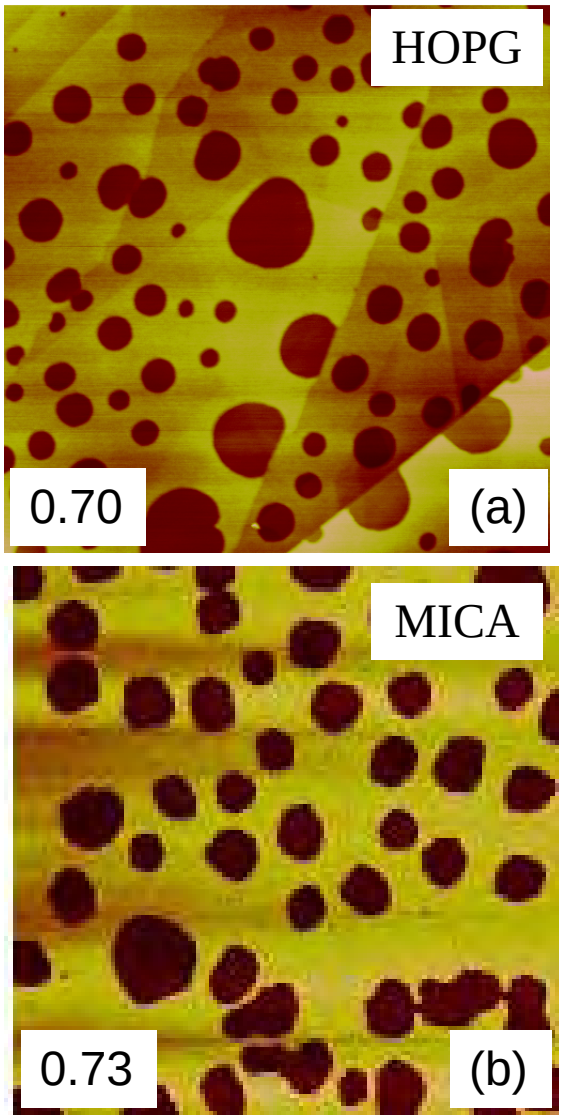

Figure 6.27 Representative plan-view AFM images (5μm x 5μm) of domain structures formed by aerosol deposition of 25%C_{12} PAMAM G4 dendrimer solution on (a) HOPG, f = 0.70 and (b) mica, f = 0.73.

At even higher coverage (f = 0.70, Figure 6.27a), the dendrimer domains are not as aligned as in the medium coverage (f = 0.52). The HOPG patches holes become less faceted.

6.5 THERMAL STABILITY OF DENDRIMER DOMAINS

It is useful to understand something about the thermal stability of dendrimer domains at elevated temperature in a liquid environment. The thermal stability experiments were executed in an ISOTEMP 110 from Fisher Scientific®. The substrate with dried dendrimer patterns is submerged into pentanol at a fixed temperature of 60 ºC for 4 hours. The sample is then taken out and allowed dry in air. The AFM images before and after the bath experiment are recorded. Note that it is extremely difficult to acquire the AFM image at exactly same spot before and after the thermal stability experiment. AFM images of similar dendrimer coverage regions are thus compared.

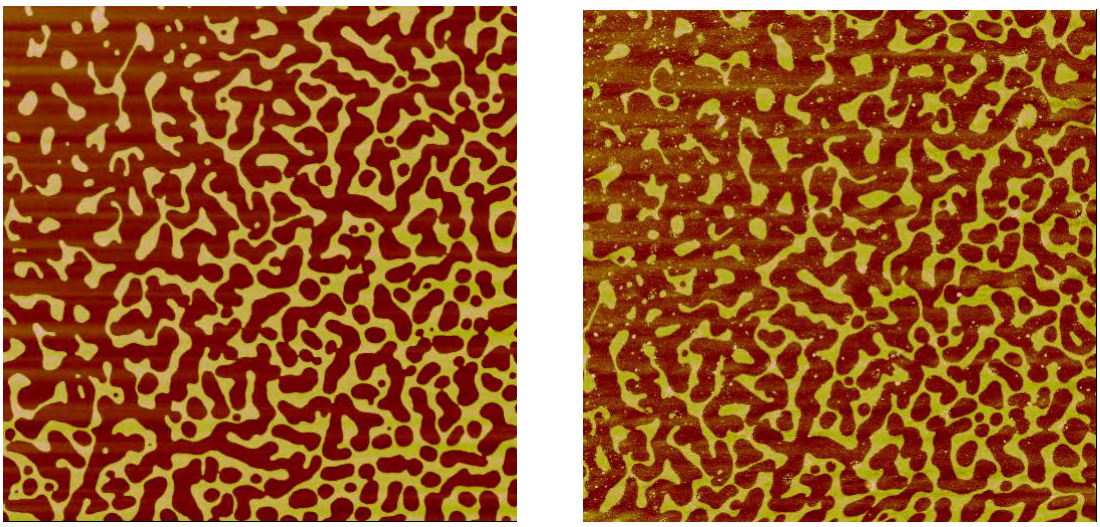

Figure 6.28 AFM topography of dendrimer nanopatterns before (Left, f = 0.31) and after (Right, f = 0.28) the liquid bath experiment. The sample is held in pentanol liquid at 60 ºC for 4 hrs.

Figure 6.28 shows representative AFM topographies of 25%C_{12} PAMAM G4 dendrimer on mica surface before and after the thermal stability experiment. The area fractions of the two images are 0.31 (before) and 0.28 (after) respectively. Although the images are not recorded in

the same spot, these images demonstrate that the dendrimer patterns are very similar and remain intact after the thermal stability experiment. The surface of the sample after the thermal stability experiment is slightly contaminated by the re-immersion. At higher dendrimer fraction (Figure 6.29), the patterns still remain stable after the thermal treatment. Once again the surface became slightly contaminated. The domain structures, however, remain very clear.

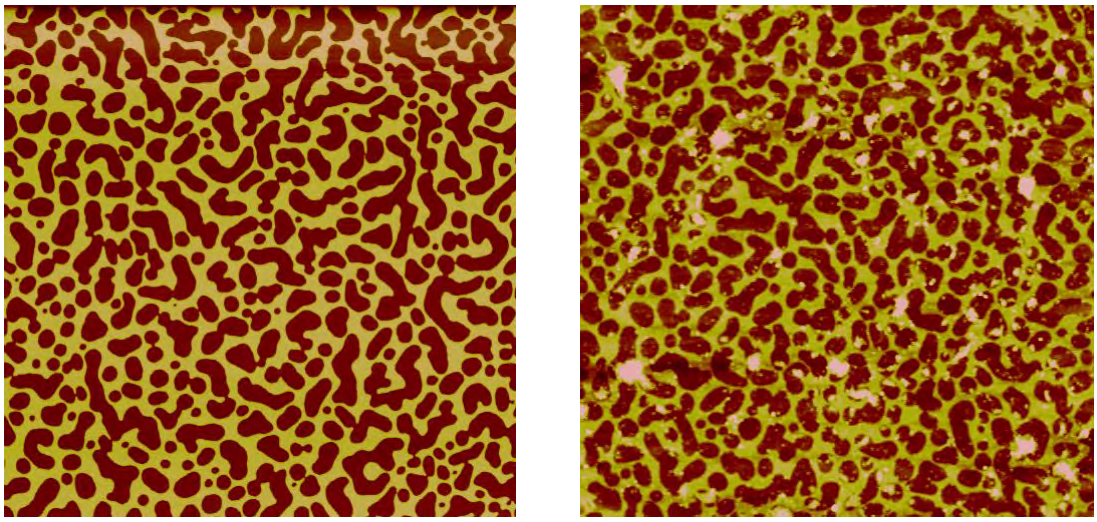

Figure 6.29 AFM topography of dendrimer nanopatterns before (Left, f = 0.39) and after (Right, f = 0.42) the liquid bath experiment. The sample is held in pentanol liquid at 60 ºC for 4 hrs

6.6 CHAPTER SUMMARY

In this chapter aerosol deposition of dilute dendrimer solutions onto atomically flat substrates has been used to fabricate a sequence of two-dimensional dried dendrimer film patterns with structures and morphologies very different from those observed for standard dipping/rinsing procedures. In standard PAMAM G4/Ethanol/Mica systems, the processes of rapid evaporation followed by dewetting via heterogeneous nucleation of dry patches appears to determine most of the complex film structures observed, except at low equivalent layer thicknesses. A clear transition from dispersed dendrimer islands, to cellular structures with a

superposed island pattern, to contiguous dendrimer network films has been documented as a function of increasing equivalent dendrimer layer thickness. Under these processing conditions there is a strong tendency for G4 dendrimers to organize themselves into 2 ML thick structures (sometimes with a partial second level at 4 ML). This may be associated with the enhanced stability/adhesion of 2 ML structures against the forces of dewetting which may tend to 'strip' dispersed dendrimer molecules from the mica surface.

In 25% C_{12} PAMAM G4/pentanol solution systems, both Mica and HOPG are used as the substrates. The competing short-range attractive and long-range repulsive interactions theory is proposed as the explanation for the domain pattern formation. This result, along with the coverage dependence of the characteristic domain length scale, is reported for the first time. The long range repulsive interaction in this case is electrostatic in origin and is associated with the contact potential between the negatively charged surface of mica (or neutral HOPG surface) submerged in pentanol and the positively charged surface of the dendrimer molecule domains. This 25% C_{12} PAMAM G4/pentanol/mica formed structure is also very stable which makes it an excellent choice for the study of physical intermixing between the metal overlayers and dendrimer molecules (Chapter 7). The consistent step height (ML) is excellent for AFM topography contrast before and after the metal deposition – especially when the step height must be monitored for different thick metal films deposition.

The importance of electrostatic interactions in the mechanism for domain formation found for the 25% C_{12} PAMAM G4/pentanol/mica system motivated work on developing a new charge storage film which is found in Appendix A. A charge storage film with appropriate characteristics could be used to directly demonstrate electrostatic patterning of dendrimer molecules.

7.0 RESULTS PART 3 - PHYSICAL INTERMIXING BETWEEN METAL OVERLAYERS AND DENDRIMER DOMAINS

7.1 INTRODUCTION

The interaction of metals with organic layers has received considerable attention due to its importance in determining the reliability and durability of many technological devices and its relevance to future applications based on hybrid organic/inorganic nanoscale systems. We have used dendrimer monolayers as the organic substrate in the study of metal–organic interfacial reactions and nanocomposite formation[34, 40]. In previous work[34, 40] we have examined the interaction of ultrathin (< 20 nm) metal layers with dendrimer monolayers adsorbed on the native oxide of silicon wafers. Vapor or sputter deposition of metal onto the monolayer yields hybrid metal/dendrimer composites with surprising physical and mechanical behavior. Among the findings to date are significant reductions in the roughness of deposited metal films mediated by dendrimer monolayers, a substantial increase in the nanomechanical hardness of ultrathin Au when deposited on a dendrimer adlayer, the occurrence of interfacial reactions, including the formation of metal nitrides, following deposition of reactive metals such as Co and Cr on amine-terminated dendrimer monolayers, and strikingly different deformation modes associated with nanoscratch events on ultrathin Cu and Cr layers deposited on SiO_x with and without a dendrimer underlayer. Some of these effects have been described in this dissertation in Chapter 5. The effects observed are likely related to at least partial penetration of the deposited metal into the dendrimer underlayer. Preliminary analysis of the chemistry of the near surface region

by X-ray Photoelectron Spectroscopy (XPS) analysis and the topography by Atomic Force Microscopy (AFM) profilometry has been reported.

In this chapter, we will combine the methods used in Chapters 5 and 6 to prepare structured overlayers – i.e., dendrimer domain *patterns* (which only partially cover the original substrate) coexisting with bare substrate patches will be used as a structured substrate for subsequent metal overlayer deposition. This method should conveniently allow for simultaneous metal film formation on both the bare substrate and the dendrimer underlayer in a single deposition on a single sample.

7.2 EXPERIMENTAL DESCRIPTION

We follow the methods described previously[46] to fabricate discontinuous dendrimer film patterns on mica substrates. All the dendrimer structures were produced by aerosol deposition and subsequent evaporation of 0.05 weight percent (wt.%) pentanolic solutions of 25%C_{12} PAMAM G4 dendrimers (48 primary amino surface groups and 16 [N-(2-hydroxydodecyl)] surface groups, theoretical molecular weight 20,113 amu) obtained as a 10 wt.% methanolic solution from Aldrich (Milwaukee, WI). This dendrimer was selected because the N-(2-hydroxydodecyl) chains which replace 25% of the terminal amine groups found in a standard G4 PAMAM dendrimer were expected to enhance the dendrimer/substrate interaction leading to stronger adhesion while maintaining surface mobility sufficient to allow the system to approach equilibrium. It is already well established that poly(amidoamine) (PAMAM) dendrimers, which are roughly spherical in solution, “collapse” when adsorbed onto substrate surfaces. are typically something less than half the diameter in solution, independent of generation[2, 115]. Based on this

general tendencies noted above, a 25%C_{12} PAMAM G4 monolayer (ML) adsorbed on a substrate would be expected to have a height of 4 – 5 nm. The pentanolic solutions were prepared by simple volumetric dilution using pipettes with disposable tips from fresh commercial methanol-based solutions. The extremely uniform thickness (1 ML) and flatness of the dendrimer film structures discussed below are consistent with dendrimers dispersed at the molecular level both in the aerosol droplet and following coalescence on the substrate, and not agglomerated into various sized assemblies prior to deposition. Grade V-1 Muscovite mica was used (SPI Supplies ®) for all experiments.

A 99.99% Au target was used to deposit Au thin films onto the previously prepared dendrimer patterned substrates. DC magnetron sputtering (base pressure: 2.7×10^{-5} Pa, working gas: 99.999% Ar, working pressure: 5mTorr) at a power density of 4.9 watt/cm^2 and a working distance of 80 mm yielded a deposition rate of ~ 6Å/s. A clean Si wafer with simultaneously deposited Au films was used to measure deposition rates and thus control overlayer thicknesses. A simple tape 'mask' was applied to the wafer before deposition. After the deposition, the tape was removed from the wafer, leaving a clear step between the Au surface and Si substrate which can be conveniently measured by AFM. Lateral Force, and Force Modulation Microscopy (LFM, and FMM) (Digital Instruments, Inc., model D-3100, FESP tip from DI) are also used to investigate the properties of the patterned dendrimer and Au/dendrimer structures.

7.3 RESULTS AND DISCUSSION

Figure 7.1 documents the typical evolution of dendrimer domain structure and morphology as a function of area fraction, *f* (or 'coverage') of a mica substrate covered by dendrimer molecules. The sectional analysis (not shown) shows that all of the dendrimer domains have essentially the same thickness (~ 4.7 nm) independent of *f* which corresponds well to the 1 ML thickness expected for 25%C_{12} PAMAM G4. Under these conditions this is an experimental realization of a 2D, two-phase system with the 1 ML thick dendrimer domains and the bare mica serving as the two phases (see Chapter 6 for further details). The dark contrast in the images is the mica substrate.

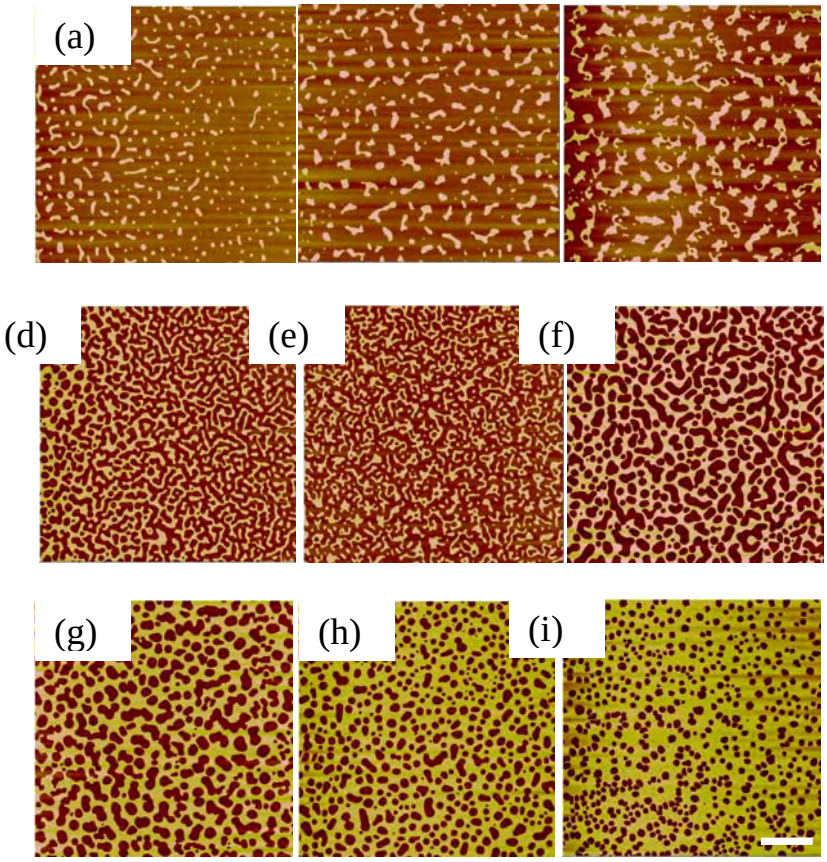

Figure 7.1 AFM topography of dendrimer domains (10μm×10μm) as a function of coverage f, f = (a) 0.13, (b) 0.16, (c) 0.23, (d) 0.33, (e) 0.39, (f) 0.45, (g) 0.52, (h) 0.64, (i) 0.73. The bar is 2 μm.

The evolution of domain patterns as a function of area fraction follows the sequence: circular islands of dendrimer in the matrix of mica substrate (the droplet phase, Figure 7.1a, 1b, and 1c), alternating elongated domains of dendrimer and mica (the striped phase, Figure 7.1d, 1e, and 1f), and circular islands of mica in a matrix of dendrimer (the inverted droplet phase, Figure 7.1g, 1h, and 1i) which is in agreement with the competing interaction theory[99, 108]. The long range repulsive interaction in this case is electrostatic in origin and is associated with the contact potential between the negatively charged surface of mica submerged in pentanol and the positively charged surface of the dendrimer molecule domains. The short range attraction is the interphase energy[47].

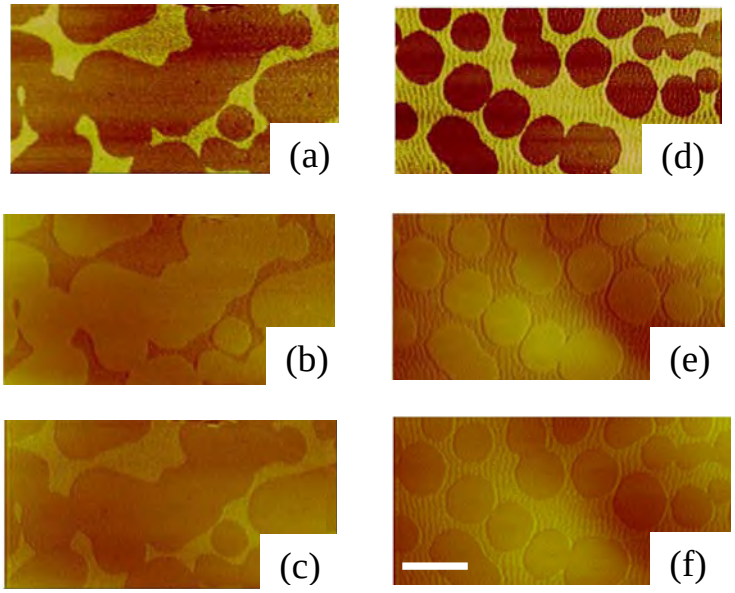

Figure 7.2 Lateral Force Microscopy (LFM) of the dendrimer patterns at f = 0.23 (left) and 0.40 (right). (a), (d) topography; (b), (e) friction by retrace line; (c), (f) friction by trace line. The bar is 1 μm.

LFM was used to evaluate the friction between the tip and sample surface as shown in Figure 7.2. Dendrimer patterns at two coverages (*f* = 0.23 and 0.40) were selected for the friction force mapping. The LFM is a non-destructive method to measure the friction contrast

between the tip and sample surface during the scanning. The normal force is ~10^{-10} N. During the LFM scan, the cantilever scans laterally (perpendicular to their lengths) along the surface. The cantilever torques more while transiting high-friction sites while low-friction sites tend to torque the cantilever less. The relative measure of lateral forces encountered along the surface yields a map with contrast correlated to the magnitude of the local friction. Note that the friction data signal inverts as the scan direction is reversed (from trace and retrace scan direction). In a friction contrast image, the image produce from the trace scanning lines would be darker in low-friction areas than that in high-friction areas. Conversely, the image produced from the retrace would be lighter in a low-friction area. This is a standard way to verify the origin of the data.

Figures 7.2a and 2d are standard topographic images of the patterns and yield a dendrimer height of ~ 4.7 nm, corresponding to the 1 ML thickness; Figures 7.2b and 2e are the friction contrast maps of the same region by LFM retrace lines. Due to the nature of LFM scanning mode, the relative signal strengths invert as the scan direction is reversed. This can be used to confirm the validity of the data. Figures 7.2c and 2f are friction images mapped using trace lines. In retrace line images, the lighter the contrast in the friction image, the lower the friction force between the tip and surface. The contrary is true for trace line images. From Figure 7.2 it can be concluded that the friction between the tip and dendrimer molecular layer is larger than that between the tip and the bare mica surface. This observation is in agreement with expectations based on the fact that dendrimers have a large fraction of straight molecular end groups at their surface which increase the friction when they are brought into contact with the tip[116].

In order to study the intermixing between the metal films and dendrimer underlayers, a full sequence of Au thicknesses films deposited by DC magnetron sputtering was undertaken to

better understand the penetration of Au into the dendrimer domains. The thickness of Au film was measured directly by AFM. Figure 7.3-6 show the AFM plane and sectional scan of the Au/dendrimer patterns at different Au thicknesses. Figure 7.7 shows the AFM line profiles of the Au films deposited onto the dendrimer patterns for different Au thickness depositions. It is very clear that the step height *decreases* as the Au thickness increases. The step length versus Au thickness is plotted in Figure 7.8. Both Figure 7.7 and Figure 7.8 show that before the deposition of the Au film, the step height between the dendrimer and mica surface is ~ 4.7 nm, corresponding to 1 ML of 25%C_{12} PAMAM G4 dendrimer on mica. After deposition of 2 nm or more of Au film, the step size *decreased* to ~ 3 nm, ~1.7 nm less than the original step height. This is an indication that the relatively open structure of the dendrimer molecules and the non-reactive nature of the sputtered Au atoms results in the equivalent of 1.7 nm of Au penetrating into and 'intermixing' with the dendrimer underlayer. Beyond 2 nm the deposited Au is incorporated on top of the growing Au film whether there is a dendrimer layer beneath or not. The linear fit of the step height versus Au thickness before saturation yields a step height of 4.7 nm without Au deposition (the dendrimer monolayer height) and a slope of -0.8 nm in step height per nm of deposited Au. In other words, up to saturation ~ 80 % of the Au atoms mix are incorporated into the dendrimer monolayer and thus contribute to the step height change. This physical intermixing between the Au film and the dendrimer underlayer may be important in understanding the improvement in film quality reported previously[31, 40].

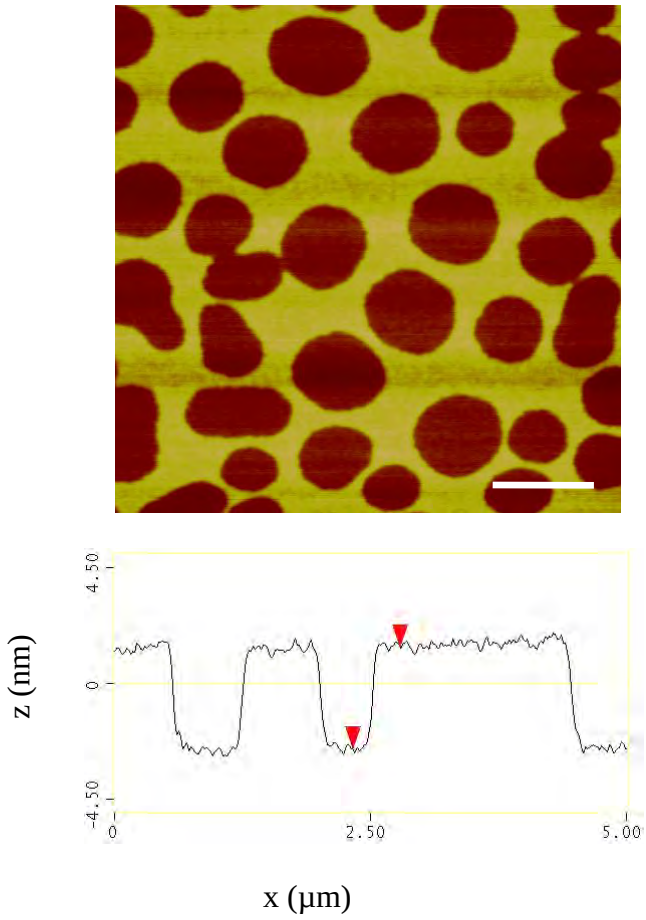

Figure 7.3 Representative plan-view AFM images (5μm x 5μm) and cross-section for a 1 nm Au film deposited on a dendrimer pattern (the bar marks 1 μm).

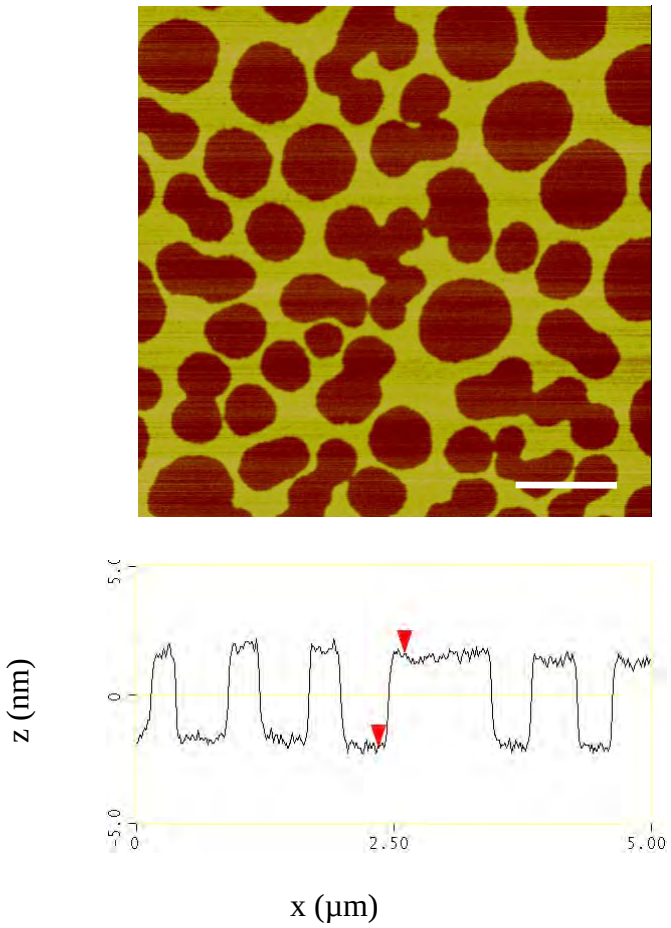

Figure 7.4 Representative plan-view AFM images (5μm x 5μm) and cross-section for a 1.5 nm Au film deposited on a dendrimer pattern (the bar marks 1 μm).

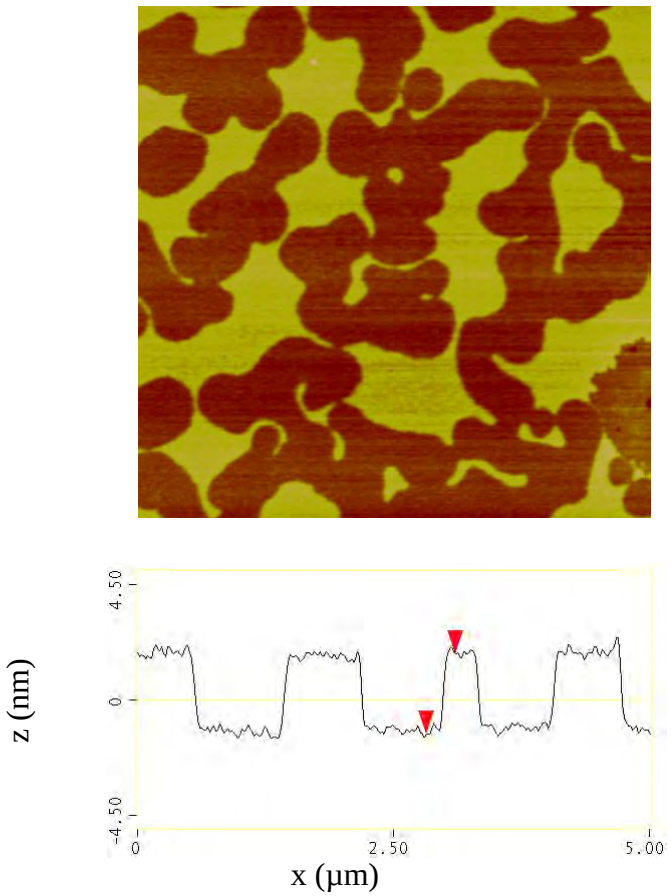

Figure 7.5 Representative plan-view AFM images (5μm x 5μm) and cross-section for a 2 nm Au film deposited on a dendrimer pattern (the bar marks 1 μm).

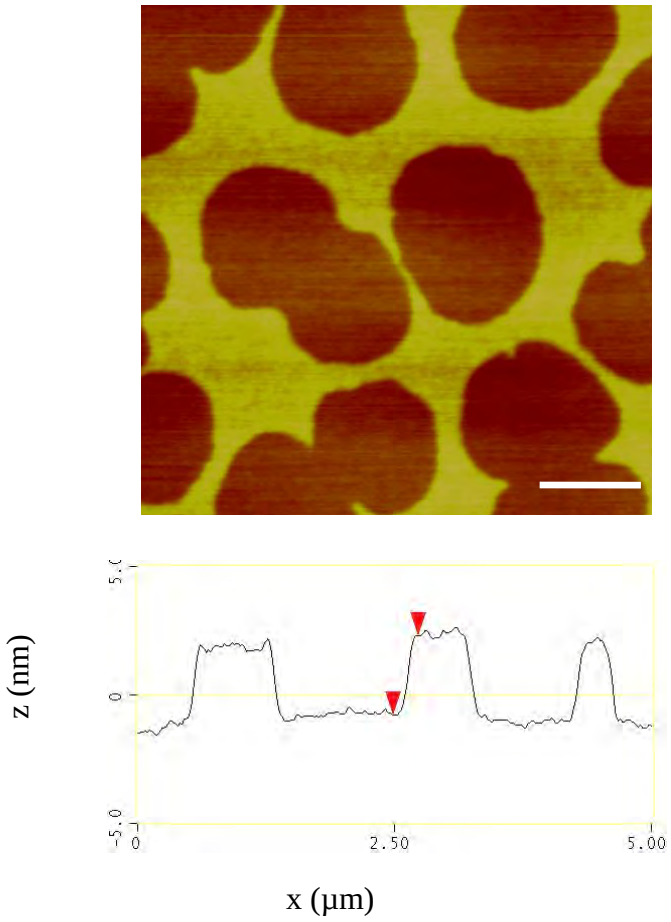

Figure 7.6 Representative plan-view AFM images (5µm x 5µm) and cross-section for a 3 nm Au film deposited on a dendrimer pattern (the bar marks 1 µm).

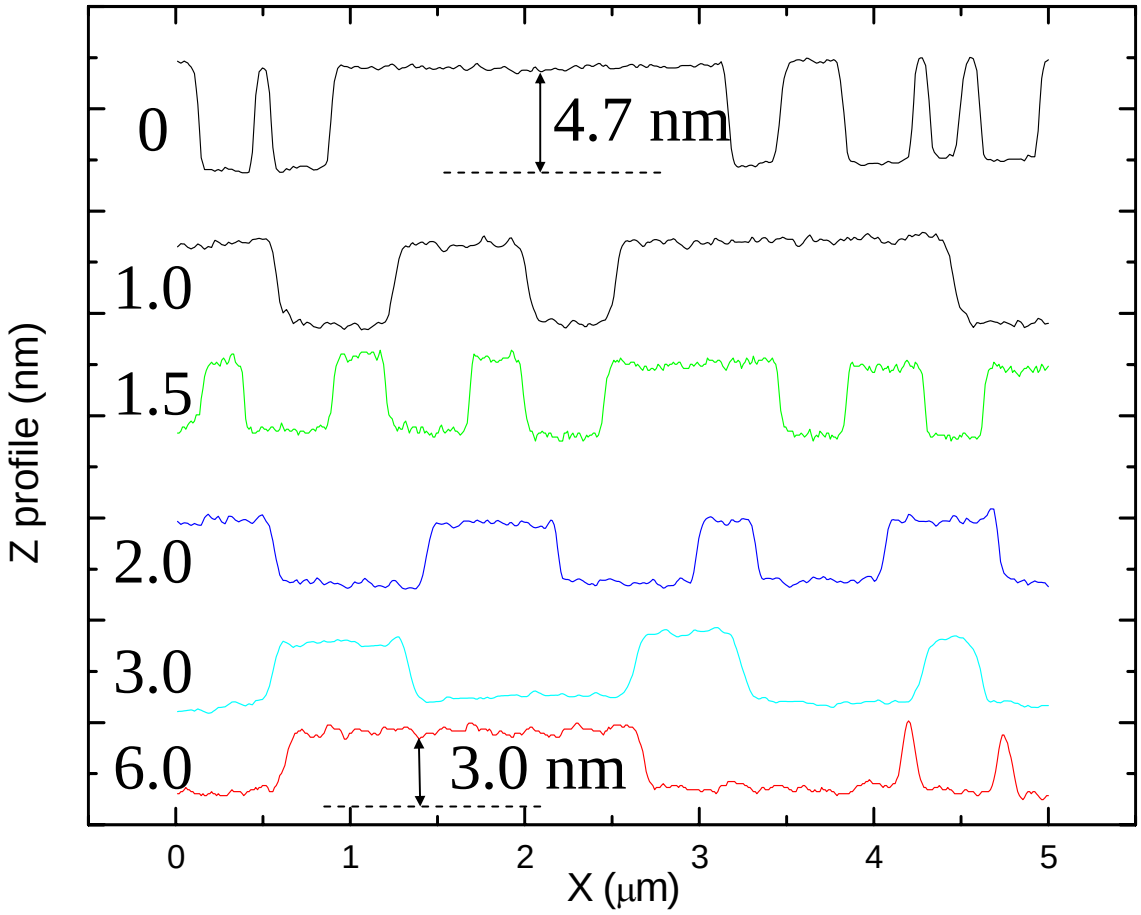

Figure 7.7 Line profile of different Au thickness deposited onto the dendrimer domain patterns.

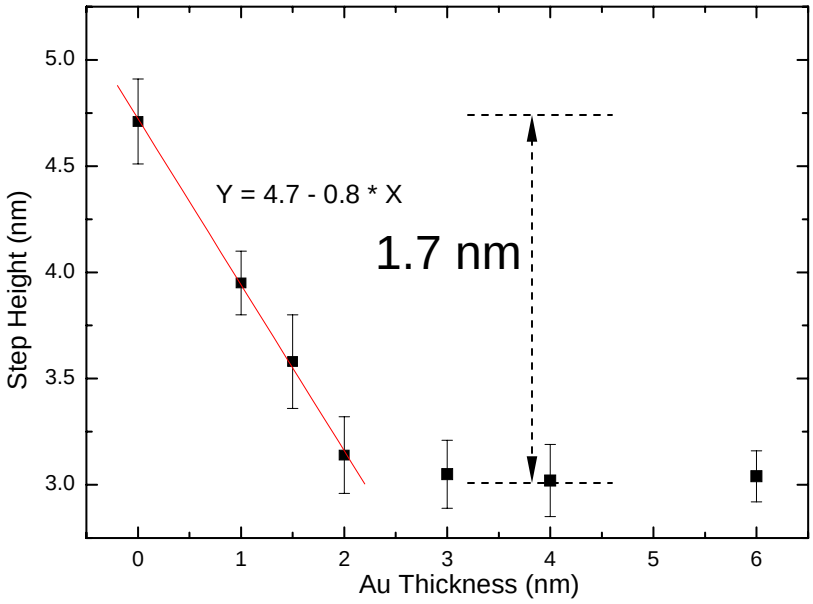

Figure 7.8 The step height between dendrimer-mediated and dendrimer-free regions for different Au thickness deposited.

The exact nature of the physical intermixing of the Au with the dendrimer layer is not known. Working on the assumption that there is very little 'space' between dendrimer molecules (we see none by AFM scan) it is clear that Au atoms must penetrate inside the molecules themselves as previously proposed[12]. The location of the Au which penetrates the molecules is an open question. In principle, instead of forming a highly dispersed Au/dendrimer nanocomposite layer at the mica surface (our expectation) it is possible that a layer of Au may form at the dendrimer-mica interface. This 'floating dendrimer' scenario is not supported by the cross-sectional analysis. If the dendrimer layer continued to reside on top of the Au film then the step heights would not be significantly affected by the deposition of Au.

LFM experiments have been carried out on two representative Au films, 2 nm and 6 nm thick Au deposited by plasma sputtering methods. Figure 7.9 shows the LFM topography, retrace

friction, and trace friction images of the 2 nm Au/dendrimer/mica films. The Au films cover the dendrimer patterned surface homogeneously. It is interesting to note that the presence of Au changes the friction contrast in dendrimer-mediated and dendrimer-free regions. As shown in Figure 7.2, before the deposition of Au films, the friction between scanning tip and dendrimer is larger than that between the tip and mica surface (the dendrimer-free region). After the 2 nm Au deposition, the friction contrast reverses, i.e., the friction force between the scanning tip and the Au/dendrimer/mica surface is lower than that between the tip and the Au/mica films. The lower Au thickness films (1 nm, and 1.5 nm) deposited onto dendrimer patterns were also imaged by LFM to try to better understand the transition. Unfortunately, the LFM results for 1 and 1.5 nm are very noisy and the friction contrast is not clear enough to interpret. The lower friction force between the tip and film surface in the dendrimer-mediated region could be interpreted as a result of the nanocomposite of Au/Dendrimer/mica becoming more rigid than Au/mica due to the penetration of Au into dendrimer molecules. This also might explain the observation that dendrimer mediated Au films have higher hardness[31] and behave a cutting wear scratch mechanism[40]. FMM was also tried on these samples but unfortunately the results are very noisy.

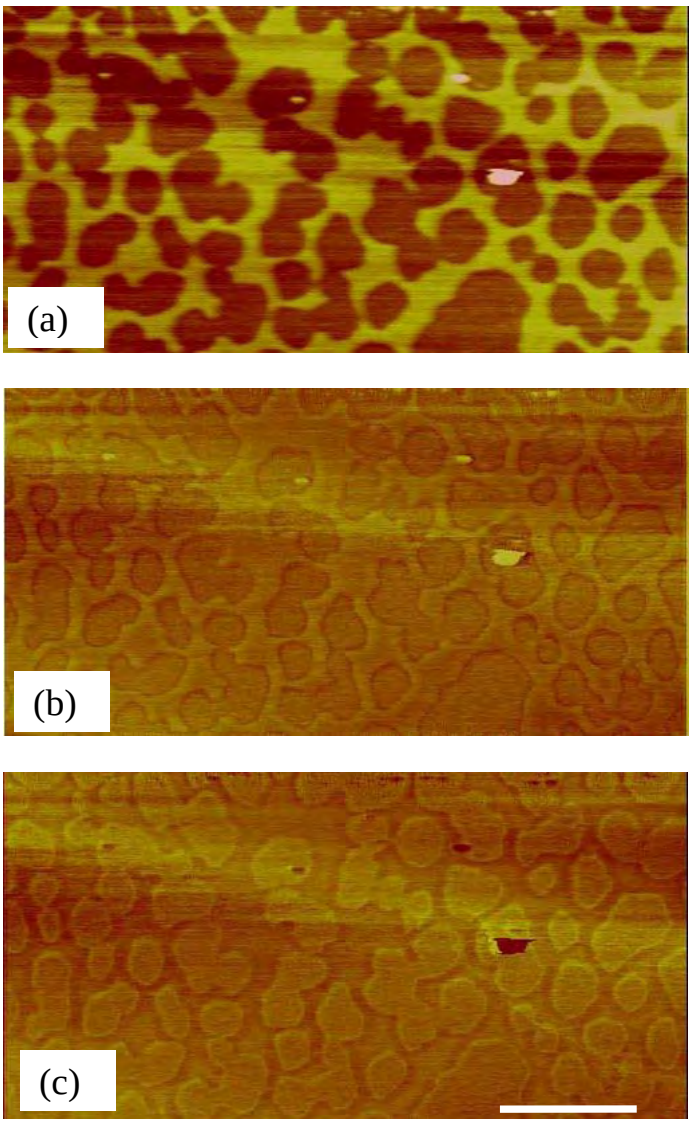

Figure 7.9 Lateral Force Microscopy (LFM) image of a 2 nm Au/dendrimer pattern/mica. topography(a), friction by retrace (b) and trace line (c). The bar is 1 μm.

A thicker (6 nm) Au film was also studied by LFM. Figures 7.10a, 10b and 10c are the LFM topography, retrace friction, and trace friction images of the 6 nm Au/dendrimer/mica films. The edge effect is very obvious and corresponds to the dendrimer pattern formation, yet the whole film appears to exhibit the same friction coefficient. This might be because the substrate effect (dendrimer/mica and mica) is canceled out in such thick Au films. FMM was

also used to evaluate the local stiffness of such films in the same region as the LFM images. Figures 7.11d, 11e and 11f are the FMM topography, retrace, and trace force modulation images of the 6 nm Au/dendrimer/mica films. The topography image is identical, as expected. There is very little contrast in the force modulation maps. This may indicate again that the entire surface is Au coated (as expected) and that the measurements are not sensitive enough to detect the subtle difference in elastic response one might expect between dendrimer-mediated and dendrimer-free regions.

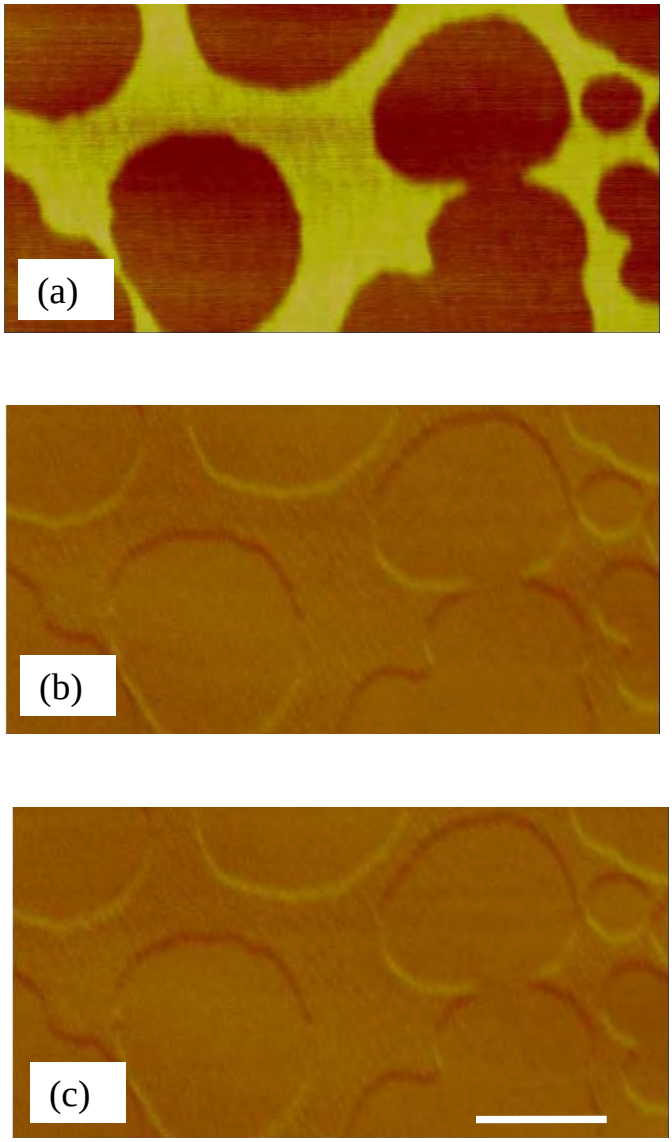

Figure 7.10 Lateral Force Microscopy (LFM) image of a 6 nm Au/dendrimer pattern/mica. topography(a), friction by retrace (b) and trace line (c). The bar is 1 μm.

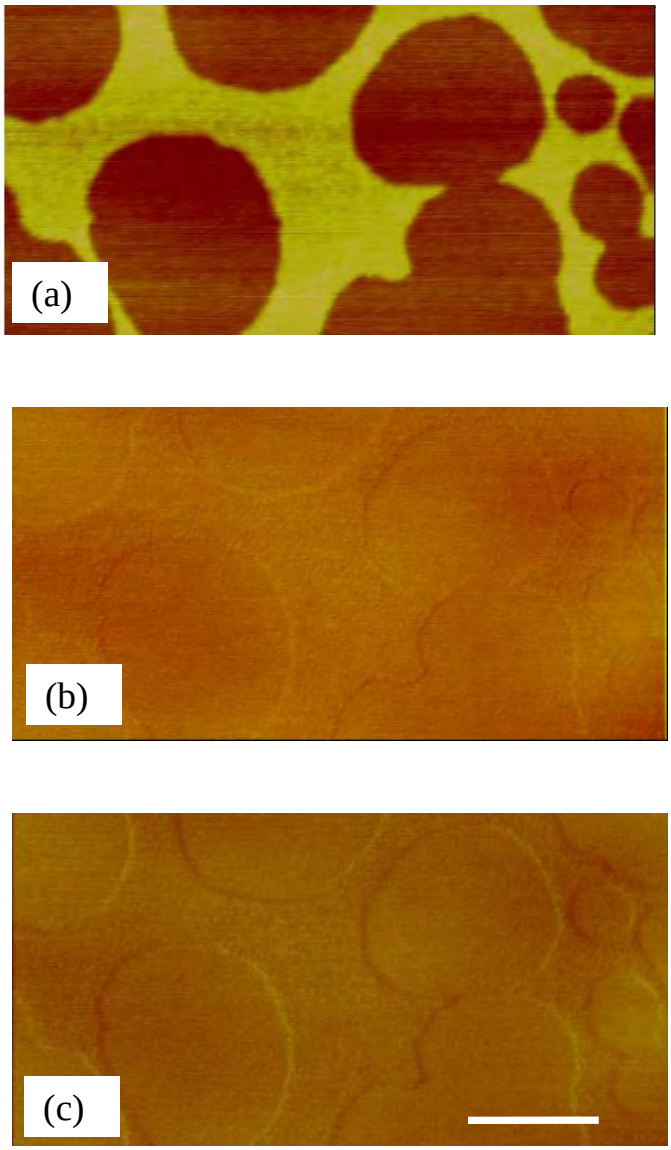

Figure 7.11 Force Modulation Microscopy (FMM) of 6 nm Au/dendrimer pattern/mica. (a), topography, (e), (f) force modulation mapping by retrace and trace line. The bar is 1 μm.

The possible growth and structure scenarios in the Au/dendrimer/substrate system are schematically illustrated in Figure 7.12. In Figure 7.12(a) a Au film deposited onto bare mica with a thickness of d_{Au}^{0} is shown; in Figure 7.12(b) dendrimer domains self assembled on a mica surface with a monolayer thickness of 4.7 nm are shown; the Au films deposited onto dendrimer domains under various hypotheses are shown in Figure 7.12 (c) – (f). In Figure 7.12(c), the step

height d_{step} after Au deposition is assumed to be equal to the dendrimer monolayer thickness d_{mono} ($d_{step} = d_{mono}$), there is no intermixing and no compression of the dendrimer layer, i.e., the Au 'floats' on top of dendrimer. In Figure 7.12d, the step height is also assumed to be the same as the dendrimer monolayer height ($d_{step} = d_{mono}$), but in this scenario the Au penetrates all the way through dendrimer and forms a Au film on the surface of mica substrate. For this case the dendrimer 'floats' on top of the Au film. In Figure 7.12e, the step height after Au deposition is less than the dendrimer monolayer thickness ($d_{step} < d_{mono}$). It is assumed that Au deposition causes the dendrimer to compress in the direction normal to the surface and that there is no intermixing between Au and dendrimer. Finally, in Figure 7.12f, the step height after Au deposition is assumed to be less than the dendrimer monolayer thickness ($d_{step} < d_{mono}$), in this case because of the intermixing between Au and the dendrimer layer and no compression is assumed.

Figure 12c - f lists the possible scenarios of Au films deposited onto dendrimer domain patterns. Since the observed step size decreases and is lower than the dendrimer monolayer thickness, the scenario presented in Figure 7.12c is not possible. In addition the LFM studies on 6 nm thick Au films shows that there is no contrast between dendrimer-free and dendrimer-mediated regions, indicating that the entire surface is covered with the same material, Au. The scenario presented in Figure 7.12d also does not apply because the step height changed in the observed results. Only the scenarios found in Figure 7.12e (intermixing) and 7.12f (compression) seem to be reasonable models for the structure of Au deposited on a dendrimer monolayer. Two factors lead us to conclude that the intermixing scenario is most likely. First, dendrimer molecules are already significantly compressed during the formation of the monolayer on the substrate yielding a thickness less than half of the diameter found in solution. Further

collapse associated with the presence of a Au overlayer is possible but unlikely to depend on overlayer thickness as we have clearly observed. Perhaps more importantly, the LFM studies of 2nm Au/dendrimer/mica films reveal that the presence of Au in this thickness range modifies the friction contrast in dendrimer-mediated and dendrimer-free regions as shown in Figure 7.2. Before the deposition of the thin Au film, the friction between scanning tip and dendrimer is larger than that between the tip and mica surface (the dendrimer-free region). After the 2 nm Au deposition, the friction contrast reverses, i.e., the friction force between the scanning tip and the Au/dendrimer/mica surface is lower than that between the tip and the Au/mica films. Compression alone (with the deposited Au sitting on top of the dendrimer layer) would not lead to the observed friction contrast. We therefore draw the conclusion that most logical explanation of the systematically decreasing step size is that the Au atoms penetrate into the dendrimer domain molecules up to a saturation point to form a more rigid nanocomposite films (intermixing) with lower friction force with the tip, as shown in Figure 7.12e. We cannot exclude the possibility that this effect might be combined with some further compression of the dendrimer molecules.

7.4 CHAPTER SUMMARY

In summary, a simple aerosol spray method is used to make self-assembled dendrimer monolayer patterns. These 2D structures were used as substrates for growth of sputtered Au films to form Au/mica and Au/dendrimer/mica films on single samples. The intermixing between Au and the dendrimer monolayer was directly observed to be 1.7 nm by AFM. LFM results indicate that that the friction between the tip and dendrimer molecules is larger than that between the tip and the mica substrate. LFM, FMM, and step height measurements were also used to conclude that Au is absorbed by the dendrimer layer up to an equivalent thickness of Au

of 2 nm and beyond this a Au film grows on top of both the dendrimer-mediated and bare mica surface.

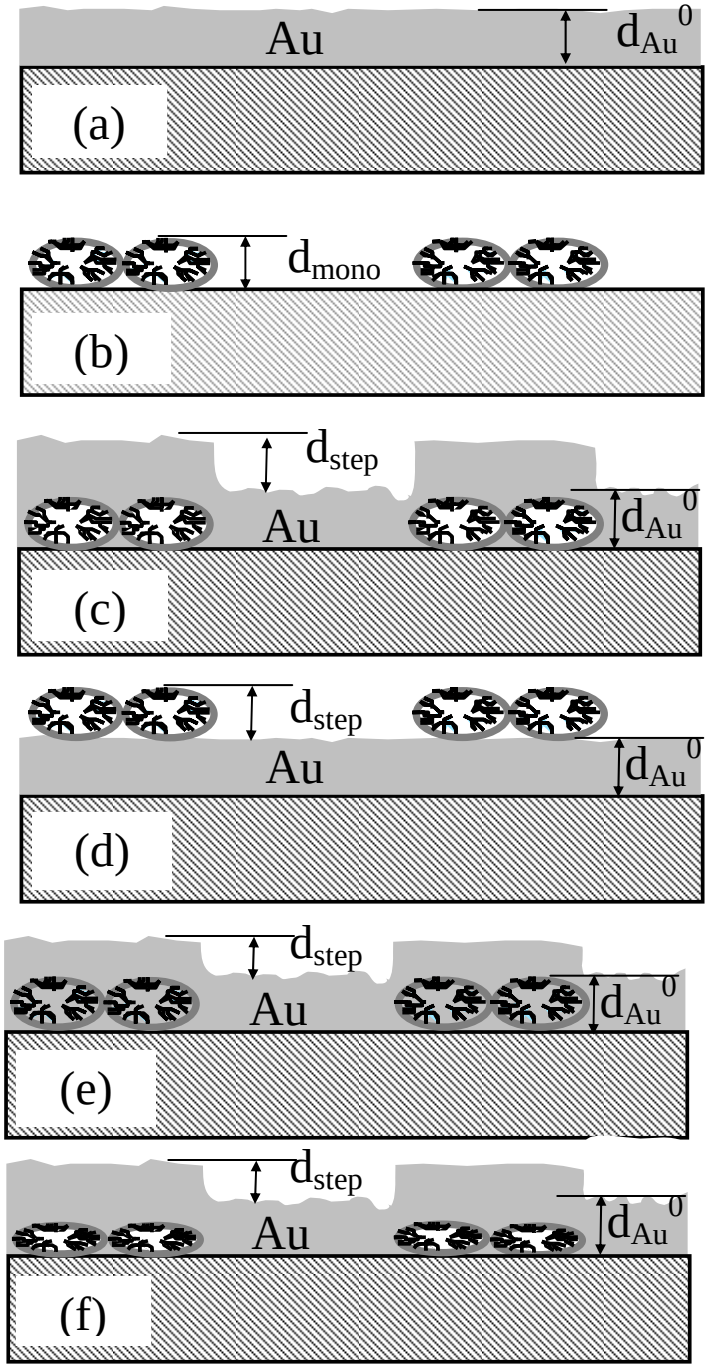

Figure 7.12 Schematics of metal film and dendrimer domain formation before and after Au deposition. (a) Au film on mica with thickness d_{Au}^{o}, (b) dendrimer domain on mica with monolayer thickness, (c) $d_{step} = d_{mono}$, no intermixing and compression, Au floating on the dendrimer, (d) $d_{step} = d_{mono}$, dendrimer floating on the Au film, (e) $d_{step} < d_{mono}$, with intermixing and no compression, (f) $d_{step} = d_{mono}$, with compression and no intermixing.

8.0 CONCLUSIONS, IMPACT, AND FUTURE WORK

8.1 KEY CONCLUSIONS

Dendrimer Monolayers and Interfacial Interactions

- Dendrimer monolayer interlayers used to mediate the growth of subsequently deposited metal thin films dramatically influence the nanotribological response of the composite system. Nanoscratch experiments clearly demonstrate a transition from plowing and wedge formation in dendrimer-free films to nearly pure cutting in dendrimer-mediated films. The benefits of dendrimer mediation (e.g., smoother more uniform films, increased hardness, enhanced adhesion) are coupled to tribological behavior that includes generation of debris resulting from cutting mode failure.
- Preliminary studies on Cu and Cr indicate that grain size effects, nanostructural uniformity, and extent of chemical interaction are relatively unimportant in explaining the nanoscratch observations. Physical intermixing is sufficient to produce an organic/inorganic nanocomposite with unique properties distinct from its component parts.

Dendrimer Domain Formation

- Aerosol deposition is a rapid and flexible alternative to the dipping and rinsing process for fabrication of dried dendrimer structures on substrates.

- By controlling the strength of the important interactions in the system, controllable monolayer height dendrimer domain patterns can be fabricated by aerosol processing. The experimentally observed domain pattern evolution with coverage is consistent with a theory of competing short range attractive and long range repulsive interactions. In the case of dendrimers on mica the long range interaction is electrostatic in origin and is associated with the contact potential between the negatively charged surface of the mica submerged in pentanol and the positively charged surface of the protonated dendrimer domains.

- Dried dendrimer patterns are remarkably stable in air and after reimmersion and may well serve as templates for patterned growth of thin films and nanostructures by vapor phase or liquid phase processing.

- If the forces associated with dewetting dominate the final molecular arrangements, then dried dendrimer structures are formed which reflect the dewetting phenomena and obscure any domain formation which may well have been present prior to final evaporation.

Physical Intermixing between Metal Overlayers and Dendrimer Domains

- Monolayer height dendrimer domain patterns are ideal bilevel heterogeneous substrates for studies of physical intermixing between molecular layers and vapor deposited films. Straightforward topographic measurements combined with a variety of scanning probe microscopy-based surface force measurements can elucidate the nature of the intermixing and overlayer formation in a very direct way.
- For the model experimental system of Au/25%C_{12} PAMAM G4, Au is found to be absorbed by the dendrimer layer up to a saturation amount (in this case the equivalent of 2 nm of Au) and beyond this a Au film grows on top of the Au saturated dendrimer-Au nanocomposite.

Charge Patterning of Granular Thin Films

- Granular thin films in the form of nanocrystals of metal embedded in a dielectric matrix are shown to have great potential as charge storage media for direct determination of the role of electrostatic forces on dendrimer domain formation. Granular media, specifically Fe or Co in SiO_2, exhibit the required characteristics of general robustness, flatness, charge stability, and isolation of charge from direct exposure to the solutions which contain the dendrimer molecules during assembly.

8.2 SCHOLARLY IMPACT

Portions of the work carried out in this dissertation have been presented and/or published separately, as follows.

Refereed publications:

1. F. T. Xu, S. M. Thaler and J.A. Barnard, “Stable Charge Storage in Granular Thin Films”, ***Appl. Phys. Lett.*** **86** (2005) 074105

2. F. T. Xu, S. M. Thaler and J.A. Barnard, “Structural and Mechanical Properties of Dendrimer-mediated Thin Films” ***J. Vac. Sci. Technol. A***, In press

3. F.T. Xu, S.C. Street, and J.A. Barnard, "Coverage dependent evolution of two-dimensional dendrimer/mica domain patterns", ***J. Phys. Chem. B*** **107** (2003) 12762-12767.

4. F.T. Xu, S.C. Street, and J.A. Barnard, "Pattern Formation in Aerosol-Deposited Dendrimer Films", ***Langmuir*** **19** (2003) 3066-3070.

5. F.T. Xu, P.P. Ye, M. Curry, J.A. Barnard, and S.C. Street, "Molecular Interlayers and the Mechanism of Abrasive Wear of Ultrathin Metal Films", ***Trib. Lett.*** **12** (2002) 189-193.

6. M. Curry, D. Arrington, S.C. Street, F.T. Xu, and J. Barnard, "Kinetic Energy Influences on the Growth Mode of Metal Overlayers on Dendrimer Mediated Substrates", ***J. Vac. Sci. Technol A*** **21** (2003) 34-240.

7. F.T. Xu, M. Curry, F. Huang, P.P Ye, A. Rar, S. Street, and J. Barnard, "Nanoscratch Behavior of Sputtered Metal Films on PAMAM Dendrimer Maonoalyers", ***Mat. Res. Soc. Symp. Proc.*** **710** (2002) DD14.4.1-6.

8. Fengting Xu, Long Li, Judith C Yang, Shane C Street and John A Barnard, “Enchanced Quality Nanocrystalline Metal Films Produced by Dendrimer Mediated Thin Film Growth”, ***Microsc. Microanal.*** **8** (Suppl. 2) (2002) 1120CD (*Abstr. Paper*).

9. M. Curry, F.T. Xu, J.A. Barnard, and S.C. Street. “Physical and mechanical characterization of dendrimer-metal nanocomposites.” 225th **ACS National Meeting**, New Orleans, LA, United States, March 23-27, 2003 (*Abstr. Paper*).

10. M. Curry, X. Li, F.T. Xu, F. Huang, J.A. Barnard, M. Weaver and S.C. Street. Surface modification by thin films for tribology. 227th **ACS National Meeting,** Anaheim, CA, United States, March 28-April 1, 2004 (*Abstr. Paper*).

Presentations:

1. “Dendrimer-mediated Thin Films Structural and Mechanical Characterization”, **MRS Spring meeting**, Mar. 29, 2005 , San Francisco (Oral Presentation)

2. “Stable Charge Storage in Granular Thin Films”, **MRS Spring meeting**, Mar. 29, 2005, San Francisco (Poster Presentation)
3. “Structural and Mechanical Properties of Dendrimer-mediated Thin Films”, **AVS Fall meeting**, Oct. 2004, Anaheim (Oral Presentation)
4. "Coverage dependent evolution of two-dimensional dendrimer/mica domain patterns", **MRS Fall meeting**, Dec. 2003, Boston (Poster presentation)
5. "Nanoscratch Behavior of Sputtered Metal Films on PAMAM Dendrimer Maonoalyers", **MRS Fall meeting**, Dec. 2001, Boston (Oral presentation)

8.3 RECOMMENDATIONS FOR FUTURE WORK

In many ways the experiments carried out in this dissertation have generated as many questions as answers. There are a number of important avenues for future research. Some key opportunities are summarized below.

Dendrimer Monolayers and Interfacial Interactions

- The nanoscratch studies of dendrimer-mediated metal films should be extended to focus on a detailed understanding of the evolution of nanomechanical behavior as a function of metal overlay thickness. By tracking nanocomposite formation and properties from the very thinnest depositions a more complete understanding can be developed. A greater emphasis on surface spectroscopy and SPM-based mechanical characterization will also be beneficial.

Dendrimer Domain Formation

- The most productive way forward in the dendrimer domain formation studies will require time dependent measurements of contact potentials and molecular rearrangements *in situ* in the liquid environment by SPM methods. Characterization of the dried structures is a

post mortem analysis. A more comprehensive understanding of detailed mechanisms, rates, and transient phenomena can only be gained by very challenging *in situ* experimentation.

Physical Intermixing between Metal Overlayers and Dendrimer Domains

- A key challenge is to develop an understanding at the atomic level of the intermixing of metals with dendrimer molecules. It is not known how long metal atoms such as Au may remain atomically dispersed in the dendrimer layer, when and where Au cluster formation may occur, and how the intermixing process eventually leads to fairly conventional Au overlayer film formation with recognizable 'metallurgical' grains, grain boundaries, twins, etc. The appropriate tool for the job is transmission electron microscopy. Significant challenges in sample preparation and preservation will have to be overcome.

Charge Patterning of Granular Thin Films

- A full understanding of charge storage in granular films will depend on detailed characterization of the size, shape, distribution, and crystal structure of the metal granules, knowledge of the chemistry of the interface between the granules and the insulating matrix, and a better appreciation of the variability of defect populations in the matrix. This will require a combination of transmission electron microscopy and surface spectroscopy studies.

APPENDIX

CHARGE PATTERNING OF GRANULAR THIN FILMS

As mentioned in Chapter 6, it may be possible to directly demonstrate the interaction of protonated of dendrimer molecules (which is used to explain the observed domain formation) using artificial charge patterning of a substrate. Films capable of storing charge in a local region near the surface may potentially be used as the template to directly assemble the dendrimer molecule patterns. Scanning probe microscopy methods may be used to write and image charged patterns with high spatial resolution. This Appendix reviews work carried out in the course of this dissertation developing a new charge storage film which might be used to directly confirm the importance of electrostatic interactions in the domain formation found for the 25%C_{12} PAMAM G4/pentanol/mica system. The required characteristics of the charge storage medium include general robustness, flatness, charge stability, and isolation of charge from direct exposure to the solutions which carry the dendrimer molecules. The existing charge storage systems do not satisfy these requirements which motivated this feasibility study.

A.1 INTRODUCTION

Unique opportunities exist for utilizing thin film electrets (dielectrics which exhibit quasi-permanent charge or alignment of dipoles) and nanoscale charge patterning for electrostatically directed assembly of complex functional nanostructures from discrete

charged/polarized nanoparticles and macromolecules[117]. Realization of such nanostructures depends on developing an understanding of the mechanisms and dynamics of charge storage and dissipation combined with quantitative characterization of electrostatic interactions in these systems. Scanning probe microscopy (SPM) methods (bias voltages applied to a conducting tip)[54] can be used for charging small positive or negative regions and creating charge patterns extending over tens of μm. Local charge densities are controlled by bias charging voltage and charging time. The same probe can then be used for characterization of electrostatic potential and topography. Electret materials considered to be appropriate for nanotechnological applications have been reviewed and organized into two primary categories: polymer films (e.g., PMMA) and silicon oxide (O) / silicon nitride (N) layered structures in various configurations on silicon (S) substrates (OS, NOS, and ONOS structures)[117]. Charge lifetimes for electret materials in these categories (single and multilayer films, homogeneous within the layer) vary widely from minutes to months, or longer, even for nominally identical materials prepared in different laboratories. The difficulty in fabricating thin film electrets with reproducible and reliable performance is an indication of their sensitivity to small variations in processing, charging procedures, and environment. The smallest charged regions which have been reported (by both SPM tip and e-beam charge injection) are of the order 50 nm or greater, significantly larger than the apparent 'spot' size at which charge is injected. Charging using a biased, sharp SPM tip could, in principle, produce charged regions localized to ~ 10 nm while focused e-beam could reduce this to ~ 1 nm. The high variability in thin film electret performance and the challenges in charge localization limit the usefulness of currently available materials for nanotechnological applications and highlight the need for development of new electret materials with reliable and tunable charge storage characteristics.

Charge storage using SPM methods has also been reported to a very limited extent in heterogeneous or granular films, including a layer of Co nanoclusters[57] (~ 3 nm) sandwiched by amorphous SiO_2, Si nanocrystals[58] (2 – 6 nm) embedded in amorphous SiO_2, and Ge clusters (a few nm) embedded in an amorphous hydrogenated carbon-germanium film[118]. For both the Co nanocluster and Si nanocrystal cases the charge stability is modest with decay times of a few hundred seconds (stability was not discussed for the Ge cluster samples). The ability to 'design' the granule chemistry, size, shape, and number density, the matrix chemistry, and the granule/matrix interface via materials processing makes granular systems scientifically and technologically attractive. A potential important advantage of granular systems is that charge injection apparently takes place within an individual granule indicating that high spatial resolution may be possible.

In this section we demonstrate highly stable charge storage in sputtered Fe-SiO_2 and Co-SiO_2 granular thin films using SPM methods. Both systems yield decay times as much as two orders of magnitude longer than previously reported in heterogeneous systems. Charge distributions are detected by Kelvin Probe Force Microscopy (KFM)[112] as well as by tapping mode atomic force microscopy (AFM) using a conducting tip (apparent height changes are induced by the electrostatic interaction between the charged region in the film and the image charge in the grounded tip)[58].

A.2 EXPERIMENTAL DETAILS

Experiments were performed on a commercial AFM (Nanoscope III - Dimension 3100, Veeco Instruments, Santa Barbara, CA). The cantilevers (MikroMasch, NSC18) are rectangular, 40μm wide, 2.5 – 3.5 μm thick and 230 μm long. Nominal spring constants range from 2.0 to

5.5 N/m and resonant frequencies from 60 to 90 kHz. Tips are silicon coated with Ti-Pt (nominal radius of ~ 40 nm). Granular Fe-SiO_2 and Co-SiO_2 thin films were prepared using rf sputtering, Corning 7059 glass substrates, and a split target assembly (half SiO_2 and half Fe (Co) foil). This arrangement yields granular films with a lateral Fe (Co) concentration gradient of ~ 0.5 volume % / mm. The Fe (Co) volume fraction varies from 0.18 to 0.62 (from isolated metal particles in SiO_2 to a percolating metallic network). The base pressure, Ar pressure, power density, and sputtering rate were 3×10^{-7} Torr, 10 mTorr, 0.62 W/cm^2, and ~ 0.1 nm/sec, respectively. A 10 nm SiO_2 capping layer protected the films against oxidation. 3 × 3 mm2 samples, each with a different Fe (Co) concentration, were cut from the glass wafers for study. Additional details of the sample preparation and magnetic characterization are available[119]. Results from films with similar Fe and Co concentrations (0.23 and 0.21) and thicknesses (~ 20 nm) are presented here. The Fe (Co) grain size was ~ 5 nm from transmission electron microscopy observations although there is considerable variation in the metal crystallite size.

Contact mode AFM with the tip dc biased to + 12 V or – 12 V was used to inject charge schematically shown in Figure A.1. The tip was first engaged to the surface without dc bias. The minimum vertical force between the tip and sample surface was then obtained in force calibration mode by adjusting the deflection set-point value in order to avoid damage to the surface by the tip. To create a charged spot the scan size was set at 1 nm. + 12 V or – 12 V was applied to the tip during the charge for 10 scans at 1Hz. The tip remained biased until it was retracted from the surface. KFM was used to obtain apparent height (AH) and surface potential (SP) images of the charged regions. First, a line scan of topographical data is recorded in standard tapping mode AFM. Charged regions in the granular films induce image charges in the AFM tip which vary with position. The electrostatic interaction between the two causes the tip

to adjust the tip-surface distance so as to maintain the amplitude of oscillation requested by the feedback loop thus producing contrast due to local charging in a simple topography image. When the tip is at ground (the case in our experiments) then the interaction between the charged region and its image in the tip is attractive whether the charged region is positive or negative, and a positive AH should result. The tip then retraces the same line at a set lift-height (30 nm) with the dc voltage of the tip adjusted by feedback electronics until it reaches the same potential as the sample (the surface potential), in the usual mannere.[120]. The two types of images are generated alternately line-by-line. All measurements were made at room temperature in ambient conditions.

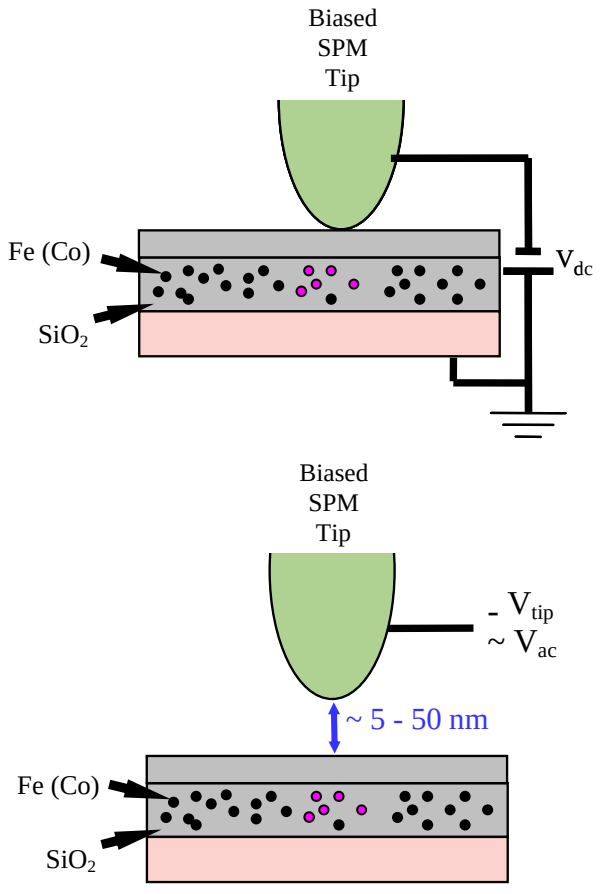

Figure A.1 Schematic of the charge writing (upper) and reading (lower) process by contact electrification method using a scanning probe microscope (SPM).

A.3 RESULTS AND DISCUSSION

The topographies of the $Fe_{0.23}$-SiO_2 and $Co_{0.21}$-SiO_2 films were characterized prior to the charging experiments using a standard AFM tip with a radius of ~ 10 nm. The films are flat (root-mean-square roughness of ~ 0.34 and 0.39 nm, respectively) and uniform with a slightly mottled appearance that gives no indication of the presence of individual Fe or Co granules.

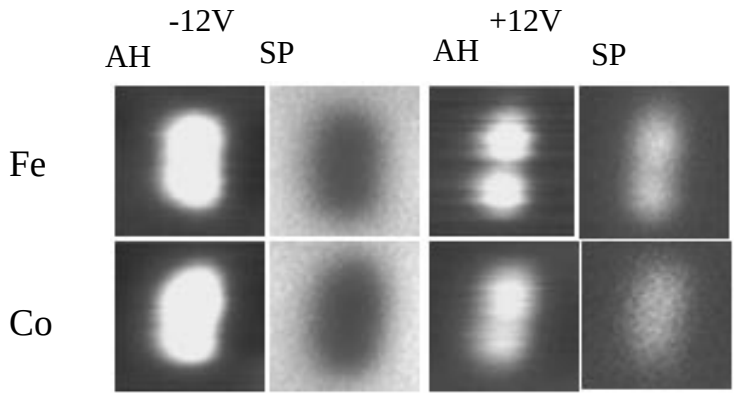

Figure A.2 Apparent height (AH) and surface potential (SP) images of charged regions (-12V and +12V) on $Fe_{0.23}$ - SiO_2 and $Co_{0.21}$ - SiO_2 granular thin films recorded ~ 256 s after charge injection. Images are 1.5μm x 1.5μm. Full scale for contrast in the AH images is 15 nm and for SP images it is 300 mV.

Figure A.2 shows AH and corresponding SP images associated with charged spots 'written' on $Fe_{0.23}$ - SiO_2 and $Co_{0.21}$ - SiO_2, as described above, with - 12 V and + 12 V applied to the tip during charge injection, and measured soon after charging (256 s). Clearly, and in line with expectations, the charged area is large compared to the tip radius (and compared to the individual metal granule size). Note that in the systems studied here ~ 70,000 granules/μm^2 of film are available for charging. The shape of the charged spot varies from charging event to charging event and depends on the local conditions at the point of contact (film topography, film chemistry, adsorbed contaminants, and the detailed morphology of the tip). For this group of

experiments elongated and even some ‘dumbbell’-shaped charged regions were produced. Irreproducibility in charging by SPM, including variations in charge shape and intensity, ‘bipolar’ charging, and even unpredictable charge sign, has been a common observation from the earliest reported measurements[54]. As expected, both positively and negatively charged surfaces yield positive AH. The decay in intensity of both positively and negatively charged regions with time for both granular systems is illustrated in Figure A.3 using SP images only (AH images closely track the SP, as seen in Figure A.2).

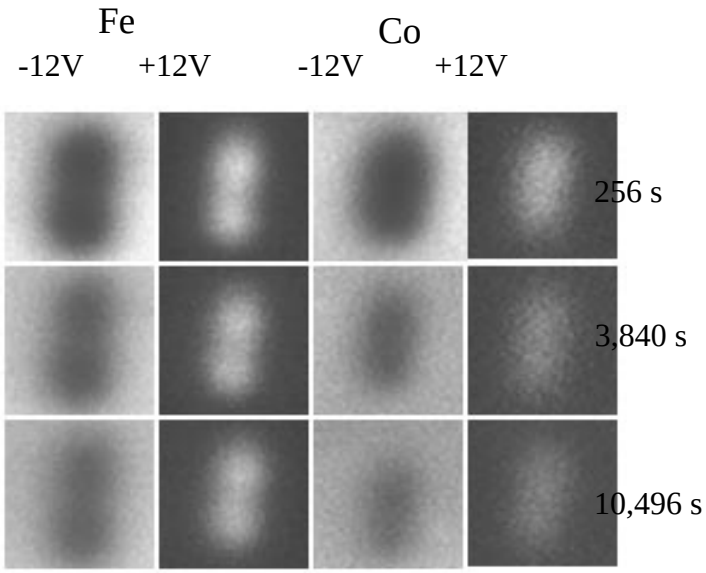

Figure A.3 Time evolution of surface potential (SP) images of charged regions (-12V and +12V) on $Fe_{0.23}$ - SiO_2 and $Co_{0.21}$ - SiO_2 granular thin films. Images are 1.5μm x 1.5μm. Full scale for contrast in SP images is 300 mV.

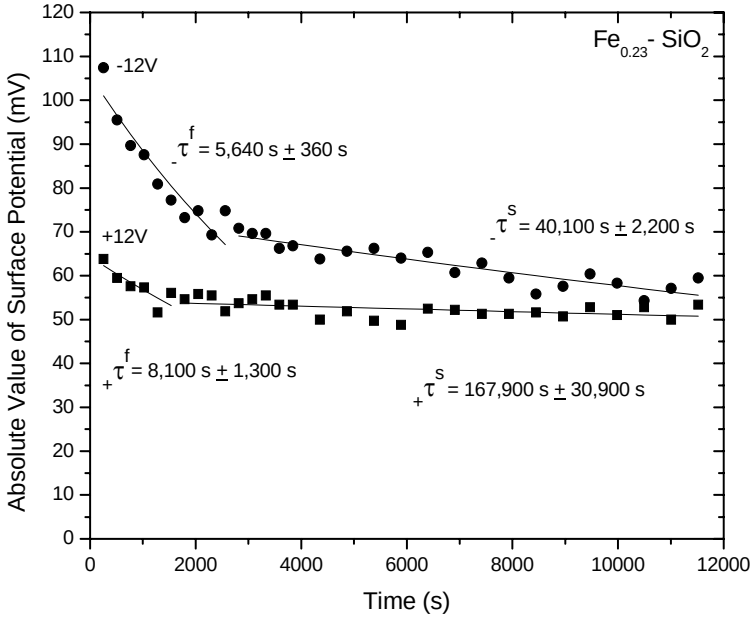

Figure A.4 Charge dissipation in $Fe_{0.23}$ - SiO_2 granular thin films. Solid circles: -12V; solid squares: +12V.

Charge stability in $Fe_{0.23}$ - SiO_2 has been quantified by monitoring the SP maximum within a charged region as a function of time (see Figure A.4). The error bars reflect the scatter in the detected local SP magnitude around the maximum in analysis of multiple cross sectional profiles. Both negatively (-12 V) and positively (+12 V) charged regions are monitored. Clearly, the magnitude of the SP for negatively charged regions is significantly larger than for positively charged regions. Using oppositely charged but equivalent magnitude charging conditions, $Fe_{0.23}$ - SiO_2 granular films are more readily charged by injection of electrons. The dissipation of charge in both cases is best described as occurring in two regimes, a comparatively fast regime at short times (up to 2,000 – 3,000 s) and a much slower regime at longer times (observed out to several days after charging but plotted here only to ~ 12,000 s). The data is well described by exponential fits for each case, with corresponding decay times ${}_-\tau^f$, ${}_-\tau^s$, ${}_+\tau^f$, ${}_+\tau^s$ (f, fast; s, slow),

with $_{-}\tau^{f} < {}_{+}\tau^{f}$ and $_{-}\tau^{s} < {}_{+}\tau^{s}$. For $Fe_{0.23}$ - SiO_2, $_{-}\tau^{f}$ = 5,460 s ± 360 s, $_{-}\tau^{s}$ = 40,100 s ± 2,200 s, $_{+}\tau^{f}$ = 8,100 s ± 1,300 s, and $_{+}\tau^{s}$ = 167,900 s ± 30,900 s. The goodness of fit based on a single decay time (not shown) is significantly poorer than the two regime approach. The time selected for the transition from one regime to the next is based on optimizing the quality of the fit. Due to our interest in obtaining high quality 'maps' of the spatial variation of the surface potential, the first SP maximum data points reported in this set of experiments correspond to 256 s after initial charging. We have also performed more rapid SP scans allowing data collection as soon as ~ 60 s after initial charging and find that the value for f is not significantly changed by inclusion of the shorter time data. Note that 60 s is very close to the time reported for the first data point in the sandwiched Co nanocluster work[57] in which a single, comparatively short decay time (see below) accounts for the observed behavior. It is well to keep in mind that it is likely that at sufficiently short times following local charging at 12 V there will be a period of more rapid, unmeasured charge decay (which may actually have little to do with the granular nature of our films). In this sense the f reported here should be viewed with some caution. Although granular $Fe_{0.23}$ - SiO_2 films are more readily charged negatively, this charge clearly dissipates more quickly than the positive version. The observed decay times are very large, one to two orders of magnitude larger than reported for a single layer of Co nanoclusters3 where only a single regime was noted with $_{-}\tau$ = 220 s and $_{+}\tau$ = 550 s. A simple physical explanation for the very long decay times reported here is not yet available. As noted above, measurements on granular thin film systems are very scarce. Based on the large variability in decay times reported in other classes of thin film electrets1 for nominally identical materials it seems evident that undetected differences in defect state, nanostructure, local composition, etc., can lead to large differences in charge dissipation. The longer decay times for positive versus negative charging

were interpreted as resulting from the Coulomb blockade energy associated with charging of Co nanoclusters. The difference between decay times for positive and negative charging was expected to decrease as the cluster size increased. It is possible that the two decay regimes noted in Figure A.4 (and Figure A.5, below) are broadly associated with smaller (faster decay) and larger (slower decay) clusters. Quantitative characterization of the metal granule size distribution is planned to clarify this point. The magnitude of the initial surface potential is found to vary within a small range from charging event to charging event. The experiment shown in Figure A.4 is representative and the decay times observed are essentially independent of the exact value of the initial surface potential. Identical charge stability experiments were also performed on $Co_{0.21}$ - SiO_2 granular thin films (Figure A.5). The same general trends are noted with two decay regimes, easier negative charging, but more stable positive charges. The decay times are shorter than for $Fe_{0.23}$ - SiO_2 but still one to two orders of magnitude longer than those found in other heterogeneous systems[57, 58].

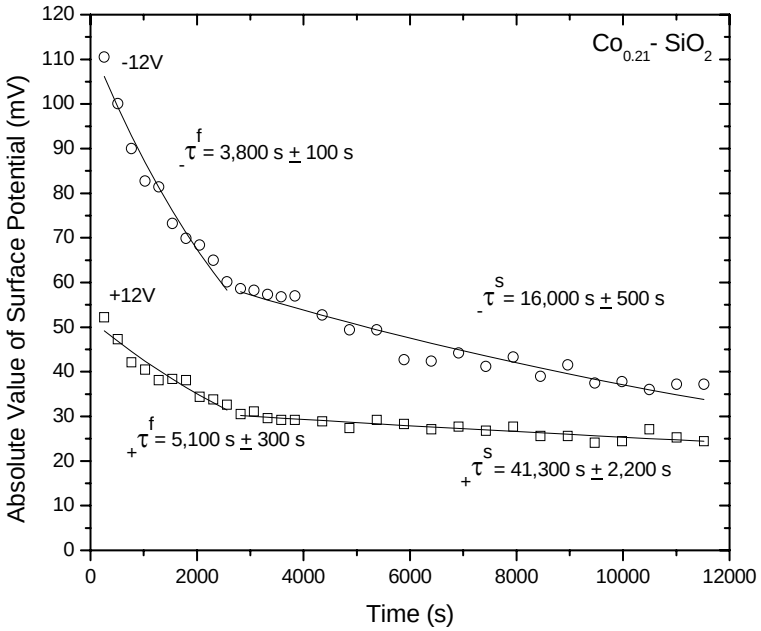

Figure A.5 Charge dissipation in $Co_{0.21}$ - SiO_2 granular thin films. Open circles: -12V; open squares: +12V.

Gaussian fits to the SP cross-sectional profiles used to quantify the decay of charge magnitude plotted in Figures A.4 and A.5 were also used to assess the evolution of the FWHM of the SP profiles. For positive and negative charges in $Fe_{0.23}$ - SiO_2 the FWHM is essentially constant with time while for $Co_{0.21}$ - SiO_2 a very slight, gradual decrease in FWMH is noted (data not shown here). The absence of charge spreading implies that the decay mechanism may be associated with the screening effect of mobile charge carriers able to diffuse to the charged region via the free surface (or the substrate).

In summary, highly stable local charge storage in Fe-SiO_2 and Co-SiO_2 granular thin films has been observed with decay times as much as two orders of magnitude longer than previously reported. Charge dissipation is well described as occurring in two regimes, a comparatively fast regime at short times (up to a few thousand seconds) and a much slower regime at longer times (up to a few days). Granular films of this type are more readily charged negatively, but negative charges dissipate more quickly than positive. Based on the results presented in this letter, granular thin films have great potential as a new class of stable electrets suitable for nanoscale charge patterning and electrostatically directed assembly of complex nanostructures. At this stage there is nothing to suggest that stable charge storage is confined to Fe - SiO_2 and Co - SiO_2; other systems are under investigation in our laboratory. Systematic studies of the size and stability of the charged region as a function of the charging voltage and injection time, focused on controlling the spatial extent of the charged region, are also underway. A full understanding of charge storage and dissipation in granular materials will also depend on quantitative structural and chemical characterization at the nanoscale.

A.4 IMPLICATIONS FOR DENDRIMER DOMAIN FORMATION STUDIES

Granular films in the form of nanocrystals embedded in a dielectric matrix have been shown to have great potential as a charge storage media for direct determination of the role of electrostatic forces on dendrimer domain formation. Granular media, specifically Fe or Co in SiO_2, exhibit the required characteristics of general robustness, flatness, charge stability, and isolation of charge from direct exposure to the solutions which contain the dendrimer molecules during assembly.

BIBLIOGRAPHY

[1] D. A. Tomalia, Adv. Mater. **6**, 529 (1994).

[2] D. A. Tomalia, A. M. Naylor, and W. A. Goddard III, Angew. Chem. **29**, 138 (1990).

[3] G. R. Newkome, Z. Yao, G. R. Baker, et al., J. Org. Chem. **50**, 2003 (1985).

[4] S. M. Grayson and J. M. J. Frechet, Chem. Rev. **101**, 3819 (2001).

[5] M. Zhao and R. M. Crooks, Adv. Mater. **11**, 217 (1999).

[6] M. Zhao, L. Sun, and R. M. Crooks, J. Am.Chem. Soc. **120**, 4877 (1998).

[7] L. Balogh and D. A. Tomalia, J. Am.Chem. Soc. **120**, 7355 (1998).

[8] E. Buhleier, W. Wehner, and F. Vogtle, Synthesis, 155 (1978).

[9] M. Fischer and F. Vogtle, Angew. Chem. Int. Ed. **38**, 884 (1999).

[10] D. A. Tomalia, H. Baker, J. Dewald, et al., Polymer J. **17**, 117 (1985).

[11] C. J. Hawker and J. M. Frchet, J. Am. Chem. Soc. **112**, 7638 (1990).

[12] T. M. Miller and T. X. Neenan, Chem. Mater. **2**, 346 (1990).

[13] J. Sagiv, J. Am.Chem. Soc. **102**, 92 (1980).

[14] S. R. Wasserman, Y.-T. Tao, and J. M. Whitesides, Langmuir **5**, 1074 (1989).

[15] J. D. Le Grange, J. L. Markham, and C. R. Kurjian, Langmuir **9**, 1749 (1993).

[16] R. Maoz and J. Sagiv, J. Colloid Interface Sci. **100**, 465 (1984).

[17] J. Gun and J. Sagiv, J. Colloid Interface Sci. **112**, 457 (1986).

[18] L. Strong and G. M. Whitesides, Langmuir **4**, 546 (1988).

[19] C. E. D. Chidsey and D. N. Loiacono, Langmuir **6**, 709 (1990).

[20] L. H. Dubois, B. R. Zegarski, and R. G. Nuzzo, J. Chem. Phys. **98**, 678 (1993).

[21] P. A. Williams, G. A. Reider, L. Li, et al., Phys. Rev. Lett. **79**, 3459 (1997).

[22] A. Kuhnle, S. Vollmer, T. R. Linderoth, et al., Langmuir **18**, 5558 (2002).

[23] D. R. Jung, A. W. Czanderna, and G. C. Herdt, in *Polymer Surface and Interfaces: Characterization, Modification, and Application*, edited by K. L. Mittal and K.-W. Lee (VSP, Utrecht, Netherlands, 1997), p. 189.

[24] G. C. Herdt and A. W. Czanderna, J. Vac. Sci. Technol. A **17**, 3415 (1999).

[25] G. L. Fisher, A. E. Hooper, R. L. Opila, et al., J. Phys. Chem. B **104**, 3267 (2000).

[26] S. R. Carlo, C. C. Perry, J. Torres, et al., Appl. Surf. Sci. **195**, 93 (2002).

[27] A. Ulman, Chem. Rev. **96**, 1533 (1996).

[28] V. V. Tsukruk, F. Rinderspracher, and V. N. Bliznyuk, Langmuir **13**, 2171 (1997).

[29] M. Zhao, Y. Liu, R. M. Crooks, et al., J. Am. Chem. Soc. **121**, 923 (1999).

[30] Y. Liu, M. L. Brueneing, D. E. Bergbreiter, et al., Angew. Chem., Int. Ed. **36**, 2114 (1997).

[31] S. C. Street, A. Rar, J. N. Zhou, et al., Chem. Mater. **13**, 3669 (2001).

[32] L. A. Baker, F. P. Zamborini, L. Sun, et al., Anal. Chem. **71**, 4403 (1999).

[33] A. Rar, M. Curry, J. A. Barnard, et al., Trib. Lett. **12**, 87 (2002).

[34] A. Rar, J. N. Zhou, W. J. Liu, et al., Appl. Surf. Sci. **175-176**, 134 (2001).

[35] M. Curry, D. Arrington, S. C. Street, et al., J. Vac. Sci. Technol. A **21**, 234 (2003).

[36] V. N. Blizniuk, F. Rinderspacher, and V. V. Tsukruk, Polymer **39**, 5249 (1998).

[37] J. Li and D. J. Meier, polymer preprints **37**, 591 (1996).

[38] D. Arrington, M. Curry, and S. C. Street, Langmuir **18**, 7788 (2002).

[39] X. Li, M. Curry, G. Wei, et al., Surface and Coatings Technology **177-178**, 504 (2004).

[40] F. T. Xu, P. P. Ye, M. Curry, et al., Trib. Lett. **12**, 189 (2002).

[41] K. M. A. Rahman, C. J. Durning, N. J. Turro, et al., Langmuir **16**, 10154 (2000).

[42] H. Tokuhisa, M. Zhao, L. A. Baker, et al., J. Am. Chem. Soc. **120**, 4492 (1998).

[43] A. Hierlemann, J. K. Campbell, L. A. Baker, et al., J. Am. Chem. Soc. **120**, 5323 (1998).

[44] M. C. Coen, K. Lorenz, J. Kessler, et al., Macromolecules **29**, 8069 (1996).

[45] M. Sano, J. Okamuro, A. Ikeda, et al., Langmuir **17**, 1807 (2001).

[46] F. T. Xu, S. C. Street, and J. A. Barnard, Langmuir **19**, 3066 (2003).

[47] F. T. Xu, S. C. Street, and J. A. Barnard, J. Phys. Chem. B **107**, 12762 (2003).

[48] D. J. Struik, (Princeton University Press, Princeton, NJ, 1986).

[49] B. N. Chapman, *Glow Discharge Processes* (Wiley, New York, 1980).

[50] M. Ohring, *Materials science of thin Films* (Academic Press, San Diego, 2002).

[51] G. Binning, H. Rohrer, C. H. Gerber, et al., Phys. Rev. Lett. **49**, 57 (1982).

[52] G. Binning, C. F. Quate, and C. H. Gerber, Phys. Rev. Lett. **56**, 930 (1986).

[53] R. D. Piner, J. Zhu, F. Xu, et al., Science **283**, 661 (1999).

[54] B. D. Terris, J. E. Stern, D. Rugar, et al., Phys. Rev. Lett. **63**, 2669 (1989).

[55] B. D. Terris, J. E. Stern, D. Rugar, et al., J. Vac. Sci. Technol. A **8**, 374 (1990).

[56] R. C. Barrett and C. F. Quate, J. Appl. Phys. **70**, 2725 (1991).

[57] D. M. Schaadt, E. T. Yu, S. Sankar, et al., Appl. Phys. Lett. **74**, 472 (1999).

[58] E. A. Boer, L. D. Bell, M. L. Brongersma, et al., Appl. Phys. Lett. **78**, 3133 (2001).

[59] J. Zhao and K. Uosaki, Appl. Phys. Lett. **83**, 2034 (2003).

[60] L. Kuhn, *The Triboscope Nanomechanical Testing System*, 1999).

[61] K. Siegbahn, C. Nording, A. Fahlman, et al., Nova Acta Regiae Soc. Sci. Ups., 201 (1967).

[62] M. Curry, in *Department of Chemistry* (University of Alabama, Tuscaloosa, 2004).

[63] D. B. Williams and C. C. B., *Transmission electron microscopy: a textbook for materials science* (Plenum Press, New York, 1996).

[64] B. D. Cullity, *Element of X-ray Diffraction* (Addison-Wesley Publishing Company, Inc., 1978).

[65] C. M. Mate, B. K. Yan, D. C. Miller, et al., IEEE Trans. Magn. **36**, 110 (2000).

[66] H. Zabel, Appl. Phys. A **58**, 159 (1994).

[67] T. C. Huang and W. Parrish, *Advances in X-ray analysis* (Plenum, New York, 1992).

[68] J. I. Goldstein, D. E. Newbury, P. Echlin, et al., *Scanning electron Microscopy and X-ray microanalysis* (Plenum press, New York and London, 1992.).

[69] F. Brochard-Wyart and J. Daillant, Can. J. Phys. **68**, 1084 (1990).

[70] G. Reiter, Phys. Rev. Lett. **68**, 75 (1992).

[71] T. G. Stange, D. F. Evans, and W. A. Hendrickson, Langmuir **13**, 4459 (1997).

[72] S. Herminghaus, K. Jacobs, K. Mecke, et al., Science **282**, 5390 (1998).

[73] J. H. Tylczak, (ASM International, 1992), Vol. 18.

[74] A. Stierle, P. Bodeker, and H. Zabel, Surf. Sci. **327**, 9 (1995).

[75] A. Stierle, T. Muhge, and H. Zabel, J. Mater. Res. **9**, 884 (1994).

[76] A. Stierle and H. Zabel, Surf. Sci. **385**, 310 (1997).

[77] A. Stierle and H. Zabel, Europhys. Lett. **37**, 365 (1997).

[78] G. Muralidharan, X. Z. Wu, and H. You, Scripta Metall. **37**, 1177 (1997).

[79] A. J. G. Leenaers and D. K. G. de Boer, (Philips Electronic Instruments Company, Mahwah, NJ, 1998).

[80] L. G. Parratt, Phys. Rev. **95**, 359 (1954).

[81] C. B. Duke, PNAS **100**, 358 (2003).

[82] A. H. Cottrell, Trans. Metall. Soc. AIME **212**, 192 (1958).

[83] N. J. Petch, J. Iron Steel Inst. **174**, 25 (1953).

[84] W. C. Bigelow, D. L. Pickett, and W. A. Zisman, J. Colloid Interface Sci. **1**, 513 (1946).

[85] S. D. Evans and A. Ulman, Chem. Phys. Lett. **170**, 462 (1990).

[86] A. Kumar, H. A. Biebuyck, and G. M. Whitesides, Langmuir **10**, 1498 (1994).

[87] X. Zhang, M. Wilhelm, J. Klein, et al., Langmuir **16**, 3884 (2000).

[88] A. Sharma and A. T. Jameel, J. Colloid Interface Sci. **161**, 190 (1993).

[89] J. W. Cahn, J. Chem. Phys. **42**, 93 (1965).

[90] V. S. Mitlin, J. Colloid Interface Sci. **156**, 491 (1993).

[91] A. V. Oppenheim and R. W. Schafer, *Discrete-time signal processing* (Prentice-Hall, Englewood Cliffs, NJ, 1989).

[92] L. Cheng and J. A. Cox, Electrochim. Commun. **3**, 285 (2001).

[93] L. Cheng, G. E. Pacey, and J. A. Cox, Electrochim. Acta **46**, 4223 (2001).

[94] A. J. Khopade and F. Caruso, Nano Lett. **2**, 414 (2002).

[95] H. C. Yoon and H.-S. Kim, Anal. Chem. **72**, 922 (2000).

[96] D. Andelman, F. Brochard, and J.-F. Joanny, J. Chem. Phys. **86**, 3673 (1987).

[97] M. M. Hurley and S. J. Singer, Phys. Rev. B **46**, 5783 (1992).

[98] C. Sagui and R. C. Desai, Phys. Rev. E **49**, 2225 (1994).

[99] K.-O. Ng and D. Vanderbilt, Phys. Rev. B **52**, 2177 (1995).

[100] Z. Suo and W. Lu, J. Mech. Phys. Solids **48**, 211 (2000).

[101] M. Seul and D. Andelman, Science **267**, 476 (1995).

[102] M. Seul and V. S. Chen, Phys. Rev. Lett. **70**, 1658 (1993).

[103] M. Seul and M. J. Sammon, Phys. Rev. Lett. **64**, 1903 (1990).

[104] D. J. Benvegnu and H. M. McConnell, J. Phys. Chem. **96**, 6820 (1992).

[105] H. M. McConnell, Annu. Rev. Phys. Chem. **42**, 171 (1992).

[106] R. Allenspach, M. Stampanoni, and A. Bischof, Phys. Rev. Lett. **65**, 3344 (1990).

[107] S. A. Langer, R. E. Goldstein, and D. P. Jackson, Phys. Rev. A **46**, 4894 (1992).

[108] R. Plass, J. A. Last, N. C. Bartelt, et al., Nature **412**, 875 (2001).

[109] R. F. Voss, R. B. Laibowitz, and E. I. Allessandrini, Phys. Rev. Lett. **49**, 1441 (1982).

[110] U. Raviv, P. Laurat, and J. Klein, J. Chem. Phys. **116**, 5167 (2002).

[111] Y. F. Gao and Z. Suo, J. Appl. Phys. **93**, 4276 (2003).

[112] M. Nommenmacher, M. P. O'Boyle, and H. K. Wickramasinghe, Appl. Phys. Lett. **58**, 2921 (1991).

[113] O. Teschke and E. F. de Souza, Appl. Phys. Lett. **74**, 1775 (1999).

[114] D. R. Lide, in *CRC Handbook of Chemistry and Physics* (CRC Press, 1994), p. 6.

[115] J. Li, L. T. Piehler, D. Qin, et al., Langmuir **16**, 5613 (2000).

[116] S. Granick, S. K. Kumar, and E. J. Amis, J. Polymer Sci B **41**, 2755 (2003).

[117] W. M. D. Wright and D. G. Chetwynd, Nanotechnology **9**, 133 (1998).

[118] P. Kazimierski and J. Tyczkowski, Surf. Coat. Technol. **174-175**, 770 (2003).

[119] J. Gomez, A. Butera, and J. A. Barnard, Phys. Rev. B **70**, 054428 (2004).

[120] H. O. Jacobs and G. M. Whiteside, Science **291**, 1763 (2001).